Characterization of laser-induced plasma and application to surface-assisted LIBS for powder and liquid samples

Ye Tian

N° d'ordre: 2017LYSE1292 Année 2017

THESE DE L'UNIVERSITE DE LYON

Délivrée par

L'UNIVERSITE CLAUDE BERNARD LYON 1

ECOLE DOCTORALE

ED 52 PHAST Physique et Astrophysique de Lyon

DIPLOME DE DOCTORAT

(arrêté du 7 août 2006)

Soutenue publiquement le 8 Décembre 2017

Par

Ye TIAN

TITRE:

Characterization of laser-induced plasma and application to surface-assisted LIBS for powder and liquid samples

Directeur de thèse : Professeur Jérôme BERNARD

JURY:

M.	Jérôme BERNARD	Directeur
M.	Christian BORDAS	Examinateur
Mme.	Nicole DELEPINE-GILON	Examinatrice
M.	Christophe DUTOUQUET	Rapporteur
Mme.	Ying LI	Rapporteur
M.	Jean-Baptiste SIRVEN	Membre invité
M.	Jin YU	Examinateur

UNIVERSITE CLAUDE BERNARD - LYON 1

Président de l'Université	**M. le Professeur Frédéric FLEURY**
Président du Conseil Académique	M. le Professeur Hamda BEN HADID
Vice-président du Conseil d'Administration	M. le Professeur Didier REVEL
Vice-président du Conseil Formation et Vie Universitaire	M. le Professeur Philippe CHEVALIER
Vice-président de la Commission Recherche	M. Fabrice VALLÉE
Directrice Générale des Services	Mme Dominique MARCHAND

COMPOSANTES SANTE

Faculté de Médecine Lyon Est – Claude Bernard	Directeur : M. le Professeur G.RODE
Faculté de Médecine et de Maïeutique Lyon Sud – Charles Mérieux	Directeur : Mme la Professeure C. BURILLON
Faculté d'Odontologie	Directeur : M. le Professeur D. BOURGEOIS
Institut des Sciences Pharmaceutiques et Biologiques	Directeur : Mme la Professeure C. VINCIGUERRA
Institut des Sciences et Techniques de la Réadaptation	Directeur : M. X. PERROT
Département de formation et Centre de Recherche en Biologie Humaine	Directeur : Mme la Professeure A-M. SCHOTT

COMPOSANTES ET DEPARTEMENTS DE SCIENCES ET TECHNOLOGIE

Faculté des Sciences et Technologies	Directeur : M. F. DE MARCHI
Département Biologie	Directeur : M. le Professeur F. THEVENARD
Département Chimie Biochimie	Directeur : Mme C. FELIX
Département GEP	Directeur : M. Hassan HAMMOURI
Département Informatique	Directeur : M. le Professeur S. AKKOUCHE
Département Mathématiques	Directeur : M. le Professeur G. TOMANOV
Département Mécanique	Directeur : M. le Professeur H. BEN HADID
Département Physique	Directeur : M. le Professeur J-C PLENET
UFR Sciences et Techniques des Activités Physiques et Sportives	Directeur : M. Y.VANPOULLE
Observatoire des Sciences de l'Univers de Lyon	Directeur : M. B. GUIDERDONI
Polytech Lyon	Directeur : M. le Professeur E.PERRIN
Ecole Supérieure de Chimie Physique Electronique	Directeur : M. G. PIGNAULT
Institut Universitaire de Technologie de Lyon 1	Directeur : M. le Professeur C. VITON
Ecole Supérieure du Professorat et de l'Education	Directeur : M. le Professeur A. MOUGNIOTTE
Institut de Science Financière et d'Assurances	Directeur : M. N. LEBOISNE

Caractérisation et spectroscopie de plasmas induits par laser et application de la LIBS assistée par surface à des échantillons en poudre ou en liquide

Résumé

La spectroscopie de plasma induit par laser (En anglais LIBS: laser-induced breakdown spectroscopy) est une méthode analytique de spectroscopie d'émission optique qui utilise un plasma induit par laser comme source de vaporisation, d'atomisation et d'excitation. Bien que la LIBS ait démontré sa polyvalence et ses caractéristiques attrayantes dans de nombreux domaines, les aspects quantitatifs de la LIBS sont considérés comme son talon d'Achille. D'un point de vue fondamental, cela peut être dû à la nature complexe du plasma induit par laser comme source d'émission spectroscopique. La caractérisation temporelle et spatiale du plasma induit par laser est considérée comme l'un des points clés pour comprendre les fondements de la technique LIBS. D'autre part, la LIBS est habituellement caractérisée par l'utilisation d'une ablation laser directe, sans traitement préalable de l'échantillon. Cela pourrait être assez limitant en particulier pour certains types de matériaux tels que des poudres ou des liquides. Une préparation adéquate ou un traitement approprié de l'échantillon permettant le dépôt d'un film mince et homogène de l'échantillon sur une surface métallique pourrait grandement augmenter le potentiel de la LIBS en vue d'obtenir de meilleures performances analytiques, et notamment une meilleure sensibilité et un effet de matrice réduit. On parle alors de LIBS assistée par surface car la matrice métallique contribue à une augmentation de la température du plasma.

Le présent travail de thèse est donc motivé par deux aspects importants de la technique LIBS: la connaissance du plasma induit par laser comme source d'émission spectroscopique, et de nouvelles méthodes de préparation des échantillons pour améliorer la performance analytique de la LIBS, notamment pour des échantillons comme poudres et liquides visqueux. La première partie de cette thèse (chapitre 2) est consacrée à la caractérisation du plasma induit sur des échantillons de verre, en fonction de la longueur d'onde du laser, infrarouge (IR) ou ultraviolet (UV), et du gaz ambiant, de l'air ou de l'argon. L'imagerie spectroscopique et la spectroscopie d'émission résolue en temps et en espace sont utilisées pour le diagnostic du plasma. La deuxième partie de cette thèse est de développer des méthodes de préparation d'échantillons, déposés sur des surfaces métalliques pour l'analyse LIBS de poudres ainsi que de vins comme exemples de liquide. Au chapitre 3, nous avons appliqué la LIBS pour l'analyse quantitative dans des poudres (exemples de poudres : cellulose, alumine ainsi que de la terre). Au chapitre 4, nous avons appliqué la LIBS pour la classification des vins français selon leurs régions de production. Deux modèles de classification basées sur l'analyse des composants principaux (PCA) et la forêt aléatoire (RF) sont utilisés pour la classification. A l'aide de ces applications, ce travail de thèse démontre l'efficacité de la méthode LIBS assistée par surface pour l'analyse de poudres (cellulose, alumine et sols) et de liquides (vins), avec une limite de détection dans l'ordre de ou sous la ppm et une réduction significative de l'effet de matrice.

Mots clés

Spectroscopie de plasma induit par laser, diagnostic de plasmas, LIBS assistée par surface, analyse quantitative, classification, effet de matrice, normalisation avec une référence interne.

Characterization of laser-induced plasma and application to surface-assisted LIBS for powder and liquid samples

Abstract

Laser-induced breakdown spectroscopy (LIBS) is an analytical method with optical emission spectroscopy that uses a laser pulse to vaporize, atomize, and excite a hot plasma as the spectroscopic emission source. Although LIBS has demonstrated its versatility and attractive features in many fields, the quantitative analysis ability of LIBS is considered as its Achilles' heel. From a fundamental point of view, this can be due to the complex nature of laser-induced plasma as the spectroscopic emission source for LIBS application. The temporal and spatial characterization of laser-induced plasma is considered as one of the key points for the LIBS technique. On the other hand, from the analytical point of view, LIBS is usually characterized by direct laser ablation. This can be however quite limiting, especially for some types of materials such as powders or liquids. Proper sample preparation or treatment allowing the deposition of a thin homogeneous film on a metallic surface could greatly improve the analytical performance of LIBS for these types of materials. Since the metallic surface is expected to contribute to increase the temperature and the density of the plasma and, consequently, to a better overall sensitivity, we call this technique surface-assisted LIBS.

The present thesis work is therefore motivated by two basic aspects of LIBS analysis: the need of an improved knowledge of laser-induced plasma as a spectroscopic emission source, and new methods to improve the analytical performance of LIBS, including a higher sensibility and a reduced matrix effect. The first part of this thesis (Chapter 2) is dedicated to an extensive characterization of the plasma induced on glass samples, as a function of the laser wavelength, infrared (IR) or ultraviolet (UV), and the ambient gas, air or argon. Both the spectroscopic imaging and time- and space-resolved emission spectroscopy are used for plasma diagnostics in this work. The second part of this thesis is to develop a surface-assisted LIBS method for the elemental analysis in powders, and in wines as examples of liquids. We applied the surface-assisted LIBS for the quantitative elemental analysis in cellulose powders, alumina powders, and soils (Chapter 3). Special attentions are paid on the figures-of-merit, matrix effects, and normalization approaches in LIBS analysis. We also used the surface-assisted LIBS for the classification of French wines according to their production regions (Chapter 4). Two classification models based on the principal component analysis (PCA) and random forest (RF) are used for the classification. Through these applications, this thesis work demonstrates the efficiency of the surface-assisted LIBS method for the analysis of powders (cellulose, alumina and soils) and of liquids (wines), with ppm or sub-ppm sensitivities and a reduced matrix effect.

Keywords

Laser-induced breakdown spectroscopy (LIBS), plasma diagnostics, surface-assisted LIBS, quantitative analysis, classification, matrix effects, normalization approaches.

Acknowledgments

I have been fortunate in my life to experience my PhD study in Lyon, and I have been fortunate in my career to be surrounded by and to work with great people.

First I would like to thank my advisor, Prof. Jin Yu, for his excellent mentorship during my thesis work in ILM, Lyon 1 University. Jin provided an ideal environment for me to begin my research in Lyon. He is always full of ideas, allowing me to go ahead no matter what kind of difficulties encountered. Jin helped me a lot on the academic writing. He also encouraged and supported me to present my work in the conferences, and helped me to prepare my presentation word by word. All of these gave me great confidence in my future career to be a teacher-researcher. Aside from the research, Jin also helped me a lot in my daily life in Lyon. I will never forget the moments that we drink wines together in a restaurant in Vieux Lyon, and take photos and dance in Chamonix Mont-Blanc…

I would also like to thank my thesis director, Prof. Jérôme Bernard, for supporting me to continue and accomplish my thesis work. He made great efforts on the correction of the manuscript. He helped me not only on the carefully language work, but also gave me plenty of comments and suggestions which significantly improved the quality of my thesis. Jerome also helped me a lot on the registration as well as administration works for my PhD study. I would like to thank Prof. Li Chen and Prof. Serge Martin, I really enjoy the lunch time every day in Maison d'hôtes together with them.

I would like to thank Prof. Nicole Delepine-Gilon for helping me to prepare the samples I used in this thesis. I can find almost everything that I need in her laboratory, and she was so nice to let me use all of them. Nicole also taught me a lot of knowledge and skills in the area of analytical chemistry. I always discuss with her before starting a new experiment. I feel happy to work in Nicole's lab.

I would like to thank the reviewers of my thesis, Dr. Christophe Dutouquet and Prof. Ying Li, for reading my thesis carefully and sending the reports on time. I am especially grateful for that Prof. Ying Li accepted to be member of my jury and attended my thesis

defense after a long trip from China. I would also like to thank the rest of my thesis committee, Prof. Christian Bordas, Prof. Nicole Delepine-Gilon, and Dr. Jean-Baptiste Sirven. I thank all the jury members for their challenging questions and valuable comments and suggestions on my thesis work.

I would like to thank my colleagues in our team. Xueshi Bai gave me a good training on the laboratory skills which allowed me to obtain good results very quickly at the first year. She is also one of my best friends in Lyon. Daniel Förster was always patient to translate everything in French for me whenever I need help. Mingchao Ji helped me to quickly become familiar with the life in Lyon and the work environment in our institute. During these years I also worked with Ekaterina Sokolova, Jorge Serrano, Hoi Ching Cheung, Jana Bockova, Jialu Yu, and Hualiang Yin. All of them helped me a lot on the experiments and made the research work full of fun. I would also like to thank my good friends in Lyon. I was always in a happy mood together with them and kept on peace of mind in this beautiful city.

I would also like to thank my professors and colleagues in Ocean University of China. Prof. Ronger Zheng, my supervisor since Bachelor degree, always supported me to go ahead following my heart and gave me the necessary energy. I was so lucky to be one of her students. Prof. Ying Li and Prof. Guang Yuan also supported me a lot on my research. I worked closely with Huaming Hou and Boyang Xue, they helped me a lot on my experiments as well as data treatments. I would also like to thank Dr. Tianlong Zhang in Northwest University for his effective contributions on the data analysis work.

I would like to thank my family for believing in me and for encouraging me for all these years of my education. Finally I would like to thank Huilin Zheng, my wife, for her devotion and support on my research work. I thank her for helping me with all the day-to-day chores so that I could focus on my thesis and finish my degree.

I would like to acknowledge the China Scholarship Council (CSC) for providing me with the scholarships which supported me to accomplish the PhD study.

Contents

General introduction

Laser-induced breakdown spectroscopy (LIBS) is a method of optical emission spectroscopy (OES) that uses a laser-induced plasma as the hot vaporization, atomization, and excitation source. The optical emission from the laser-induced plasma is thus used for chemical analysis purposes. Generally, in a LIBS measurement, an intense pulsed laser beam is focused onto the surface of a sample, where high energy density is delivered within short time duration. Consequently, a small volume of material of the target is heated and evaporated into the surrounding gas, producing a material plume above the target surface. The plume can continue to absorb laser energy becoming further ionized into the state of plasma. The optical emission of the plasma is then collected by a spectrometer. The obtained emission spectrum recorded by a photo-detector can thus be used for qualitative or quantitative elemental analysis of the target.

Brief historical review of the development of LIBS technique

Laser-induced spark emission can be considered as the precursor of LIBS. In 1962, two years after the first ruby laser, Brech and Cross demonstrated the first useful laser-induced plasma on a surface [1]. The first analytical use of laser-induced plasma for spectrochemical analysis of surface was reported in France in 1963 [2], which was considered as the "birth" of the LIBS technique [3]. Subsequently, laser-induced plasma was not only considered as the result of laser sampling but also as the emission source for LIBS. However, for a quite long time, LIBS was relegated to merely a scientific research topic, with published literature devoted more to study the fundamental characteristics of laser plasma than to its analytical capabilities [4].

Starting in the early 1980s, there has been renewed interest in LIBS. The first fast developments of LIBS as an analytical technique can be traced to the works of Radziemski and Cremers [5-8] and their co-workers at Los Alamos National Laboratory. It was also this group at first coined the acronym LIBS for laser-induced breakdown spectroscopy in Ref. 9. The renewed interest in LIBS can be related to several factors. Firstly, there was a

need for new methods of analyzing materials under unsuited conditions for the commonly used analytical methods at that time. Secondly, there were substantial technological improvements of lasers (reduction in size and weight, increase of power, etc.), spectrographs and detectors [4]. Since the 1990s, LIBS has undergone a dramatic progress towards becoming a viable technique for both laboratory and field analysis. In a 2004 review article by Winefordner et al., LIBS has been described as "a future super star" [10].

In the present day, LIBS has been widely investigated and developed for a variety of applications, such as the environmental [11-13], industrial [14-16], geological [17-19], biological [20-22], archaeological [23-25], and forensic [26-28] applications. The integrations by the NASA and the ESA of a LIBS module in their Mars exploration rovers highlights the application of LIBS for space exploration [29-33]. The Chinese first Mars mission HX-1 will also be launched in 2020 with a LIBS instrument.

LIBS as an analytical technique: capabilities and limitations

What renders so wide the range of applications of LIBS is preliminarily its unique and attractive features. Like other techniques of atomic emission spectrometry (AES), LIBS presents some advantages compared with some non-AES-based techniques of elemental analysis, for instance the ability to detect all elements and the capability of simultaneous multi-elemental detection. In addition, LIBS has many specific advantages compared with conventional AES-based techniques, thanks to the use of the laser radiation-induced spark rather than a physical device such as a pair of electrodes to create the plasma [4].

Any kind of substance in gas, liquid and solid state, can be analyzed with simple or even without sample preparation in air, under water, and in extreme conditions such as high temperature and pressure [34]. The high analysis speed and remote sensing capabilities offer strong potentials for LIBS for in-situ [35], standoff [36], and online analyses [37]. In addition, laser pulse induces a limited damage on the sample surface by removing a small amount of material in the order of tens to hundreds of nano-grams, which is appropriate for the precisely localized or micro surface analysis [38,39]. Finally, LIBS can be easily coupled with other spectroscopic techniques, for example Raman

spectroscopy or laser-induced fluorescence (LIF) [40,41]. Now the fast development in instrumental capabilities and knowledge on fundamental aspects of laser-induced plasma has allowed LIBS for a large expansion into laboratory as well as industrial applications [42].

Although LIBS has demonstrated its versatility and attractive features, from the analytical point of view, the performance of quantitative analysis may still be considered as its Achilles' heel [43]. A major factor affecting LIBS quantitative performance is the matrix effect. Obviously, such effect also exists for other plasma-based atomic emission spectroscopy such as ICP, but it is in general more severe for LIBS due to direct laser sampling of materials in different phases. Moreover, in terms of the usual analytical figures of merit (limit of detection, accuracy, precision), LIBS is still generally less competitive than other established laboratory-based analytical methods [44].

From a fundamental point of view, the current limitations of LIBS can be attributed to several factors. The first one to mention is the complex nature of the laser-sample interaction processes, which depends on both the laser characteristics and the sample material properties. The second one is the complex time- and space-evolution of laser-induced plasma [43]. Together, these may cause undesirable matrix effects. Although the principle of LIBS operation is quite simple, the physical processes involved in the laser-matter interaction and plasma excitation-ionization are quite complex and still not completely understood [45]. Therefore, ways of alleviating these problems rely upon the detailed description of the mechanisms involved in plasma evolution and the consequent emission characteristics, which depend mainly on the experimental conditions in which the ablation is carried out. Indeed, emission spectrum features are correlated to the specific interaction of the laser pulse with the sample, as well as to the dynamics of the produced plasma [46].

On the other hand, it is worth mentioning that most conventional analytical techniques inherently require significant amount of works to treat the samples to achieve good analytical results. All other standard techniques, including ICP and XRF, rely on rigorous sample preparation protocols [42]. For LIBS, it is clear that applying a complex

treatment to the sample is to give up one of the most attractive advantages of the LIBS technique. However, proper adapting a sample for LIBS measurements could greatly increase the capacity of LIBS to achieve the figures of merit that any good analytical tool should have [42]. Now, various sample treatment and preparation methods have been used for LIBS in different analytical applications, such as the analysis for liquids [47], loose powders [48] and biological samples [49].

Previous works and objectives of the present thesis

Previous works of the research team from the ILM, Lyon 1 University can be principally divided into two parts: fundamental studies of laser-induced plasma as a spectroscopic emission source, and developments of new methods to improve LIBS analytical capabilities. Particularly, in the fundamental aspect of LIBS, the influences of the experimental conditions (laser wavelength, fluence and ambient gas) on the properties of plasma have been systematically investigated in the framework of two PhD thesis [50,51]. The focus of these works was on plasmas induced on a metallic aluminum target [52-58]. The first part of my thesis is thus a continuation and extension of these works on a dielectric material (glass for instance), as quite different properties can be expect for plasmas induced on these two types of materials, which will lead to specific considerations when optimizing experimental conditions for their LIBS analyses.

Meanwhile, in the analytical aspect of LIBS, a so-called surface-assisted method was developed in our group. And this method has been applied for the elemental analysis in viscous liquids (lubricating oils) [59-61] and soft materials (sunscreen creams) [62]. The key benefits of this method were demonstrated with a sub-ppm sensitivity and a reduced matrix effect for the analysis of materials that is usually limited by the low efficiency of direct laser ablation. The second part of my thesis is to generalize the surface-assisted LIBS technique to the quantitative analysis of powders, as well as to the classification of wines. Such generalization can find much wider applications in important areas such as environmental pollution detection, industrial process, food security control and so on.

The objectives of the present thesis are therefore:

1) Provide an extensive characterization of the plasma induced on glass samples, as a function of the laser wavelength, infrared (IR) or ultraviolet (UV), and the ambient gas, air or argon, to get a better knowledge on plasma to help on the choice of experimental parameters for LIBS analysis of glass-like materials such as gemstones.

2) Apply the surface-assisted LIBS technique for the quantitative analysis of powder samples (cellulose, alumina and soils) with particle size in the range of several tens of micrometers. Special attentions will be focused on the figures-of-merit, matrix effects, and normalization approaches in LIBS analysis.

3) Apply the surface-assisted LIBS technique for the classification of French wines according to their production regions. Two classification models based on the principal component analysis (PCA) and random forest (RF) will be used for the classification.

Structure of the thesis manuscript

After this general introduction, the following manuscript is divided into four Chapters. In Chapter 1, I will describe the theoretical background of laser-induced plasma as a spectroscopic emission source and LIBS as an analytical technique, which is necessary for a good understanding of the presented results in the next chapters. In Chapter 2, I will present the work on the characterization of ablation plume induced on glasses by IR or UV laser pulse in an ambient gas of air or argon. The analytical performance for glasses is also studied in terms of signal-to-noise ratio, and self-absorption behavior of the plasmas induced in the different conditions. In Chapter 3, I will present the work on the quantitative analysis of powder samples with surface-assisted LIBS. Calibration graphs are built to deduce the figures-of-merit parameters and to assess the matrix effect. The effects of spectrum normalization with an internal reference are also presented. In Chapter 4, I will present the work on the classification of French wines according to their production regions with surface-assisted LIBS. The classification is realized by using a non-supervised and linear method of PCA, and a supervised and nonlinear method of RF. Finally, a general conclusion and perspective of the thesis manuscript will be given.

Chapter 1. Theoretical background of laser-induced plasma and laser-induced breakdown spectroscopy

As mentioned in the general introduction, LIBS is a versatile technique that has many attractive features in a wide range of applications. However, LIBS has some drawbacks when considering quantitative aspects such as the limit of detection, accuracy and reproducibility. From a fundamental point of view, this can be due to the complex nature of the laser-sample interaction process together with the time- and space-evolution of laser-induced plasma [43]. Indeed, as a spectroscopic emission source for LIBS application, laser-induced plasmas are quite specific compared to other plasmas (discharge, inductively coupled plasma…) due to its violent expansion into the ambient gas. Therefore, the description of the mechanisms involved in plasma evolution and the consequent emission characteristics represents one of the key points for LIBS as an analytical technique [63].

In this chapter, we will first describe the physical backgrounds to understand the laser-induced plasma from its generation to its propagation into the ambient gas. The mechanisms of laser ablation, as well as the processes of the post-ablation laser-plasma interaction, will be presented. Secondly, we will describe the characterization of laser-induced plasma with the optical emission spectroscopy. The methods of determination of the physical parameters of plasma, including electron density and electron temperature, will be presented. Thirdly, we will focus on the analytical aspects of LIBS, discussing several important issues studied in this thesis, including the calibration procedures, the figures-of-merit in quantitative LIBS, and the matrix effects as well as normalization approaches in LIBS analysis.

1.1 Laser-induced plasma as a spectroscopic emission source

1.1.1 General description of the laser-induced plasma

Laser-induced breakdown is a well-known phenomenon, which leads to a strongly ionized gas commonly named laser-induced plasma. Such plasma occupies a particular place in the scales of temperature and density for plasmas as shown in Fig. 1.1 [63,64]. By using a typical nanosecond pulsed laser with fluence in the order of 10 J/cm^2 and corresponding irradiance in the order of 10 GW/cm^2, the initial temperature and initial electron density of laser-induced plasmas can be typically in the range of 10^4 to 10^5 K, and 10^{17} to 10^{19} cm^{-3} respectively [65]. Excitation energies in the order of tens of eV is typically available allowing a large variety of processes to occur for constituents of the plasma, ions, atoms as well as molecules and clusters. Such processes include absorption/emission, ionization/electron capture, dissociation/recombination and formation of molecules, clusters and nanoparticles.

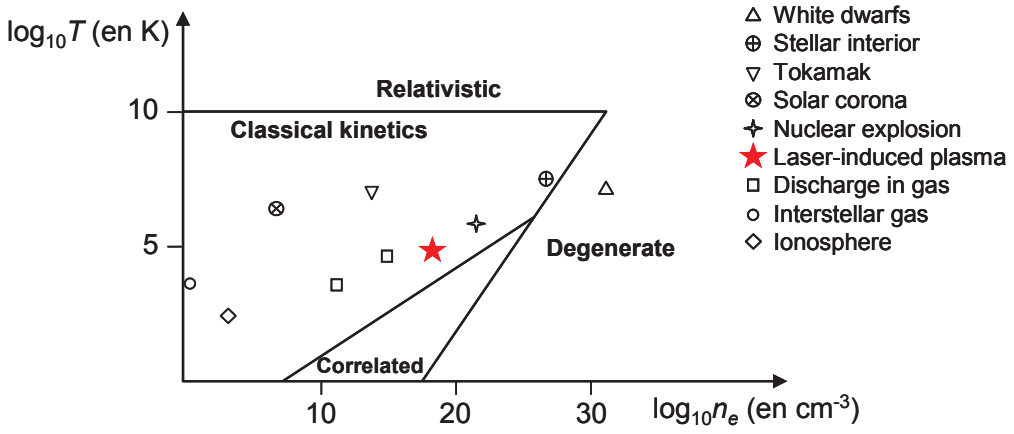

Figure 1.1 Position occupied by laser-induced plasma in the scales of temperature T and electron density n_e, with respect to those occupied by other types of plasmas [64].

Typical structure of the laser-induced plasma in ambient gas

A description of the process of laser-induced plasma requires a collection of basic terms being first specified before they will be properly used in this thesis. The initial process begins with the ablation laser pulse impacting on the surface of the target. As it is often the case for LIBS, we consider that the ablation laser pulse is sent to the target surface

along its normal direction. The ambient gas fills the environment where the laser ablation occurs. Usually for LIBS, the ambient gas is the atmospheric air at the room temperature and one atmosphere pressure.

A description of a typical spatial structure of the laser-induced plasma in ambient gas is shown in Fig. 1.2 [51]. In such description, the vapor is the gas-phase material removed from the target, which is composed of electrons, ions, atoms and other forms of the material such as droplets and solid fragments. For example, when aluminum is ablated, an aluminum vapor is produced. The shockwave is a discontinuity (in the thermodynamic point of view) propagating into the ambient gas. The shockwave is induced when the removed material (the vapor) is ejected out the target surface with a velocity larger than the speed of the sound in the ambient gas. The shocked gas is the part of the ambient gas left behind the shockwave. The thermodynamic property, as well as the optical property of the shocked gas can be dramatically changed due to the passage of the shockwave. The ensemble vapor and shocked gas is referred to the plume. This definition emphasizes the fact that the plume corresponds to a gas with a substantially higher temperature than the initial ambient gas, and that it efficiently emits visible radiations (continuum, atomic, ionic or molecular emissions). When the plume is significantly ionized, it can be considered as a plasma, denoted actually as a laser-induced plasma. A more detailed description of the structure of the laser-induced plasma can be found in Ref. 66 and 67.

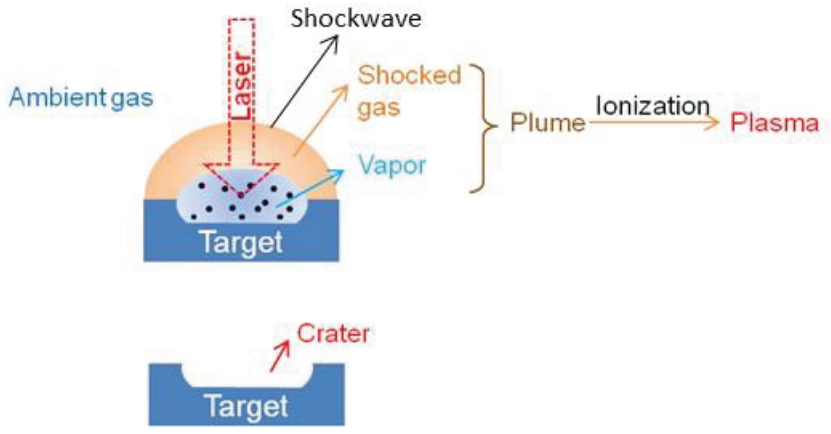

Figure 1.2 Illustration of the spatial structure of laser-induced plasma in ambient gas [51].

When the plume disappears, a crater remains on the surface of the target where the laser pulse was impacted. It is noteworthy that the crater does not correspond to the state of the target surface immediately after the rejection of the vapor; indeed, the ablated materials can eventually deposit back on the target surface contributing therefore to the morphology of the final crater.

With the principal used terms specified, we will describe in the following sections the generation and the evolution of the laser-induced plasma.

Processes in the generation and evolution of the laser-induced plasma

Several steps can be distinguished to describe the generation of the ablation plasma and its subsequent evolution into the ambient gas. As shown in Fig. 1.3, the process starts at the instant when the leading edge of the laser pulse reaches the target surface [63]. Some energy of the incident laser pulse is first absorbed by the material inducing microscopic as well as macroscopic changes in the material. In particular, if the laser fluence or laser irradiance exceeds the ablation threshold, a phase transition occurs in the irradiated volume leading to the generation of a vapor. This vapor, which can be neutral or ionized, interacts with the tailing edge of the incoming laser pulse in the case of ablation with nanosecond or longer laser pulse duration. The high density and temperature and the initial presence free electrons inside the vapor for efficient laser energy absorption leading to a high degree of ionization. A plasma is thus generated above the target surface, and a crater is left behind it.

The plasma then expands into the ambient gas and interacts strongly with it. Since the laser pulse may still be present during the early stage of the plasma expansion, the so-called laser-supported absorption wave (LSAW) [68] dominates the propagation of the plasma into the ambient gas. After the termination of the laser pulse, the resulting system continues to expand into the ambient gas. Relaxation processes, especially radiative decays, take place including the spectral emission from the plasma, which is the basis of the LIBS technique. The plasma finally condenses itself. A typical timescale of the development of the sequential processes during the lifetime of the plasma is shown in Fig. 1.3. In this

figure, the variations of the electron density and temperature are also indicated. The time interval when the LIBS measurement is usually taken place is especially specified. In the following sections, we will provide a more detailed description of the mechanisms of laser ablation, as well as the processes of post-ablation interaction between the plasma and the laser pulse.

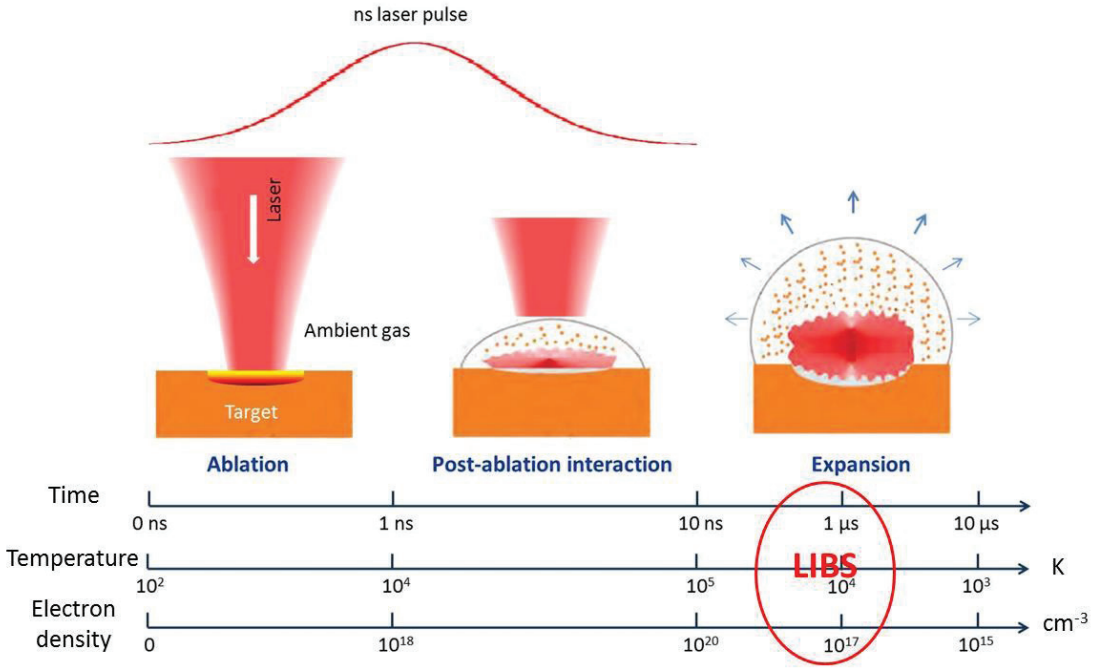

Figure 1.3 Sequential events of the generation and evolution of a laser-induced plasma together with the time scales of the variation of the electron density and temperature in the plasma [63].

1.1.2 Laser ablation

Laser ablation is the process of material removal and formation of a vapor more or less ionized following the impact of a laser pulse on the surface of a target material. Different mechanisms can lead to laser ablation according to the optical, thermal and mechanical properties of the target and also according to the characteristics of the incident laser pulse, wavelength, fluence, and pulse duration [69]. For LIBS measurement, Nd:YAG lasers are typically used because of their reliability and efficiency for ablation on any material with easily generated harmonics from the near ultraviolet (UV) to the near infrared (IR). The typical pulse duration of a Nd:YAG laser ranges from several to tens of nanoseconds. Typical fluence used in LIBS is in the order of 10 J/cm^2, which corresponds to an

irradiance of 10^9-10^{10} W/cm^2. The available wavelengths with the fundamental and the harmonics of a Nd:YAG laser are listed in Table 1-1 together with the corresponding photon energy. Besides the incident laser pulse, the ablation process can also be influenced by the property of the ambient gas [70]. In most cases, LIBS measurement is performed in an ambient gas at the atmospheric pressure, with the ambient air or an introduced gas, such as argon or helium. In the present thesis work, we have performed the LIBS measurement on glasses with two different ablation laser wavelengths of 1064 nm and 266 nm, and in two different ambient gases, air and argon, in the atmospheric pressure.

Table 1-1 Available wavelengths with a Nd:YAG laser associated to harmonics generation together with associated photon energy.

Wavelength/nm	Photon energy/eV
1064	1.17
532	2.33
355	3.49
266	4.66

Mechanisms of laser ablation

In general, laser ablation can be due to one of the following mechanisms: photothermal ablation, photochemical ablation and photophysical ablation [71]. The first two types of ablation are distinguished by the mechanism of laser radiation absorption by the material, and the third one corresponds to the case where both the photothermal and the photochemical process play an important role in the ablation. Although LIBS can concern materials in all the phases, solid, liquid and gas, the ablation of solids is most studied and often representative for the majority of involved processes, of the ablation processes of the different phases of material. In the following, we will address more specifically the laser ablation of solid-state materials.

In the photothermal ablation, the laser energy is first absorbed by free electron available in the material. Electron-lattice coupling transfers then the absorbed energy to

the matrix. In solid-state materials, such coupling has a time constant in the order of a picosecond. Therefore, for a nanosecond laser pulse, the pulse duration is much longer than the energy coupling process from the electron to the matrix, in such way that the laser pulse can be considered as a heat source in the ablation process. The temperature rising in the volume touched by the heat transfer can result in the surface material melting and vaporization, which leads to the formation above the target surface of an ablation vapor. The initial temperature of the formed vapor is essentially determined by the vaporization temperature of the ablated material. The thermal ablation is especially suitable to describe the ablation of metals by nanosecond laser pulses [72], because of the availability of initial free electrons and the long duration of the laser pulse. For other types of materials (such as dielectrics or polymers), additional mechanisms are needed to create initial free electrons, for example by multiphoton ionization or ionization from default levels.

Photochemical ablation occurs when the photon energy of the ablation laser is high enough or when multiphoton transitions are sufficiently efficient (in the case of intense femtosecond laser for instance), so that the optical excitation results in direct bond breaking in the volume of the material touched by the laser pulse. Such photochemical dissociations build up mechanical stresses in the touched volume, which leads to material removal through fragmentation. It takes place in principle without any change in the temperature of the target surface. The photochemical ablation is often suitable to describe ablation of dielectric and polymeric materials. UV nanosecond laser pulse or femtosecond laser pulse is often efficient to induce photochemical ablation.

As already mentioned above, photophysical ablation occurs when the both photothermal and photochemical mechanisms contribute to the ablation process. It corresponds to ablation with both thermal and non-thermal processes [71]. In such ablation, the photochemical process creates initial free electrons, which allows the photothermal process to transfer efficiently the absorbed laser energy to the matrix, leading to its fusion and vaporization. Ablation of dielectric or polymeric materials with nanosecond laser can often be described by the photophysical process. The existence of

default energy levels in dielectric materials or metallic trace elements with low ionization potential in polymeric materials facilitates the ablation of these materials even for infrared ns laser pulses with moderate pulse intensity. High temperatures in the range of 10^4 to 10^5 K can be reached for the plasma induced from these materials through the photophysical process [65].

1.1.3 Post-ablation laser-plasma interaction

The specificity of ablation with nanosecond pulses comes from the fact that the initiation of the ablation plume within an interval of several hundred picoseconds [73] is much shorter than the duration of the ablation pulse. Even with short nanosecond pulses delivered by a Q-switched Nd:YAG laser (with a typical pulse duration of about 5 ns), the laser pulses last a rather long time after the formation of the ablation vapor over the impacted area of the target surface. Post-ablation interaction between the vapor and the tailing part of the laser pulse represents therefore an important process in the early stage of the plasma expansion, which subsequently determines the morphology and the internal structure of the plume after the end of the laser pulse.

Post-ablation processes of the laser-plasma interaction

In the presence of the laser radiation, several steps can be involved in the post-ablation interaction processes. The solid material is heated first, melts, and then evaporates with further absorption of laser energy. After being evaporated, the vapor begins to expand into the ambient gas, therefore, a shockwave forms and propagates into the ambient gas. As a result, the ablated vapor is surrounded by the shocked gas, as shown in Fig. 1.2.

The expanding vapor as well as the shocked gas can absorb energy from the incoming laser pulse. This corresponds to the plasma shielding effect, which reduces the laser energy deposition to the target surface. The shielding is efficient for ablation under an ambient gas at atmospheric pressure.

Thermal ionization can occur in the shocked gas, increasing its absorption rate. The early stage of the plasma expansion is thus driven by laser-supported absorption waves (LSAW) [68]. The absorption of the laser pulse by the interacting system, which can

include the vapor and the shocked gas, is the key point that determines the subsequent evolution of the plasma.

The expanding vapor above the target surface is ionized by absorbing laser energy. It can also contain ionized ambient gas, which, once ionized, is ingested by the vapor plasma. An absorption zone locates in the front part of the plasma, which can more or less extend into the shocked ambient gas and back into the vapor. Finally, the precursor shock can separate the ensemble of the plume (containing the vapor plasma and the shocked gas) from the ambient gas still in the ambient temperature and pressure. Strong interactions of mechanical, thermal or radiative nature occur between the different parts of the plume. The expansion of the vapor plasma mechanically compresses the surrounding ambient gas, leading to a shocked gas layer behind the precursor shock. Thermal conduction occurs from the hot vapor plasma to the shocked layer. Moreover, radiations emitted by the hot vapor plasma can be absorbed by the surrounding ambient gas, leading to further excitation and ionization. The optical property of the ambient gas can be greatly modified by its interaction with the vapor [58].

The vapor plume and the shocked ambient gas are therefore considered as a hot and partially ionized gas. For nanosecond laser ablation, the photon energy is smaller than the ionization potential of implicated elements, and the laser irradiance is too small for significant multiphoton absorption to happen. The main mechanisms involved in the absorption of laser radiation by such gas correspond to the inverse bremsstrahlung (IB) (free-free transitions) and the photoionization (PI) (bound-free transition) [74]. The total absorption coefficient of the gas is therefore contributed by two processes of single photoionization of excited states and inverse bremsstrahlung.

Laser-supported absorption waves (LSAW)

The laser absorption in the plasma accelerates its propagation toward the laser incoming direction and leads to an anisotropic expansion. Such propagation corresponds to the LSAW. For given laser wavelength and ambient gas, there are three major types of LSAW depending on the laser irradiance. The three LSAW are laser-supported combustion (LSC)

wave, laser-supported detonation (LSD) wave, and laser-supported radiation (LSR) wave [68]. The difference between the three modes of LSAW arises from different roles that the ambient gas plays and the different way it is ionized and it absorbs the laser radiation. For usual laser irradiances used in LIBS (~10 GW/cm^2), LSC and LSD waves are more often ignited. In the following paragraphs, we will present the principal characteristics of LSC and LSD waves in the simplified one-dimension model as exposed in Ref. 68.

Laser-supported combustion wave (LSC)

Laser-supported combustion waves can be induced at low irradiance. As shown in Fig. 1.4 (left), the laser absorption zone is localized in the vapor plasma behind the layer of shocked gas which is comprised between the precursor shock (or shockwave) and the vapor. The shocked gas remains transparent for the laser radiation. The laser energy is almost fully transmitted through the shocked gas and is absorbed by the vapor above the target and behind the shocked gas. Consequently, the vapor is efficiently heated to a high temperature and pressure as shown in Fig. 1.4 (c: left) and (d: left). In contrast, the shocked gas remains at a low temperature. The shocked gas is mechanically compressed by the expanding vapor to high pressure and density. The dynamics of the system is maintained by the expansion of the hot vapor. The absorption wave propagates into the cold and high-pressure shocked gas. The main mechanism of propagation is radiative and thermal transfers from the hot plasma to the cold shocked gas. The high pressure and density of the shocked gas increases the absorption of the extreme ultraviolet radiation emitted from the plasma. The part of the shocked gas in contact with the plasma becomes rapidly heated, ionized and is ingested by the LSC wave. Its expansion maintains the pressure that drives the propagation of the shockwave.

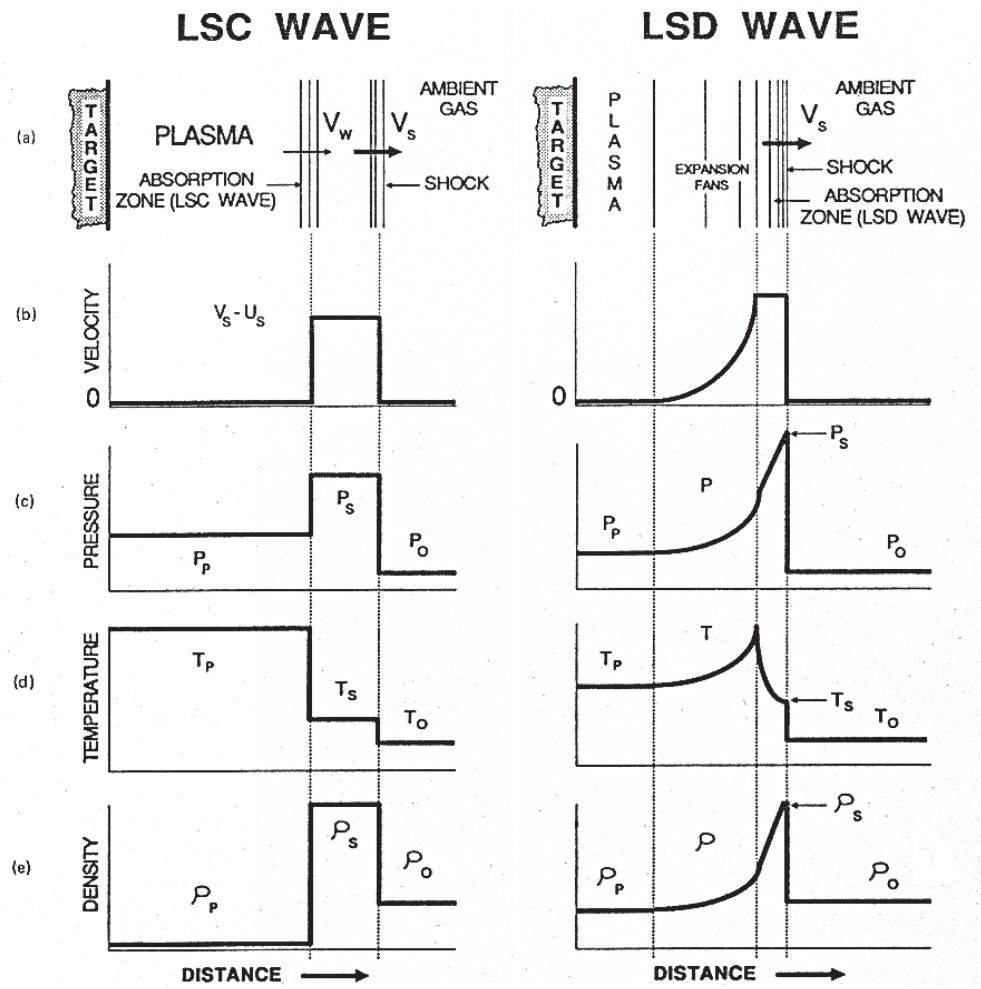

Figure 1.4 Illustration of the structures of one-dimensional LSAWs (a) and qualitative presentation of the profiles of characteristic parameters of the wave, velocity v (b), pressure P (c), temperature T (d) and density ρ (e). The subscribe P is used for the vapor plasma, S for shocked gas and 0 for the ambient gas. Reproduced from the Ref. 68.

Laser-supported detonation wave (LSD)

As the laser irradiance increases, a threshold value will be reached beyond which the shocked gas will be ionized due to significant absorption of the laser radiation. The mode of propagation becomes dominated by the LSD wave, as shown in Fig. 1.4 (right). An absorption zone is found just behind the precursor shock inside of the layer of shocked gas [Fig. 1.4 (a: right)]. No abrupt separation exists between the shocked gas and the vapor plasma. Instead, the pressure, the temperature and the density continuously vary between the vapor and the shocked gas. The propagation of the LSD wave is driven by the absorption of laser energy by the shocked gas. Higher velocity can be found for the

shockwave propagation than in the case of the LSC wave as shown in Fig. 1.4 (b: right). This implies that there is an accelerated propagation along the laser axis of the plasma with LSD. The consequence of laser absorption by the shocked gas is also a layer of gas with higher pressure, temperature and density than in the vapor behind the shocked gas layer. The shielding of the laser radiation by the shocked gas leads to a vapor with lower pressure and temperature than in the case of the LSC wave as shown in Fig. 1.4 (c: right) and (d: right).

Transition between different LSAWs: effect of irradiance and wavelength

As mentioned above, the transition between the different types of LSAWs is controlled by the role of the shocked gas in the absorption of laser radiation. However, the absorption properties of a given gas not only depend on the wavelength of the laser pulse as we discussed above, but also on its thermodynamic state determined by its interaction with the shockwave and the vapor. Such interaction critically depends on the initial energy of the vapor, which is in turn determined by the laser pulse irradiance. The laser wavelength λ and laser irradiance I appear therefore as two pertinent parameters, which provide a practical way to control the regimes of LSAW.

Figure 1.5 shows the characteristic velocities, pressures and temperatures that can be found in different regimes of LSAW [68]. By measuring these characteristic parameters as a function of the laser irradiance, the irradiance ranges corresponding to each type of LSAW can be determined as shown in Fig. 1.5(a). It is important to remark that in Fig. 1.5, the irradiance ranges determined for different LSAW regimes are associated to the wavelength of a CO_2 laser at 10.6 μm in the infrared and in the one-atmosphere ambient air. When the wavelength changes, with the absorption coefficient scaling roughly as λ^2 to λ^3 [63], a correction factor has to be applied in order to find the good indication of the irradiance ranges for the different regimes of LSAW.

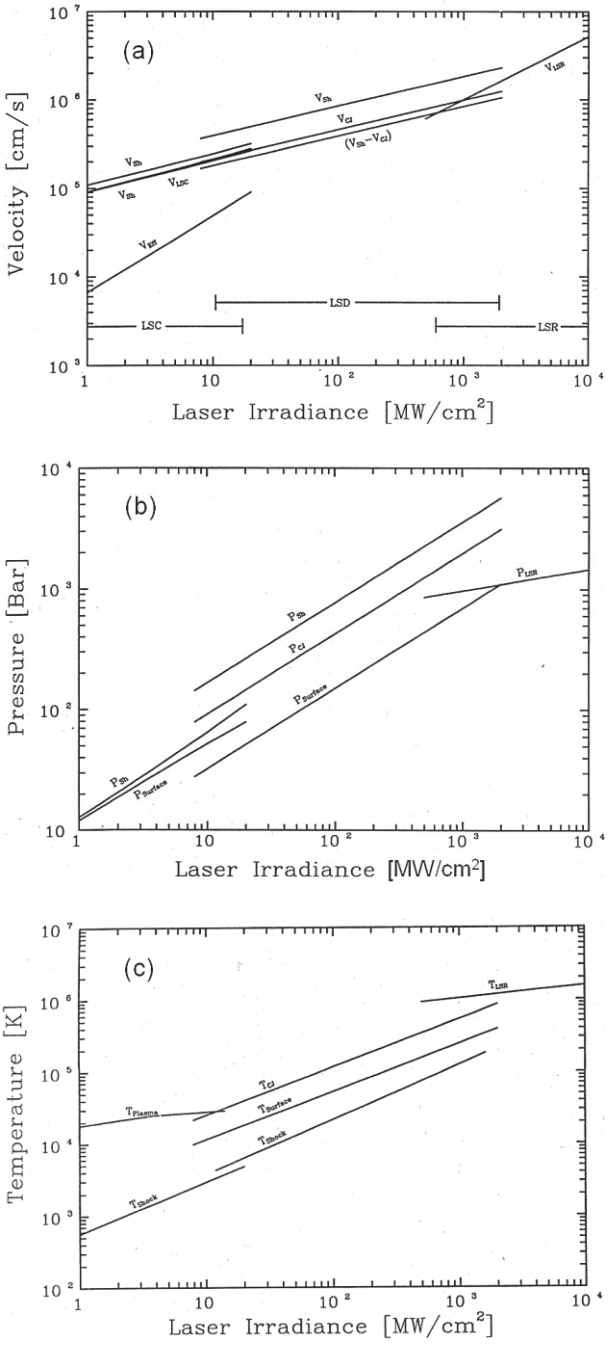

Figure 1.5 Characteristic parameters for plasma expansion into an ambient gas of atmospheric air as a function of the laser irradiance of a CO_2 laser at 10.6 μm. Different irradiance ranges for the three modes of LSAW are also indicated. Reproduced from the Ref. 68.

For typical LIBS applications, a Nd:YAG laser is used for ablation with an irradiance in the range of 10 GW/cm². If the fundamental at 1.064 μm is used, a correction factor can be apply on the irradiance scale of Fig. 1.5 for a rough estimation of the irradiance ranges corresponding to the different LSAW regimes. Such estimation indicates that in a

typical LIBS experiment, either LSC or LSD wave can be induced according to the detailed experimental parameters concerning the laser irradiance and wavelength as well as the background gas (nature and pressure). In the literature, LSD has been observed for a copper plasma induced by a 1.064 μm pulse in an argon ambient gas with laser fluence and irradiance of 15 J/cm² and 7.3 GW/cm² respectively [75]. Such irradiance corresponds well to the range of irradiance for LSD excitation indicated in Fig. 1.5 once the irradiance scale has been multiplied by a factor of between 100 and 1000.

Effect of the LSAW on the propagation of the plasma into the ambient gas

The propagation behavior of the plasma is sensitively influenced by LSAWs. As mentioned in the above discussions, during the LSAW, laser energy is supplied to the plume. However, in different types of LSAW, the laser energy is absorbed in different regions of the plume. For LIBS, measurements take place at a rather long delay after the post-ablation interactions and the most significant effect is related to the morphology of the plasma left by LSAW. This morphology includes the geometrical form of the plume, the profile of the electron density and temperature, and the spatial distribution of the different species in the plume [52-56]. The morphology of the plume in the typical time range of the LIBS measurements is determined in a large extent by the one right after the LSAW, since no more energy is provided to the plume. In LSC, the absorption takes place in the central part of the plume, while in LSD it takes place in the front region of the plume. As consequence, LSC wave is expected to lead to a nearly spherical plume. On the other hand, LSD wave can lead to an elongated form of the plume due to the accelerated propagation of the shocked gas with an efficient absorption of laser energy. Accordingly, the distributions of electron density, of temperature as well as the spatial distribution of various species in the plume can be also significantly changed for the different types of LSAW.

We can thus conclude that the property of the laser-induced plasma as a spectroscopic emission source is crucially determined by not only the ablation but also the propagation of the ablation vapor into the ambient gas. The post-ablation interaction between the plasma and the laser pulse depends on the laser parameters, such as the wavelength and

the fluence, and on the ambient gas. In the PhD thesis of Qinli Ma [50] and Xueshi Bai [51] in our group, the influences of laser wavelength, fluence, and the influence of ambient gas on the expansion behavior of the plasma, have been extensively studied with the ablation of a metallic aluminum target. The present thesis of Chapter 2 is the continuation of these research works on a dielectric material, glass for instance, with two different laser wavelengths of 1064 nm and 266 nm and in different ambient gases of air and argon. The obtained results will be presented and discussed in Chapter 2.

1.2 Plasma characterization with optical emission spectroscopy

Plasma diagnostic is considered as the basis of LIBS, because most of the LIBS information comes from the emission lines of the plasma. The optical emission spectroscopy has become a powerful tool for the fundamental studies of plasma [76]. In this section, we will describe the characterization of laser-induced plasma by the optical emission spectroscopy. The methods of determination of the electron density and temperature will be presented in detail.

1.2.1 Assumptions in the methods for plasma characterization

The description of the plasma state and the evaluation of its essential physical parameters are strictly connected to the concept of thermodynamic equilibrium [43]. For a plasma to be in complete thermodynamic equilibrium, all processes are balanced and characterized by a single temperature. Therefore, the process of excitation of atoms by collisions with electrons is equal to the reverse deactivation process (collisions of second kind), collisional ionization is equal to three-body collisional recombination, and radiation emitted is equal to the radiation absorbed [43]. As mentioned above, laser-induced plasmas are spectroscopic sources that experience a fast temporal evolution of their characteristic parameters, and have spatial distributions with significant gradients. In LIBS studies, there are two basic assumptions when using the emission spectroscopy method for plasma characterization: the local thermodynamic equilibrium and the optically thin spectral line emission.

Local thermodynamic equilibrium (LTE)

The most frequently used methods for the determination of the plasma temperature are based on the application of two equilibrium relations. The first one is the Boltzmann equation, which describes the population densities N_j^z of excited energy levels as a function of temperature T [77]:

$$\frac{N_j^z}{N^z} = \frac{g_j e^{-\frac{E_j^z}{kT}}}{U^z(T)}. \tag{1-1}$$

In Eq. (1-1), the superscript z refers to the ionization stage (z=0 for neutral atoms, z=1 for singly-charged ions), N^z is the number density, E_j^z and g_j^z are the energy and degeneracy of the level, $U^z(T)$ is the partition function and k is the Boltzmann constant. Secondly, the Saha equation relates the densities of subsequent ionization species for a temperature T [77]:

$$\frac{N_e N^z}{N^{z-1}} = \frac{2U^z(T)}{U^{z-1}(T)}\left(\frac{2\pi mkT}{h^2}\right)^{3/2} e^{-\frac{E_\infty^{z-1} - \Delta E_\infty^{z-1}}{kT}} \tag{1-2}$$

where N_e is the electron density, E_∞^{z-1} is the ionization energy of species $z-1$ for isolated systems, ΔE_∞^{z-1} is the correction of this quantity for interactions in the plasma, h is the Planck's constant and m is the electron mass. The applicability of these equations relies on the validity of local thermodynamic equilibrium (LTE), a state in which the temperature of the Boltzmann and Saha equations is equal to that of the Maxwell–Boltzmann velocity distribution of free electrons [78]. Moreover, for LTE, Kirchhoff's law of radiation is also valid. This law establishes a connection between the emission coefficient or emissivity ε_λ ($\mathrm{Wm^{-3}\,sr^{-1}nm^{-1}}$) and the absorption coefficient k' ($\mathrm{m^{-1}}$), and is given by [78]:

$$\frac{\varepsilon_\lambda(\lambda)}{k'(\lambda)} = B_\lambda(\lambda, T) \tag{1-3}$$

where $B_\lambda(\lambda, T)$ is the intensity ($\mathrm{Wm^{-2}\ sr^{-1}\ nm^{-1}}$) of the equilibrium radiation field (blackbody radiation) at temperature T, given by Planck's law. The subscript λ in ε_λ and B_λ indicates that these are radiant quantities, defined per unit wavelength.

For LTE to hold in a plasma, the collisions with electrons have to dominate over the radiative processes, this condition requiring a sufficiently large electron density. A criterion proposed by McWhirter [79] was based on the existence of a critical electron density for which collisional rates are at least ten times the radiative rates. For an energy gap difference ΔE (eV) between the transition levels, the criterion for LTE is:

$$N_e \geq 1.6 \times 10^{12} T^{1/2} (\Delta E)^3 cm^{-3}. \quad (1\text{-}4)$$

In most cases, the critical electron density values were typically in the range 10^{15}-10^{16} cm^{-3}. For laser-induced plasmas generated with different experimental conditions, the plasma electron density is higher than the critical value for the largest energy gap of the transitions used in the experiment, supporting the existence of LTE.

It should be noted that the McWhirter criterion is a necessary but not sufficient condition for LTE to hold. The existence of LTE in LIPs has been questioned due mainly to their fast evolution and temperature decrease. Two more criteria to check the existence of LTE have been used [76], based on the experimental measurement of the plasma temperature. One of them is the comparison of the excitation and ionization temperatures, deduced from the Boltzmann and Saha–Boltzmann equations, respectively. The other criterion is the agreement between the Boltzmann distribution and the experimentally measured line intensities, which is reflected in the linearity of the Boltzmann plot (see section 1.2.3 for more details).

Optically thin spectral line emission

The methods used for determining the plasma parameters are also based on the optically thin emission of spectral lines. The determination of the electron density by the Stark broadening effect (Section 1.2.2), as well as the measurement of temperature using the Boltzmann and Saha-Boltzmann equations (Sections 1.2.3) require that the spectral lines used are optically thin. If this condition is not satisfied, i.e., if the lines used for characterization suffer from self-absorption, their line profiles are saturated, showing distorted widths and areas that lead to wrong values of electron density and temperature [76].

Several methods have been used to verify that the spectral lines are emitted in the optically thin condition. A simple method is based on the measurement of the relative intensities of lines belonging to resonance emission lines, for example the N I multiplet [9] or the three O I lines [80]. Optically thin conditions can also be verified by checking that the non-resonance emission lines selected showed the same line width at the different axial positions and power densities studied [81]. Indeed, if self-absorption occurs, it should be noticeable at high power density and the line widths would change at different axial positions because of different plasma densities. A more complex but accurate method for the estimation of the degree of self-absorption of a spectral line is based on the calculation of the growth curve, i.e., the intensity vs. the concentration curve, starting from the transition parameters, the plasma temperature and the damping constant of the line [82].

1.2.2 Measurement of electron density

Stark broadening

The Stark effect in plasmas is due to collisions of the emitting atoms with electrons and ions, resulting in a broadening of the line and a shift of the peak wavelength. For the determination of electron density, the broadening of emission lines due to the Stark effect has been the most widely used. This method is based on the assumption that the Stark effect is the dominant broadening mechanism, in comparison with the Doppler broadening and the other pressure broadening mechanisms, due to collisions with neutral atoms (i.e., resonance and Van der Waals broadenings) [76].

The theoretical calculations of Stark broadening of hydrogen lines, hydrogenic ion lines and lines of atoms with two or more active electrons are described in detail in the books by Griem [77,83]. These references contain approximated expressions relating the Stark broadening to the electron density. For the linear Stark effect (hydrogen and hydrogenic ions) the following equation is provided:

$$N_e = C(N_e, T)\Delta\lambda_s^{3/2} \qquad (1\text{-}5)$$

where $\Delta\lambda_s$ is the full width at half maximum (FWHM) of the line width due to the Stark effect and $C(N_e, T)$ is a coefficient that is only a weak function of electron density and temperature. For atoms with two and more active electrons, the FWHM of the line broadening due to the quadratic Stark effect is approximately given by [83]:

$$\Delta\lambda_s \approx 2[1 + 1.75A(1 - 0.75R)]w\frac{N_e}{N_e^{ref}}. \quad (1\text{-}6)$$

In this equation, w is the electron-impact half width, A is the ion broadening parameter, which is a measure of the relative importance of the collisions with ions in the broadening, N_e is the electron density and N_e^{ref} is a reference electron density, usually of the order of 10^{16} or 10^{17} cm^{-3}, at which the parameters w and A are measured or calculated. The parameters w and A are weak functions of temperature. R is the ratio of the mean distance between ions and the Debye radius. Eq. (1-6) is valid only in the range $A \leq 0.5$, $R \leq 0.8$. Also, this equation is valid for neutral emitters; for singly ionized emitters, the term $0.75R$ should be replaced by about $1.2R$.

Eqs. (1-5) and (1-6) were used to determine the electron density from the experimentally determined line widths of selected lines. The necessary broadening coefficients or parameters at a given plasma temperature can be found in Refs. 77 and 83.

For accurate measurements of the electron density, spectral lines with no interference and emitted in optically thin conditions have to be selected. The error of the determined electron density includes the error on the Stark width measurement and the error on the reference Stark coefficients or parameters. In the literature, a variety of lines have been used for the determination of electron density, and the atomic lines coming from the ambient gas, such as Ar, He, H, N, and O were used frequently. The hydrogen and hydrogenic lines are considered as good choices because their Stark coefficients are more accurate. For example, the calculated widths are reliable within 10% for hydrogen, neutral and ionized helium lines, and the higher accuracy of better than 5% is expected for the Hβ line [77].

Stark shift

The electron density of laser-induced plasma may also be determined from the shifts of the intensity maxima of line profiles produced by the Stark effect. To this aim, the measured shifts are compared with the values predicted by the approximated formula in Griem's book [77] that gives the Stark shift d_{Stark} as a function of the electron density:

$$d_{\mathrm{Stark}} \approx \left[\frac{d}{w} \pm 2.00A(1-0.75R)\right] w \frac{N_e}{N_e^{ref}}. \quad (1\text{-}7)$$

In Eq. (1-7), d is the electron-impact shift parameter. The range of validity and modification of the equation for singly charged ion emitters described for Eq. (1-6) apply for Eq. (1-7). The theoretical calculations of the shift parameters have large uncertainties, therefore, the electron densities determined from the Stark broadening are considered more accurate than that from Stark shift. In this thesis, the electron densities were determined by the Stark broadening method with Si I 288.2 nm line (Chapter 2) and with H_α 656.3 nm line (Chapter 3 and Chapter 4).

1.2.3 Measurement of temperature

The Boltzmann equation

The simplest method to determine the plasma temperature by emission spectroscopy is based on the measurement of the relative intensities of two lines from the same element and ionization stage under the assumption that the Boltzman equation [Eq. (1-1)] is valid to relate the population densities of the upper levels of the transitions [77]. Let E_i be the energy of the upper level of each of the two lines (labelled with $i = 1\ or\ 2$) and let us define the quantity $\mathrm{y}_i \equiv \varepsilon_i\lambda_i/(\mathrm{g}_i\mathrm{A}_i)$, where ε_i is the line emissivity ($\mathrm{Wm^{-3}\ sr^{-1}}$) integrated over the line profile, λ_i is the transition wavelength, g_i is the statistical weight of the upper level and A_i is the transition probability. The wavelength-integrated emissivity for a transition of a given emitting species can be expressed, using Eq. (1-1) for the population density, as [78]:

$$\varepsilon_{ji}^{z} = \frac{\mathrm{hc}}{4\pi\lambda} A_{\mathrm{ji}} \frac{N^z}{U^z(T)} \mathrm{g}_j e^{-\frac{E_j^z}{kT}} \quad (1\text{-}8)$$

where c is the speed of light in vacuum and h the Plank constant.

Taking the natural logarithm of y_i, the temperature can be deduced from the equation:

$$\ln\frac{y_2}{y_1} = -\frac{1}{kT}(E_2 - E_1). \quad (1\text{-}9)$$

The wavelengths, level energies, degeneracies and transition probabilities were taken generally from the atomic spectroscopic databases. The temperature resulting from the Boltzmann equation has also been called excitation temperature although, in LTE conditions, it should be equal to the electron kinetic temperature. The Boltzmann two-line method presents the advantage of simplicity. It has been used frequently when the samples used to generate the plasma contained elements that have few transitions in the visible region of the spectrum. The main disadvantage of the Boltzmann two-line method is that it may lead to considerable uncertainties of the determined temperatures. From Eq. (1-9), the relative uncertainty of temperature can be roughly estimated by [78]:

$$\frac{\Delta T}{T} = \frac{kT}{E_2 - E_1}\frac{\Delta(y_1/y_2)}{y_1/y_2}. \quad (1\text{-}10)$$

The error on y_1/y_2 comprises the error of the relative intensity measurement and the usually much more important uncertainties on the transition probabilities. If the interest is in the relative temperatures of plasma in different experimental conditions, the uncertainties on the transition probabilities can be excluded in the estimation of the errors of the relative temperature values.

The accuracy of temperature determination from the Boltzmann equation can be improved by measuring a number of different lines. Eq. (1-8) is transformed into:

$$\ln\left(\frac{\varepsilon_{ji}^z \lambda}{A_{ji} g_j}\right) = -\frac{1}{kT}E_j^z + \ln\left(\frac{hcN^z}{4\pi U^z(T)}\right). \quad (1\text{-}11)$$

If a graph is constructed for various lines with the left side of Eq. (1-11) as the ordinate and the upper level energy E_j^z as the abscissa, a straight line is expected. The slope of this line yields the temperature. For a better accuracy, the range of upper level energies in the Boltzmann plot should be as large as possible [78].

In the usual procedure to obtain Boltzmann plots, emission lines from a single element and ionization stage are included. However, it is also possible to construct multi-element Boltzmann plots, including the line intensities from different elements. Two different approaches have been described to use multi-element Boltzmann plots. The first considers that if the raw line intensities are used, under LTE conditions, the data for the different elements should lie on parallel straight lines, whose slope should yield the same temperature [84]. For the second approach, the multi-element Boltzmann plots are constructed from the intensities corrected taking into account the stoichiometry of the plasma, which is assumed the same as that of the sample. With this correction, the data for all the elements is expected to lie on a single straight line whose slope should yield the temperature [85].

The Saha-Boltzmann equation

The limited accuracy of the Boltzmann two-line method for temperature determination is due to the fact that, for two lines of the same ionization species, typically $kT/(E_2 - E_1) \sim 1$ in Eq. (1-10), and the relative error of the ratio y_1/y_2 leads to a similar relative error for temperature. Considerable improvement in the accuracy is obtained if lines of successive ionization stages of the same element are compared with each other, because the effective energy difference is now enhanced by the ionization energy, which is larger than the thermal energy [77]. Combining Eqs. (1-8) and (1-2), the so-called Saha-Boltzmann equation is obtained, which relates the relative emissivities of lines from subsequent ionization stages of the same element to the temperature T and the electron density Ne [78]:

$$\ln\frac{y_2}{y_2} = -\frac{1}{kT}(E_2 - E_1 + E_\infty - \Delta E_\infty) + \ln\left[2\frac{(2\pi mk)^{3/2}}{h^3}\frac{T^{3/2}}{N_e}\right]. \qquad (1\text{-}12)$$

In the Saha-Boltzmann two-line method, the knowledge of the electron density is necessary to determine, using Eq. (1-12), the temperature from the ratio of the wavelength-integrated line emissivities from successive ionization stages. In LTE, the temperature resulting from the Saha-Boltzmann equation is the so-called the ionization temperature, which should be equal to the electron temperature.

A multi-line approach to temperature determination based on the Boltzmann and Saha equations was also developed [86]. If the density N^z of the ionized species ($z \geq 1$) is obtained from Eq. (1-2) in terms of N^{z-1} and substituted into Eq. (1-10), and this procedure is iterated for decreasing z, the following equation, similar to the Boltzmann-plot equation [Eq. (1-11)] can be shown to be valid for the emissivity of any line and ionization stage:

$$\ln\left(\frac{\varepsilon_{ji}^{z}\lambda}{A_{ji}g_j}\right)^{*} = -\frac{1}{kT}E_j^{z^*} + \ln\left(\frac{hcN^0}{4\pi U^0(T)}\right). \tag{1-13a}$$

Eq. (1-13a) allows plotting both neutrals and ions (or any two sequential ionization stages or several ionization stages) on the same plot. This Saha-Boltzmann plot is similar to a Boltzmann plot but, to place neutrals and the different ionization stages on the same plot, it is needed to adjust the abscissas and ordinates of the ion points. The abscissa values of the ions are modified by the addition of the corrected ionization energy to the upper level energies:

$$E_j^{z^*} = E_j^z + \sum_{k=0}^{z-1}\left(E_\infty^k - \Delta E_\infty^k\right) \tag{1-13b}$$

and the ordinates are corrected with the expression:

$$\ln\left(\frac{\varepsilon_{ji}^{z}\lambda}{A_{ji}g_j}\right)^{*} = \ln\left(\frac{\varepsilon_{ji}^{z}\lambda}{A_{ji}g_j}\right) - z\ln\left[2\frac{(2\pi mk)^{3/2}}{h^3}\frac{T^{3/2}}{N_e}\right]. \tag{1-13c}$$

As the correction term in Eq. (1-13c) term depends on temperature as $\ln(T^{3/2})$, which is slower than $1/T$, the temperature can be rapidly determined through an iterative approach.

A multi-element Saha–Boltzmann plot method was also proposed in Ref. 85 for the determination of the temperature and the relative number density in plasmas. The assumptions of the validity of the method include the LTE condition, the conservation of the sample stoichiometry in the plasma and the range of the temperature and the electron density values such that the ionic species with charge >1 can be disregarded. The method is based on a double correction of the ordinates of the usual Boltzmann equation. The first correction term is that of Eq. (1-13c), and does not depend on the element. The

second correction term varies with the element considered and is the same for neutrals and ions. Also, the abscissa values of the ions have to be modified as in Eq. (1-13b).

The methods for temperature determination described above are the most frequently used methods in the literature. In the present thesis, the plasma temperatures were determined by Saha-Boltzmann plot of the emission lines from Ca (Chapter 2 and Chapter 4) and Ti (Chapter 3).

The plasma temperatures can also be determined from the line and continuum emissions, as well as from the molecular emissions. The former one is based on the line-to-continuum intensity ratio, which is suitable for the diagnostics of the early phase of the plasma, since the continuum and line emission are of comparable magnitude, and good precision of line-to-continuum ratio can be obtained [87]. The determination of molecular temperature is based on the Boltzmann plots obtained from the intensities of vibrational bands and rotational lines, corresponding to the vibrational and rotational temperatures, respectively [88]. This method is often used for the late-stage diagnostics of the plasma, since the molecules and radicals are generally formed through recombination when the temperature decreases in the plasma, and therefore the molecular emissions are expected from a plasma with long delays of detection [57].

1.3 Quantitative analysis with LIBS

All the above descriptions, including the initiation and diagnostics of the plasma, and the validation of LTE condition, provide the basis of quantitative analysis using LIBS. As stated by Omenetto et al. in Ref. 43, the quantitative aspects of LIBS may be figuratively considered its Achilles' heel. Also as stated by Mermet et al. in Ref. 89, the acceptability of LIBS is still related to the problem of quantitation, involving accuracy, i.e., repeatability and trueness. In this section, we will focus on the quantitative aspects of LIBS analysis, to describe the basic concepts of calibration and calibration curve, and the figures-of-merit parameters in quantitative analysis. Matrix effects as well as normalization approaches will also be discussed in this section, which are of critical importance in LIBS analysis.

1.3.1 Calibration and calibration curve

In most cases in atomic spectrometry, a calibration procedure is required for providing analyte concentrations in unknown samples. Calibration implies two steps [90]. The first step consists of measuring signal intensities using samples with known concentrations (references) in order to construct a calibration curve. In a second step, the concentration is deduced from the calibration curve using the measurement of the signal intensity from an unknown sample. A so-called "counter or inverse calibration" is therefore performed. When more than two references are used, it is necessary to carry out a regression, which may be of the linear or quadratic (curvilinear) type. Regressions are mostly based on the least-squares method (LSM), which minimizes the sum of the squares of the differences between the experimental data and the computed values. Regression is based on statistics, which implies some consequences because of the LSM selected model [90]. The best calibration curve is that which would provide the closest computed value compared to the experimental one, within an expected concentration range. The rules and guidelines for optimizations of the calibration strategy can be found in a variety of publications [91-93].

The regression model establishes the relationship between the intensities in a LIBS spectrum (predictors) noted (X) and the concentration values (Y) of the analyte. The simplest case of regression model is univariate, which means that only one predictor x per sample is exploited instead of a X-matrix and only the concentration values of one single analyte are predicted, and referenced as y. In this case, both x and y are vectors of dimension N, N being the number of samples exploited for calibration. The corresponding graphical display is the so-called calibration curve, which consists in plotting the measured signals against the analyte's concentrations [94]. In LIBS measurements, the signals correspond usually to the intensity or the peak area of the most relevant lines, which are exempt of spectral interferences and self-absorption effects and with good signal-to-noise ratios.

1.3.2 Figures-of-merit in quantitative analysis with LIBS

Correlation coefficient (R^2) and prediction ability (Q^2)

In order to get a first understanding of the relationship between the physical parameters namely, the peak intensity (or area) on one hand, given by x, and the analyte's concentration on the other hand, given by y, it is common to calculate the correlation factor also called the Pearson coefficient, assuming a linear relationship between x and y, which is given by [90]:

$$R = \frac{\sum_{i=1}^{N}(x_i-\overline{x})\left(\hat{y}_i-\overline{\hat{y}}\right)}{\sqrt{\sum_{i=1}^{N}(x_i-\overline{x})^2}\cdot\sqrt{\sum_{i=1}^{N}\left(\hat{y}_i-\overline{\hat{y}}\right)^2}} \quad (1\text{-}14)$$

where x_i is the value of the LIBS signal for the sample i, and $\overline{x}$ the average value of x_i over the N samples. Similarly, $\hat{y}_i$ is the reference value of the analyte's concentration for sample i, and $\overline{\hat{y}}$ the average value of $\hat{y}_i$ over N samples. The Pearson coefficient can vary between -1 and $+1$. Values close to 0 are synonym of poor correlation while values close to $+1$ reveal strong correlation and values close to -1 reveal strong anti-correlation.

The correlation coefficient R^2, the value of the square of the Pearson coefficient, is more often used. The R^2 factor provides fast information about the correlation of the data and consequently a fast first knowledge about the prediction ability of the model since poor correlation necessarily implies poor predictive ability. The usual requirement for a quantitative analytical technique is $R^2 \geq 0.99$ [90].

Another parameter of figure of merit, Q^2, allows evaluating the ability of a model to predict values of concentrations close to the reference value [95]. Q^2 is given by:

$$Q^2 = 1 - \frac{\sum_{i=1}^{N}(\hat{y}_i-y_i)^2}{\sum_{i=1}^{N}\left(\hat{y}_i-\overline{\hat{y}}_i\right)^2} \quad (1\text{-}15)$$

where $\hat{y}_i$ are the reference values of concentration, y_i the predicted ones, and $\overline{\hat{y}}$ the average value of $\hat{y}_i$ over N samples in the dataset. The values of R^2 and Q^2 can be separately calculated for the calibration, the validation and the test datasets. Ideally, R^2 and Q^2 values should be equal to 1. However, the Q^2 value could be high for the

calibration dataset and for cross-validation, but the related model could have poor predictive ability in the case of external validation, especially in case of a non-linear behavior [96]. Consequently, R^2 and Q^2 are not sufficient to assess the predictive ability of a model.

Accuracy: trueness and precision

It is therefore necessary to estimate the accuracy of a quantitative method [97]. Accuracy simultaneously contains trueness, which is related to systematic error and measured by the value of bias, and precision, which is related to random error and measured by the value of standard deviation. While trueness is simply given by the difference between the value of concentration retrieved after LIBS analysis and the "true" value, precision includes instrument and independent repeatability as well as intermediate precision and reproducibility [98].

Precision is described by the standard deviation (SD) or by the relative standard deviation (RSD in %), which is a very common figure of merit in the framework of LIBS analysis. For a given sample or an ensemble of statistically equivalent samples, assuming N replicate measurements being performed, these two factors are given by:

$$SD = \sqrt{\frac{\sum_{i=1}^{N}(y_i - \overline{y})^2}{N}} \tag{1-16}$$

and:

$$RSD(\%) = \frac{SD}{\overline{y}} \times 100 \tag{1-17}$$

Where y_i refers to the concentration value predicted with the i^{st} replicate measurement, $\overline{y}$ to the average value over the N replicate measurements, and SD to the standard deviation of the y_i predicted concentrations of the N replicate measurements.

Root mean square error (RMSE) and relative error (RE)

Once a quantitative model is built, it provides predicted values of concentrations. Thus, it becomes possible to compare the predicted values with the "true" values. For reference samples, these values correspond to the known concentration values provided for the

samples. Consequently, it is possible to define new figures of merit based on the error of prediction. The root mean square error (RMSE) is thus given by [94]:

$$RMSE = \sqrt{\frac{\sum_{i=1}^{N}(\hat{y}_i - y_i)^2}{N}} \tag{1-18}$$

where $\hat{y}_i$ are the reference values of concentration, y_i the predicted ones, and N the number of samples in the dataset. It should be noticed that the unit of RMSE is identical to the unit of the concentrations y_i. Thus, if the concentrations y_i are given in part per million (ppm), RMSE will be also obtained in ppm. In addition, the quantity $(\hat{y}_i - y_i)^2$ is expected to be higher for the highest concentrations. This means that the high values of concentration have a strong influence on the RMSE value.

Another way to evaluate the error between the predicted and the actual values of concentration consists in calculating the mean relative error defined as [94]:

$$RE(\%) = 100\frac{1}{N}\sum_{i=1}^{N}\frac{|\hat{y}_i - y_i|}{\hat{y}_i}. \tag{1-19}$$

In this case, the percentage error is calculated for each value of concentration. So both low concentrations and high concentrations have the same influence on the result. Therefore, RE (%) appears to be an adequate factor to estimate the ability of a quantitative model to correctly predict the analyte's concentrations.

Uncertainty resulting from the regression

The uncertainty resulting from the regression procedure, also called the limits of confidence, is another convenient way to evaluate the quality of calibration [90]. Assume a linear regression between the values of concentration x and the LIBS signal y, described by the equation $y = bx + a$. It should be noted that the notation here is reversed with respect to that described previously, where x was defined as the LIBS signal and y the concentration value.

The slope (b) of the resulting straight line is given by [90]:

$$b = \frac{\sum_{i=1}^{N}(x_i - x_m)(y_i - y_m)}{\sum_{i=1}^{N}(x_i - x_m)^2}. \tag{1-20}$$

And the intercept (a) is given by:

$$a = y_m - bx_m \tag{1-21}$$

where y_m is the mean value of the LIBS signal, x_m the mean value of the concentrations, N the number of samples and x_i the reference value of the concentration of the sample i. Then, the residual standard deviation between the measured values of the LIBS signal and the values deduce from regression is given by [90]:

$$S = \sqrt{\frac{\sum_{i=1}^{N}(y_i - y_c)^2}{N-2}} \tag{1-22}$$

where y_i is the mean value of the replicates of the measured LIBS signal recorded for a given value of concentration x_i; y_c is the value deduced from regression at the value of concentration x_i and considering the degree of freedom being $N-2$. Because of the uncertainty on the slope and the intercept of the regression line, for a given value of concentration x_0, the corresponding mean value of the LIBS signal y_0 can be determined by the regression law within a confidence limit of $\pm t \cdot s_0$ giving:

$$y_0 = a + bx_0 \pm t \cdot s_0 \tag{1-23}$$

where t is the Student's coefficient $t(1-\alpha/2)$ at a given risk α or at a confidence percentage of $[100(1-\alpha)\%]$ and $N-2$ the degree of freedom. The value of s_0 is given by:

$$s_0 = S \cdot \sqrt{\frac{1}{N} + \frac{(x_0 - x_m)^2}{\sum_{i=1}^{N}(x_i - x_m)^2}}. \tag{1-24}$$

The equation describes two hyperbolas on each side of the straight line that correspond to two confidence bands. Once the confidence bands have been determined, it is necessary to determine the confidence limits for a concentration x_u of an unknown sample, from the measured LIBS signal y_u. After applying relevant approximations [90], two values of concentration x_1 and x_2 can be deduced and given by:

$$x_1 = x_u - \frac{t \cdot S}{b}\left(\frac{1}{p} + \frac{1}{N}\right)^{1/2} \tag{1-25}$$

$$x_2 = x_u + \frac{t \cdot S}{b}\left(\frac{1}{p} + \frac{1}{N}\right)^{1/2} \quad (1\text{-}26)$$

where p represents the number of replicates. The two values x_1 and x_2 correspond then to the uncertainty on x_u due to the regression, and these confidence limits are graphically represented by hyperbolas surrounding the regression line, as shown in Fig. 1.6. Note that the two limits will also depend on the concentration level, i.e. close or far from the limit of detection, as a low uncertainty cannot be expected near the limit of detection [90]. Therefore, this type of analysis about accuracy allows for understanding that the predictive ability of a quantitative model is always better in the middle of the range of concentrations [94].

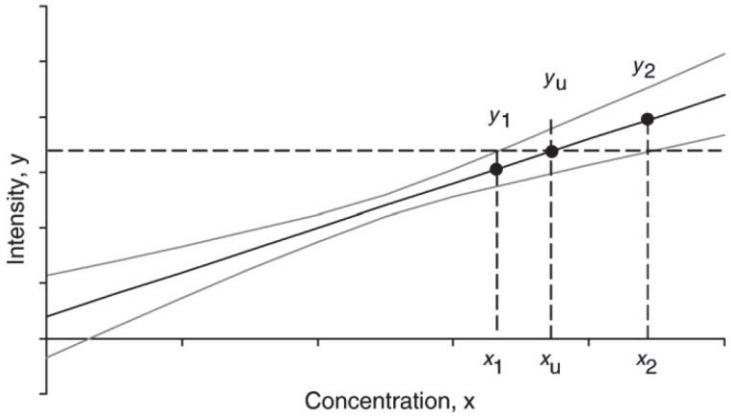

Figure 1.6 Computation of an unknown x_u concentration from the measured y_u intensity, associated with its $x_1 - x_2$ uncertainty range [90].

Limit of detection (LOD) and limit of quantification (LOQ)

The limit of detection (LOD) is widely used in analytical chemistry as an ultimate concentration for which it is possible to provide a statistical evidence of the presence of an analyte. As defined by IUPAC [99], the limit of detection, expressed as a concentration, c_L, is derived from the smallest measure (or signal), X_L, that can be detected with reasonable certainty for a given analytical procedure. The value of X_L is given by the equation $X_L = x_{bi} + ks_{bi}$, where x_{bi} is the mean of the blank measures, s_{bi} is the standard deviation of the blank measures, and k is a numerical factor chosen according to the confidence level desired.

Because the relationship between the measure (or signal) and the concentration is

given by the slope of the calibration curve $m = \Delta c_L/\Delta x_L$, we have $c_L = c_{bi} + ks_{bi}m$ but c_{bi} is typically zero (no analyte concentration in the blank sample) so that $c_L = ks_{bi}m$. This is the formula that is often used to compute the LOD with $k = 3$. Ideally, a $k = 3$ value would correspond to a confidence level of 95% but because s_{bi} is determined from a small number of measurements, a 90% confidence level is more reasonable [3]. The detection limit should be considered as the minimum amount of the analyte that can be present and be determined to be present, rather than the minimum amount of the sample that can be actually measured. For quantification purposes, $k = 10$ and the limit of quantification is given by $LOQ = 10s_{bi}m = 3.3LOD$.

In most LIBS literatures, assuming a linear regression described by equation $y = bx + a$, where y describes the values of the LIBS signal and x the values of concentrations, the definition of the limit of detection the most frequently used is:

$$LOD = \frac{3\sigma_a}{b}. \tag{1-27}$$

And the limit of quantification is generally defined by [97]:

$$LOQ = \frac{10\sigma_a}{b} \tag{1-28}$$

where σ_a is the standard deviation of the background (or analytical blank) and b the slope of the regression curve. It should be noted that definition of LOQ is not unique, and the definition in Eq. (1-28) is the simplest one that is widely used in atomic spectrometry. It is actually an extrapolation of the LOD [97] and it may suffer from severe limitations: lack of Gaussian distribution, insufficient number of measurements, only instrumental repeatability, and presence of outliers. Besides, it is assumed that there is negligible uncertainty on the calibration curve. As defined by EURACHEM, the limit of quantitation is the lowest concentration of analyte that can be determined with an acceptable level of uncertainty [100]. Various definitions and approaches for the determination of LOQ was reviewed by Mermet in Ref. 97.

Finally, it should be mentioned that the experimental response, i.e. the LIBS signal versus the concentration of the analyte might be nonlinear, especially for relatively high

values of concentrations where self-absorption may happen. Consequently, the linear regression could be misfit and a quadratic regression might be advantageous. In the latter case, some figures-of-merit such as R^2, S and the confident limits have to be revisited [97]. In this thesis in Chapter 3, both linear and quadratic regressions were used to build the calibration graphs for powders analysis with surface-assisted LIBS. As figures-of-merit, R^2 was calculated, and the confidence bands were also plotted on the calibration graphs (confidence level 95%). The LOD was extracted from $3\sigma_a/b$, while the LOQ was determined based on the confidence bands of the calibration graphs [97]. This method takes into account the uncertainties due to regression, which is considered more rigorous than the definition of $10\sigma_a/b$ introduced above.

1.3.3 Matrix effects and normalization with an internal reference

Matrix effects in laser sampling-based spectrometry

Matrix effects are of critical importance in several analytical spectroscopy techniques, and LIBS is not an exception [101]. A significantly different signal response can be observed at a given spectroscopic transition of an element present at the same concentration level in two different samples. Such different response can be attributed to differences in the laser-sample interaction, resulting from changes in the ablation mechanism and efficiency, or it can be due to a variation in the physical plasma parameters, namely to changes in the electron temperature and number density, or a combination of both. In other words, like in other methods, the analytical response can be influenced by physical, chemical, spectral, and instrumental causes [101]. The term "matrix effect" is then described as the matrix dependence of analytical signal when analyzing samples of different matrices. A simplified depiction of matrix effects in laser sampling based spectrometry is shown in Fig. 1.7 [102].

Matrix effects can be divided into two kinds, physical and chemical [4]. Physical matrix effects depend on the physical properties of the sample and generally relate to the ablation step of LIBS, while chemical matrix effects occur when the presence of one element affects the emission characteristics of another element. In Ref. 103, matrix effects are

divided in two broad categories, namely those associated with the entry of the material into the plasma and those taking place in the plasma. The former process is the major topic of study in the laser ablation literature while the last one resides more in the field of plasma modeling and diagnostics.

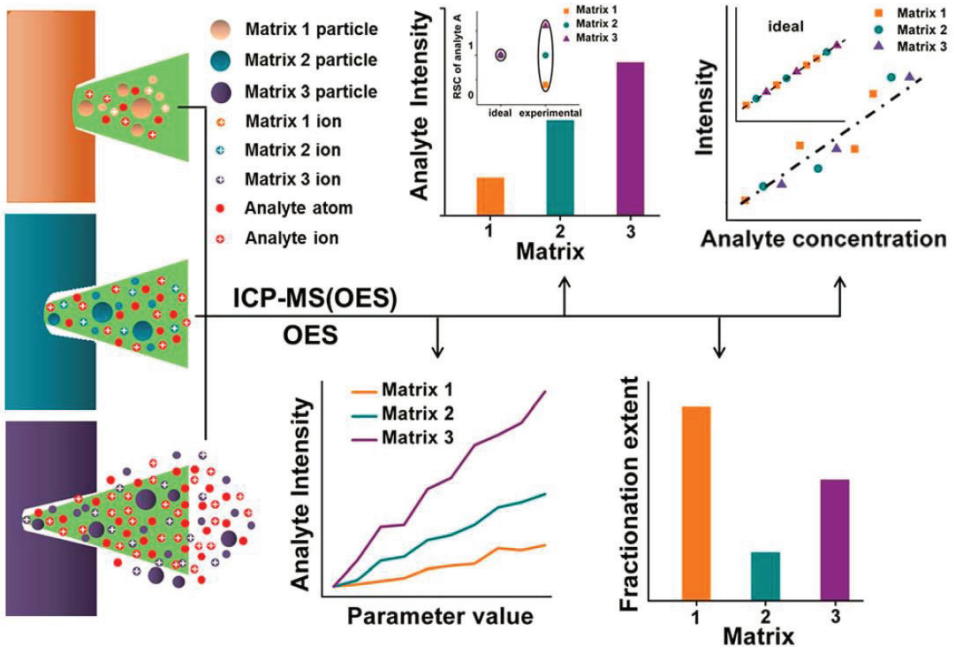

Figure 1.7 Simplified depiction of matrix effects in laser sampling based spectrometry. Note that all three different matrices are assumed to have the same concentration of the element, and all the matrices are ablated under the same laser conditions [102].

The most direct way is to evaluate the matrix effects is to compare the signals of a specific element from different matrices, which have the same concentration of the element, as shown in Fig. 1.7. A similar way is to measure the difference of calibration curve slopes of an element made from different series of matrices [102]. On the other hand, matrix effects can also be represented by the plasma characterization methods based on emission spectroscopy, since the existence of matrix effects will naturally lead to a variation of the plasma parameters like the electron density and temperature [104].

In order to increase the quantitative ability of LIBS, extensive studies have been done to reduce the influence of matrix effects. In Ref. 105, strategies for reducing matrix effects are collected in three groups: (i) matrix matching; (ii) internal calibration (e.g., standard

addition and isotope dilution); and (iii) correction of the effect either by directly measuring the effect or some property of the matrix and establishing a correction function or possibly joint analyte/interferent calibration. Some models have also been developed to compensate for matrix effects by parameterizing the plasma state, including the so-called calibration-free LIBS (CF-LIBS) [84]. This is a method of standardless analysis, and its basic idea is to compensate for the matrix effect by applying the basic equations derived from the LTE assumption to the spectral data in order to make each single measurement self-consistent and avoid the need for any comparison with calibration curves or reference samples.

Normalization approaches

Internal reference normalization is a well-known and frequently used method to minimize matrix effects and obtain accurate results. It can correct for the difference of ablation mass of various matrices and rectify the pulse-to-pulse signal instability [102]. As mentioned above, matrix effects can be related to the entry of the material into the plasma and to the fluctuation of plasma parameters. It is therefore understandable that the three most important normalization parameters for the intensity of a given spectral transition are the ablated mass, the plasma temperature, and the electron number density. However, the most general approach to normalization remains that of ratioing the intensity of the spectral line of the analyte to that of a suitable element present in the sample [101].

In Ref. 106, Barnett et al. have pointed out the criteria for the selection of the internal reference element and the internal reference line. These criteria state that the analyte and the internal reference should have: (i) similar volatilization rates; (ii) comparable ionization energies; and (iii) similar atomic weights. The spectral lines chosen for the ratio should: (i) have the same excitation energies; (ii) be free from self-absorption; and (iii) have similar intensity. Two kinds of internal reference elements can be used [42]: in some samples, matrix elements that are already present in a known and fixed amount can be used; in other types of samples (e.g. powders or liquids), an internal reference element can be added in a known and fixed amount. In this case, the element should be one that is not already present in the samples (or present in negligible amounts).

Besides normalization with an emission line, many other normalization approaches have been performed in order to achieve better quantification results, such as the use of the acoustic signals resulting from the ablation process, the temperature, the electron number density, the continuum background, the electrical current, the total plasma emission, and the surface density of the material [101]. A review of several different normalization approaches used in laser sampling-based spectrometry can be found in Ref. 107. Both single-variate and multi-variate corrections are discussed in this review in order to improve the analytical figures-of-merit.

We mention that the matrix effects as well as normalization approaches are much concerned in this thesis. In the following chapters, we will assess the matrix effects on the quantitative analysis of powders (Chapter 3) and on the classification of wines (Chapter 4), with surface-assisted LIBS. We will also discuss the effects of spectrum normalization with an internal reference element and the choice of reference lines for the spectrum normalization.

1.4 Resume

In this chapter, we have provided an overview of the theoretical background of LIBS as an analytical technique. After a general description of the laser-induced plasma, the physical processes of the plasma generation and evolution are described, with special attentions on the mechanisms of laser ablation and post-ablation interaction between the plasma and the laser pulse. Then, we presented the methods of plasma characterization with the optical emission spectroscopy. The methods used for the determination of plasma parameters are based on the assumption of a plasma in LTE and optically thin. The Stark broadening and Stark shift methods for the measurement of electron density, and the Boltzmann and Saha-Boltzmann methods for the measurement of temperature, are presented in detail. Finally, we focused on the quantitative analysis aspects of LIBS. The concepts of calibration and the figures-of-merit in quantitative analysis have been described. The matrix effects as well as normalization approaches, which are of critical importance in LIBS analysis, were also discussed in the end of this chapter.

Chapter 2. Characteristics of the ablation plume induced on glasses with laser-induced breakdown spectroscopy

As mentioned in the previous chapter, laser-induced plasmas can be distinguished from other plasmas (discharge, inductively coupled plasma…) by its violent expansion into the ambient gas. The description of the mechanisms involved in the plasma evolution and the consequent emission characteristics represents one of the key points for the analytical LIBS technique [63]. In previous works of our group, the influences of different experimental conditions (laser wavelength, fluence and ambient gas) on the plasma properties have been systematically investigated, with a metal (aluminum) as the target [53-56,58]. However, we can expect quite different properties for plasmas induced on dielectric materials compared to metal targets.

To complete our systematic studies on the evolution of laser-induced plasma, this chapter intends to characterize the plasma induced on the surface of a dielectric material, glass for instance, as a function of the ablation laser wavelength, infrared (IR) or ultraviolet (UV), and the ambient gas, air or argon. The surface damage of the samples will be discussed for ablation with IR or UV laser pulse when the sample is a float glass or a frosted one. Optimized ablation fluence will then be determined. Concerning the investigation methods, the morphology of the plasma will be presented with time-resolved spectroscopic imaging, while the profiles of the emission lines, electron density and temperature will be analyzed with time- and space-resolved emission spectroscopy. The analytical performance of the plasmas will then be studied in terms of the signal-to-noise ratio for several emission lines from some minor elements, Al, Fe, contained in glass, and in terms of the behavior of self-absorption for another minor element, Ca, in different ablation conditions.

2.1 Motivation

During the last ten years, it has been demonstrated that LIBS is an efficient tool for elemental analysis in transparent or translucent dielectric materials, glasses or crystals, for applications required in many fields such as archeological research [23-25], forensic investigation [26-28], nuclear waste storage [108-110], or gemstone identification and qualification [111-113]. In the fundamental point of view, laser ablation of transparent or translucent dielectric materials corresponds to specific processes, which are different from laser ablation of metals. The ablation plumes induced on the surface the two types of materials (metal or dielectric materials) are expected to have quite different properties leading, obviously, to specific considerations when optimizing experimental conditions for LIBS analyses. Up to now, even though extensive studies have been devoted to the characterization of plasma induced on metallic samples [52-58,114-117], the investigation of the plasma induced on the surface of dielectric materials remains rare. A lot of efforts have been focused on the influence of the ablation wavelength on the analytical performance of the induced plasma [118,119]. Especially, it has been demonstrated that the 4th harmonics Nd:YAG laser at 266 nm results in a more stoichiometric ablation than the 1064 nm radiation [119]. Some studies took into account the spatial and temporal evolution of the plasma [120,121]. In the practical point of view, one can still remark a large dispersion in the used experimental conditions for LIBS analyses of dielectric materials in terms of the laser parameters, such as wavelength (1064, 532, 355, or 266 nm from a Nd:YAG laser) and fluence, as well as the ambient gas, air or noble gas such as argon.

In this chapter, we will provide an extensive characterization of the plasma induced on glasses in terms of the morphology of the plasma, the profiles of the electron density and temperature and the emission properties of minor or trace elements contained in the sample, properties that are directly interesting for LIBS analytical purposes. Such a characterization has been carried out with two different ablation laser wavelengths of 1064 nm and 266 nm and in different ambient gases of air and argon in the atmospheric pressure. The resulting information provides arguments for the choice of the

experimental parameters in a given application. It supports also the plasma model used for the implementation of the calibration-free LIBS procedure for elemental determination in glasses [122]. The analytical performance is then studied in terms of signal-to-noise ratio, and self-absorption behavior of the plasmas induced in the different conditions. Another purpose of this chapter is also to correlate the damage left on the sample surface after a LIBS analysis to the used laser wavelength for different surface qualities of glass (float or frosted). This aspect is very important for some specific applications such as historical glass analysis [23] or gemstone qualification [113], since the induced surface damages have to be restricted into a minimal amount.

2.2 Experimental setup and measurement protocol

2.2.1 Experimental setup and protocol for plasma generation

The experimental setup for plasma generation and emission detection is shown in Fig. 2.1. Two Q-switched Nd:YAG lasers were used for ablation with IR (1064 nm) or UV (266 nm) radiation, a repetition rate of 10 Hz and a pulse duration of 5 ns. The laser beams passed through an ensemble of a half-wave plate (HWP) and a Glan prism (GP). This ensemble allowed a fine adjustment of the laser energy delivered to the target. A mechanical beam shutter (BSH) was used to control the delivery of bursts of pulses to the target. A beam splitter (BS) sampled each delivered pulse by sending 4% of it to a photodiode (PD), which, in turn, generated a synchronization signal to trigger the detection system. The laser beam was focused slightly under the sample surface by a quartz lens (f1 = 50 mm), with a shift of 2.0 mm for IR pulses and 0.5 mm for UV pulses. The laser spots on the target surface were measured to be 500 μm and 150 μm in diameter for IR and UV pulses, respectively.

During a measurement, the target was moved by using a motorized three direction (XYZ) translation stage to provide a fresh surface to each burst of laser pulses. The lens-to-sample distance was kept constant during the experiment using a trigonometric surface positioning system. This system was based on a combination of a laser pointer focused obliquely on the sample surface and a monitoring camera (C) used to image the laser spot

on the sample surface. The position of the laser spot on the CCD image was a direct monitoring of the lens-to-target distance. A flow of argon gas was delivered by a pair of tubes installed above the target and surrounding the laser impact zone, with a fixed rate of 5 l/min. Such flow ensured the expansion of the plasma into a pure argon environment at one atmosphere pressure. The argon gas was removed in the case of the ablation in ambient air. It is noticeable that the ablation took place in an open environment.

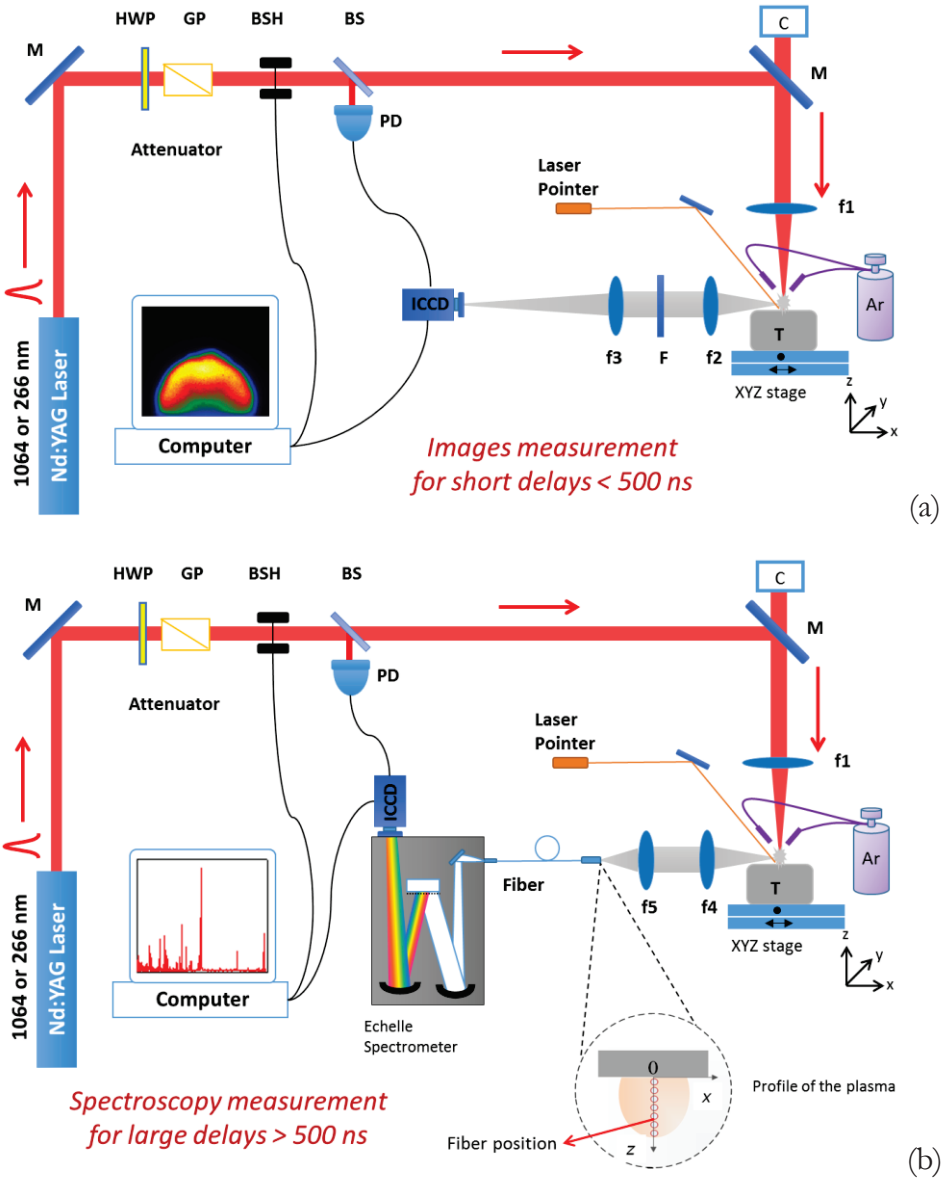

Figure 2.1 Experimental setup for plasma generation and emission detection: (a) spectroscopic imaging system was used at short delays below 500 ns; (b) time- and space-resolved spectroscopic detection system was used at long delays above 500 ns. M: mirror, HWP: half wave plate, GP: Glan prism, BSH: beam shutter, BS: beam splitter, PD: photodiode, C: camera, F: filter, T: target.

2.2.2 Dual-wavelength differential spectroscopic imaging

Experimental setup for images measurement

A spectroscopic imaging system [shown in Fig. 2.1(a)] was used to monitor the plasma morphology along a perpendicular axis with respect to the ablation laser beam. The associated collimation optical arrangement consisted of two achromatic doublet lenses in BK7 with focal lengths respectively of 60mm (f2) and 200mm (f3). The formed image was directly projected to an ICCD camera (iStar from Andor Technology) placed at the image plane. In our experiment, monochromatic images were recorded for the emission from the species to be studied in the plasma. Such spectroscopic imaging was realized with the help of narrowband filters (F).

Principle and protocol of dual-wavelength differential spectroscopic imaging

The procedure of spectroscopic imaging corresponds to dual-wavelength differential spectroscopic imaging technique [123]. A pair of narrowband filters is used in the experiment, as shown in Fig. 2.1(a). The center of one of these filters is centered at an emission line of a species, elemental or molecular, to be studied in the plasma (on-filter), while that of another one is shifted to a neighboring wavelength (off-filter) where emission from the specie is negligible. Wavelength shift between the two filters should remain small enough to avoid any change in the continuum emission and background passing through them. The experimental conditions (laser energy, surface position…) should be stable during the period where the double images are recorded, to ensure the representability of the images recorded with on-filter (for the specie signal) and with off-filter (for the background).

In addition, the transmission curves of the filters are measured with a calibrated white light source in such way that the subtraction between the two images can be correctly processed. An illustration is given in Fig. 2.2 with the spectrum of Al II 358.6 nm line [51]. The raw spectrum (green curve) was the result of superposition of the continuum and the Al emission line. The images recorded with the two filters (on-filter: blue curve, off-filter: red curve) were first corrected by the transmission curves of the filters. The

image with off-filter was then subtracted from the image with the on-filter. After subtracting, the resulting image was obtained which corresponding to the image of the emission line. It is noticed that with respect to the classical spectroscopic imaging, the subtraction of the continuum emission in this technique allows the plasma diagnostics starting from very short delays below tens of ns [123].

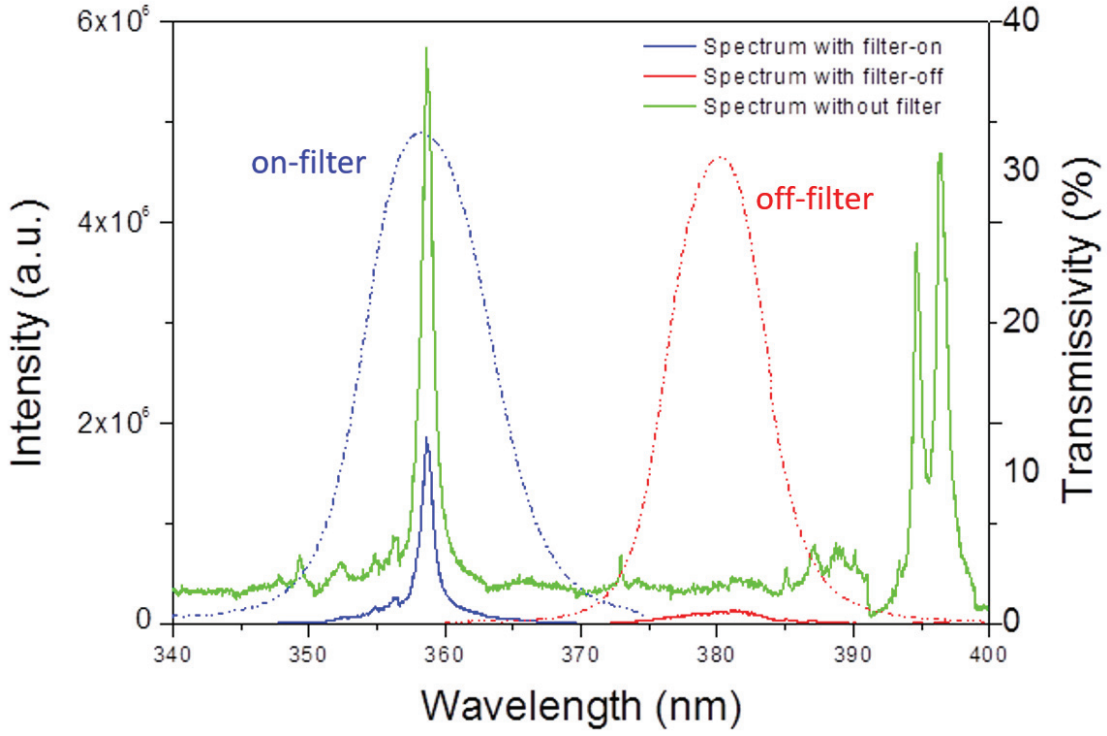

Figure 2.2 LIBS spectra around 370 nm including the Al II 358.6 nm line, without filter, with an on-filter and with an off-filter [51].

After the above-discussed subtraction, the Abel inversion [124,125] was applied to the resulting image in order to obtain the two-dimensional distribution of the corresponding emitters inside the plume. Abel inversion is a commonly used numerical method for the spatial diagnostics of rotationally symmetric plasmas. It was needed here because the image recorded by ICCD camera was spatially integrated along the line-of-sight defined by the imaging optics. However, before Abel inversion, the images were also processed with a Gaussian smoothing and a symmetrization [123]. Finally, the Abel inversion was performed using the Nestor-Olsen method [126]. An illustration is given in Fig. 2.3 to show the results of the images after background subtraction and after Abel inversion [51]. The inverted images for several species in a plasma could be presented in the same picture

by associating a specific color to each species, and the multi-species image can thus be obtained. We mention that the inverted emissivity images represent only the spatial distribution of the corresponding excited emitters, i.e. the population of the associated species in the upper level of the transition. Using emissivity images to determine the spatial density distribution of the species implies to take into account the corrections due to temperature gradients in the plasma (assuming LTE). In this work, we restrain the use of emissivity images to qualitative interpretations of the morphology and the internal structure of the plasma.

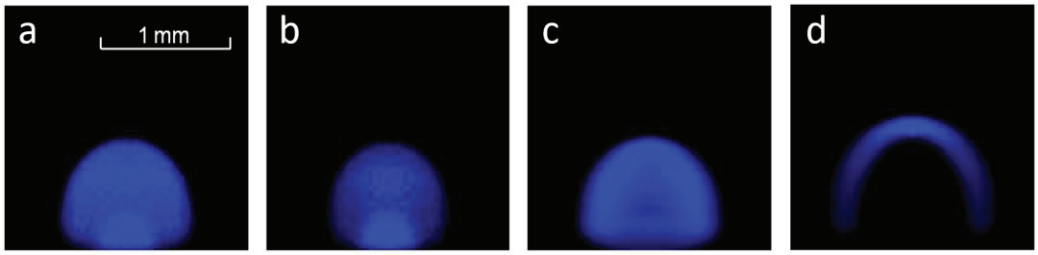

Figure 2.3 Illustration of the background-subtracted image and Abel-inverted image with the emission from Ar I line. a) The image recorded with the on-filter, b) the image recorded with the off-filter, c) the differential image, d) the differential image after Abel inversion [51].

2.2.3 Time- and space-resolved emission spectroscopy

An arrangement of time- and space-resolved spectroscopic detection system [shown in Fig 2.1(b)] was also available in the experiment. An optical system with two fused silica lenses, with a first lens of focal length of 75 mm (f4) and a second lens of focal length of 50 mm (f5), collected the plasma emission along an axis perpendicular to the ablation laser beam. Typical size of the image of the plasma formed by this optical collection system was about 1.5 mm. An optical fiber of 50 μm diameter placed in the image plane of the two-lens system captured a part of the emission from the plasma. By moving the fiber in the image plane, profile of the plasma along the laser propagation direction could be performed with a space resolution of 75 μm. The output of the fiber was connected to the entrance of an echelle spectrometer, which was in turn connected to a second ICCD camera (Mechelle and iStar from Andor Technology). The used spectrometer offered a spectral range from 220 to 850 nm with a resolving power of $\lambda/\Delta\lambda=5000$. The

recorded spectra were used for plasma diagnostics: the electron density was extracted using the Stark broadening of an emission line, while the electron temperature was calculated by performing the Saha–Boltzmann plot (assuming LTE). The principle of the plasma diagnostic methods can be found in Section 1.2.

It is noteworthy that, at short delay times, the continuum emission from the plasma was very strong. Consequently, the diagnostics with emission spectroscopy became efficient only from a delay of about 500 ns. This is the reason why the time- and space-resolved emission spectroscopy and the imaging technique were used in a complementary way to cover different time intervals of the evolution of the plasma from several ns to several μs.

2.2.4 Glass samples used in the experiments

Fig. 2.4 shows the microscope slides used as samples for the present study. They are convenient, cheap and commercially available. All these glass slides belonged to the same series so that it is ensured that their physical and chemical properties were identical. The slides presented two surface qualities, one part (~1/4) of a slide showing a frosted surface, while the rest of the slide was left with the original floating glass surface. They are often quite pure with a matrix of SiO_2 and some minor elements such as Ca, Al, and Fe. They can be directly ablated after some basic cleaning with in sequence, tap water, distilled water and alcohol.

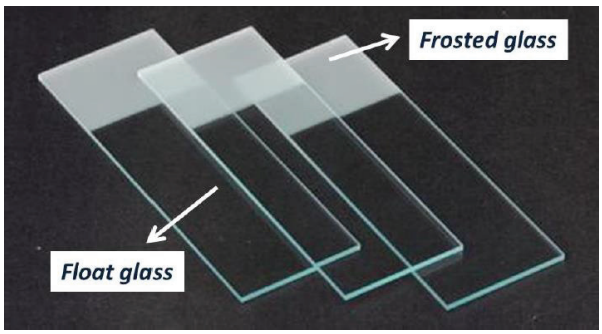

Figure 2.4 Microscope slides used as glass samples in the experiment.

2.2.5 Protocol of image or spectrum taking

Each image or spectrum was recorded with an accumulation over 200 laser shots

distributed in 20 craters, each of them being ablated by 10 consequent laser pulses. The synchronization of the whole setup was ensured by a computer with a homemade software.

2.3 Determination of the experimental conditions

2.3.1 Effect of the surface quality

Surface damage induced by laser ablation was first observed on float and frosted glasses. The results are shown in Fig. 2.5 with macro-mode photographs of the glass surfaces ablated with IR or UV laser pulses in air (the same scale is used for all the photos). Each crater on the sample surface was caused by the ablations of 10 consequent laser pulses. We can see in Fig. 2.5(a) that a large damage zone appears around a laser impact on a float glass surface following ablation with IR pulse. Cracks are visible on the photo, indicating surface damage by mechanical/thermal waves. A contrasting feature can be seen with UV pulse ablation: craters with regular contour appear with a size compatible with the laser beam spot on the glass surface [Fig. 2.5(b)]. On the rough surface of a frosted glass, situation changed in the sense that both IR and UV laser pulses leave rather regular craters on the surface, no visible crack is observed [Fig. 2.5(c) and (d)]. We can remark however that the size of the craters is significantly larger than the spot of the laser beam on the sample surface. This implies certainly damage by mechanic/thermal waves, but, for the rough surface of a frosted glass, such damages remain small enough for the glass surface to keep its mechanical stability. The above tests demonstrate therefore that in order to restrict the damage on a float glass within an acceptable extent, only the UV ablation laser can be used. On a rough surface of a frosted glass however, both IR and UV ablations allow limited surface damages. This observation can have a practical importance even though the underlying physical mechanisms still need some clarifications.

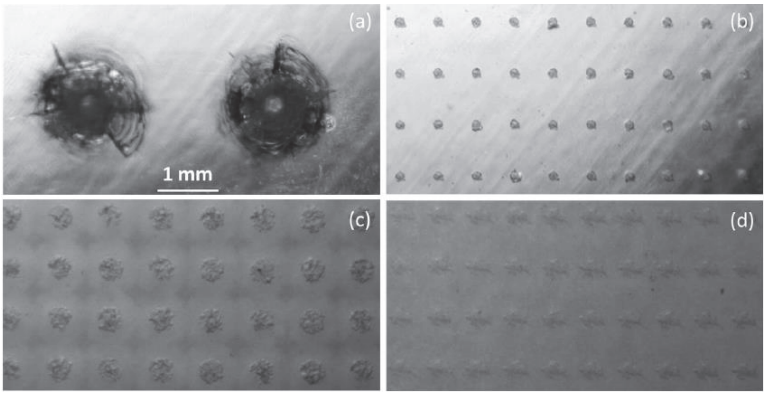

Figure 2.5 Macro-mode photographs of glass surface after laser ablation in atmospheric air with (a) float glass ablated by 1064 nm pulse, (b) float glass ablated by 266 nm pulse, (c) frosted glass ablated by 1064 nm pulse, and (d) frosted glass ablated by 266 nm pulse. A same magnification was used for all the photographs. The scale in Fig. 2.5(a) applies therefore to all the pictures in this figure. Each crater on the sample surface was resulting from 10 consequent laser pulses.

In order now to compare LIBS signals with plasmas induced in the same ablation conditions on a float glass and a frosted glass, we show in Fig. 2.6 the decay of the intensity of the Ca II 315.8 nm line emitted from the plasmas induced by UV laser pulses on these two types of glass placed in air or argon ambient gas. The intensity was recorded with the collection fiber placed in the middle of the plasma. The results clearly show similar emission properties of the plasmas induced by UV pulse on float or frosted glass and such behavior is observed for ablations in air as well as in argon ambient gas. This means that for a systematic study of the properties of the plasmas induced by IR or UV laser pulse on a glass sample, an only choice is frosted glass, because it offers the possibility for both IR and UV lasers to perform regular craters with a bust of pulses. Moreover, this test demonstrates that the results obtained with UV laser ablation of a frosted glass would be representative for a float glass. Therefore, only frosted glass was used for the following studies.

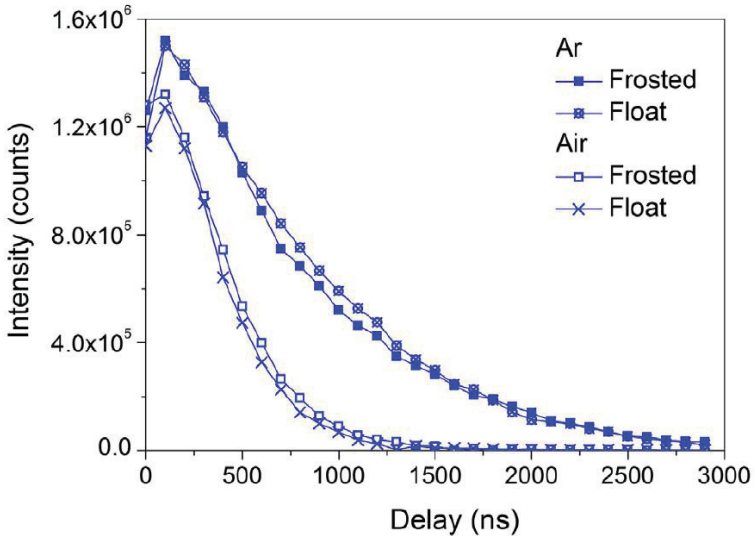

Figure 2.6 Decay of the intensity of the Ca II 315.8 nm line emitted from plasmas induced by UV laser pulses on a float or a frosted glass placed in air or argon ambient gas.

2.3.2 Determination of the laser fluence

The laser fluence for an optimized operation of LIBS measurement was then determined. Here, the criterion was taken as an optimized emission intensity of a minor element, Ca for instance, from the induced plasma. The measurement was carried out with the IR laser because it is easy to change the laser energy with the attenuator for IR laser. The spectra were recorded at a delay of 0.5 µs with a detection gate width of 2 µs and with the fiber positioned in the middle of the plasma for air as well as argon ambient. Fig. 2.7 shows the intensity of the Ca I 649.3 nm line as a function of the pulse energy of the IR laser when the ablation took place in air and argon. We can see that the breakdown threshold is situated around 30 mJ for ablation in argon and around 40 mJ for ablation in air. Beyond the threshold, the emission intensity increases with pulse energy. For ablation in argon above 70mJ, the intensity becomes saturated. No clear saturation is observed for air. Therefore, it is reasonable to work with a pulse energy of 85 mJ for IR ablation. For a focused laser spot of 500 µm on the sample surface, it corresponds to a fluence of 43.3 J/cm^2. For the UV laser, focused on the sample surface on a spot of 150 µm in diameter, a pulse energy of 8 mJ was fixed for the experiment, resulting in a similar fluence of 45.3 J/cm^2.

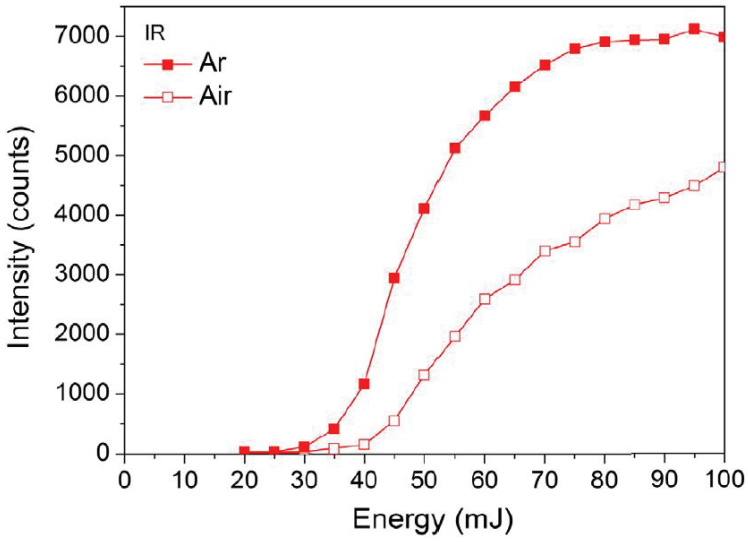

Figure 2.7 Intensity of the Ca I 649.3 nm line as a function of the pulse energy of the IR laser for ablations in air and argon ambient gases.

2.4 Characteristics of the plasmas in different ablation conditions

With the experimental conditions fixed in the above tests, i.e. ablation of frosted glass with both IR laser, at a fluence of 43.3 J/cm^2, and UV laser, at a similar fluence of 45.3 J/cm^2, we have then studied the temporal and spatial characteristics of the generated plasmas in air and in argon. In this section, we present the obtained results about the morphologies of the plasma, the axial profiles of the emission line, and the profiles of electron density and temperature. The focus of our presentation will be the comparison between the different ablation conditions of laser wavelength and ambient gas.

2.4.1 Morphology of the plasma and its evolution with differential imaging

For ablation in air, we have chosen calcium and nitrogen in their neutral and first-ionization forms, to represent the shocked gas and the vapor from the target, respectively. For ablation in argon, the corresponding chosen elements are calcium for the vapor and argon for the shocked gas. Table 2-1 shows the emission lines selected for these species and the corresponding pairs of filters for differential spectroscopic imaging. As mentioned above, for each representative species, emission images were taken with the on- and off-filters. The differential emission image between the on and the off images

was then processed with the Abel inversion, which led to emissivity image of the species. Note that different detection windows of ICCD were used here for different ablation conditions, as shown in Table 2-2, in order to avoid the saturation of ICCD camera and guarantee the high quality image signals simultaneously.

Table 2-1 Elements chosen to represent the ablation vapor and the shocked gas in a plasma, emission lines selected for the species associated with the chosen elements and the characteristics of the corresponding on- and off-filters for the spectroscopic images of the species.

Plasma component	Element	Species emission line	Central wavelength (nm) [a]	
			On-filter	Off-filter (in air/in Ar)
Vapor	Ca	Ca I 422 .7 nm	420	488/530
		Ca II 396.8 nm	400	488/530
Shocked gas	N	N I 746.8 nm	750	760
		N II 500.5 nm	500	488
	Ar	Ar I 750.4 nm	750	720
		Ar II 488.9 nm	488	530

[a] The bandwidth is 10 nm for all the used filters.

Table 2-2 Detection windows of ICCD for plasma imaging under different ablation conditions

Delay (ns)	IR (in Air and in Ar)		UV (in Air and in Ar)	
	Gate (ns) [a]	Gain	Gate (ns)	Gain
0	5	50	4	100
120	5	50	4	100
210	5	50	30	100
300	50 (25)	50	80	100
500	50 (25)	50	80	100

[a] (25) ns gate width was used with the filters of 720, 750 and 760 nm.

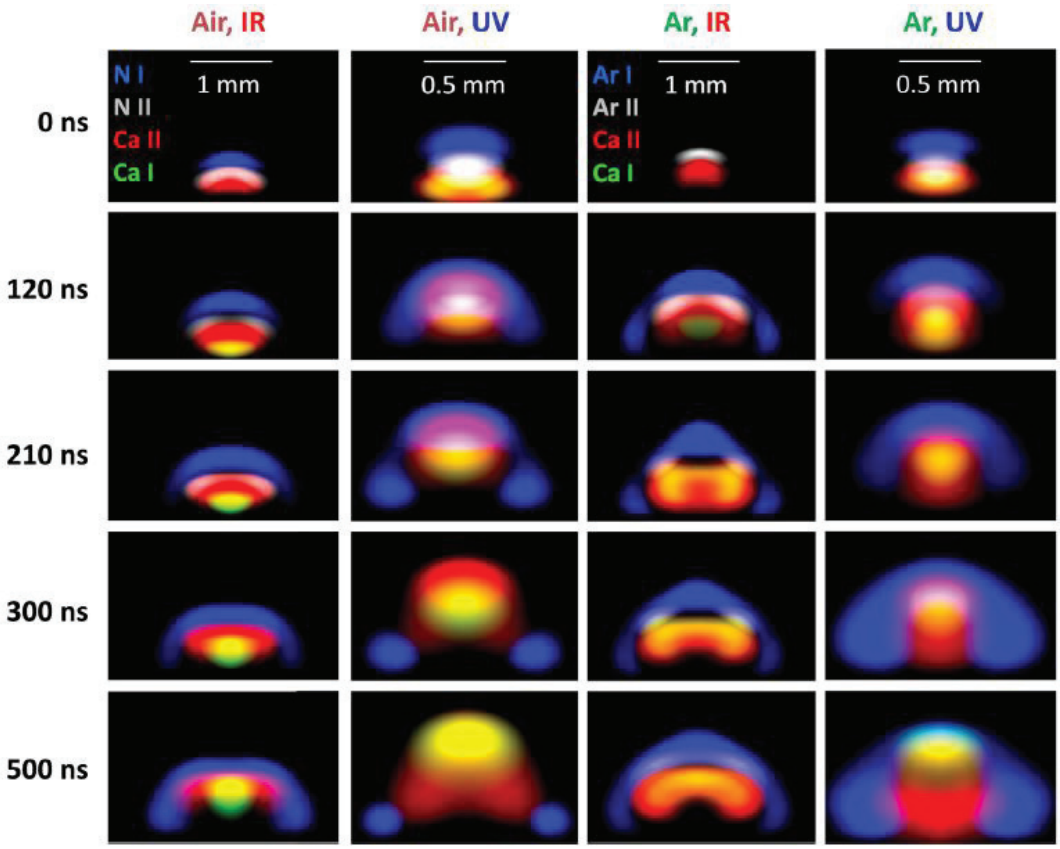

Figure 2.8 Composite emissivity images of the plasmas obtained by IR ablation in air (1st column from the left), UV ablation in air (2nd column), IR ablation in argon (3rd column) and UV ablation in argon (4th column). The detection delays for these images are indicated against the left side of the figure. The bottom line of each image corresponds to the target surface. Remark the two different scales used for IR and UV ablations.

Figure 2.8 shows the composite emissivity images where the emissivity images of the representative species in the plasma are superimposed on a same picture. The correspondence between the 4 used colors and the represented species in the plasma is indicated in Fig. 2.8 on the images corresponding to 0 ns delay. Some intermediary colors appear when mixtures of the initial colors occur. For example, a mixture of red (Ca II) and green (Ca I) results in yellow, while a mixture of red (Ca II) and gray (N II or Ar II) results in pink. The images are presented as a function of the detection delay and for the four ablation configurations corresponding to the combinations of two ablation laser wavelengths and two ambient gases. We remark the different scales used for the presentation of the images corresponding to IR and UV ablations because of the smaller sizes of the UV induced plasmas. The bottom of the pictures corresponds to the sample

surface.

In Fig. 2.8, we can see that in all the studied ablation conditions, the plasma exhibits a rather hemispherical form and a layered structure, especially at very short delays below 200 ns. If we go through the plasma along its symmetric axis by following the propagation direction of the ablation laser pulse, we can in general meet first a thin layer of excited neutral ambient gas, indicated by an emission zone of N I or Ar I for the cases of ablation in air or in argon respectively. Under this layer, a layer of ionized gas N^+ or Ar^+, can be observed with an emission zone of N II or Ar II respectively. For the case of ablation in argon with IR laser at very short delay, the layer of excited neutral gas is absent; instead, a layer of ionized argon is present in the front of the plasma in direct contact with the unexcited ambient gas. This suggests a complete ionization of the layer of shocked gas at very short delays. The excited neutral argon layer appears for a longer delay of 120 ns when the plasma cools down and expands. Under the layer of ionized gas, a partially ionized calcium vapor can be found. In such vapor, in general, a layer of Ca^+ indicated by the emission of Ca II, is first observed, followed by a population of neutral calcium indicated by the emission of Ca I. For long delays, mixtures between the different layers of species can occur due to the hydrodynamic motions of the species within the plume.

As shown in Ref. [54,56], the propagation behavior of the plasma at short delays is directly linked to the post-ablation interaction regime. The similar general aspect of the plasma observed at short delays in the four different ablation conditions thus suggests that a same post-ablation interaction regime can characterize the plasmas generated in all the four ablation configurations. This interaction regime can be clearly identified as the laser-supported combustion wave (LSC) [68], because the plasma plume has a hemispherical form and a layered structure, as discussed in detail in Section 1.1.3. This observation contrasts with the ablation of a metallic target with IR or UV laser pulse, where while UV ablation leads to LSC, IR ablation induces laser-supported detonation (LSD) wave which results in a very different structure of the plasma at short delays [54,56]. Even though a detailed interpretation of the observed results does not correspond to the main purpose of the present work, it is not surprising to find different behaviors between

ablation of metals and that of dielectric materials such as glass. The absorption and the relaxation properties, as well as the thermal and mechanical properties are indeed very different between metals and glasses.

Now, let us look at the differences that exist between ablations of glass for the two laser wavelengths (IR or UV). An obvious difference in Fig. 2.8 is that the lateral size of the plasma induced by UV pulse is clearly smaller than that by IR pulse. This is simply related to the difference in the size of the focused laser spots on the sample surface. Another difference between IR and UV ablations can be observed in Fig. 2.8 concerning the lifetime of the ionized ambient gas. For IR laser ablation, this lifetime is always, in air as in argon, longer than that for UV laser ablation. In the last case, ionized gas disappears for delays beyond 210 ns. This can be due to the fact that in the ablation plasma, the inverse bremsstrahlung is the dominant absorption mechanism, which leads to a dependence of the absorption cross section in λ^3 at high temperature and in λ^2 at lower temperature, where λ stands for the ablation laser wavelength [63]. As discussed in Ref. [54], in the LSC regime, the shocked gas remains transparent for laser radiation, the tailing part of the laser pulse transmits through the layer of shocked gas and is absorbed by the ablation vapor. The higher absorption rate of IR laser radiation results in a higher temperature in IR ablation vapor than that in UV ablation vapor. In the LSC interaction regime, the layer of the shocked gas that is in direct contact with the vapor can be ionized by the UV part of the continuum emitted from the heated ablation vapor. This is the reason why longer lifetimes of the population of the ionized shocked gas was observed for IR laser ablation, since in this case the vapor is heated into higher temperature. This will be discussed in detail later.

Let us compare now between different ambient gases. For IR ablation, the lifetime of the ionized gas layer in argon is longer than in air, suggesting a higher ionization degree of the shocked gas in argon. This assumption is supported by the observation of the complete ionization of the layer of shocked gas at very short delay for IR ablation in argon (as already discussed above). For UV ablation, the difference between air and argon ambient gases is less straightforward by looking only on the emissivity images.

2.4.2 Axial profiles of emission intensity

In the experiment, by recording the emission spectrum as a function of the position of the collection fiber along the symmetrical axis of the plasma, we got the axial emission profile of the plasma. As already mentioned above (Section 2.2.3), the diagnostics with emission spectroscopy become efficient for detection delays beyond 0.5 μs. This is complementary with the spectroscopic imaging technique for longer delays in the monitoring of the ablation plume. Three typical delays of 0.5 μs, 1.0 μs and 2.0 μs were studied for each ablation condition, and the corresponding gate widths are shown in Table 2-3. As after 0.5 μs, the emission intensity is globally decreasing with time, such that longer gate widths were needed for large delays to integrate spectra with high signal-to-noise ratios. For all the recorded spectra, the gain applied to the intensifier of the ICCD camera was kept constant (150) in order to avoid such gain corrections for comparing different line intensities. The spectra were then normalized to the corresponding gate width for the evaluation of the emission intensity.

Table 2-3 Detection windows of ICCD for spectrum collection under different ablation conditions

Delay (μs)	Gate width (ns)			
	IR-Air	IR-Ar	UV-Air	UV-Ar
0.5	80	60	200	80
1.0	100	80	500	120
2.0	150	100	1000	300

Fig. 2.9 shows the axial emission intensity profiles of Ca I and Ca II lines at different ablation conditions. The axial position in each figure represents the distance between the observation point in the plasma and the target surface (the origin of the axis being the target surface). In each figure, the line intensities of the IR plasmas are always higher than UV plasma; moreover, the line emission of IR plasma continues to propagate at longer delays, while the UV plasma is more static. For example, for the Ca I line in air [Fig. 2.9(a)], during 0.5 to 2 μs, the point of maximum intensity for the IR plasma moved from 0.6 to 1.6 mm with an average speed of 67 m/s, while the emission zone of UV plasma was

moved from 0.6 to 0.9 mm with a much smaller speed of 20 m/s. In addition, for the IR plasma, the Ca I line is closer to the target surface at the delay of 0.5 µs and it gradually mixes with the Ca II line at longer delays. This is in good agreement with the spectroscopic image results as observed in Fig. 2.8.

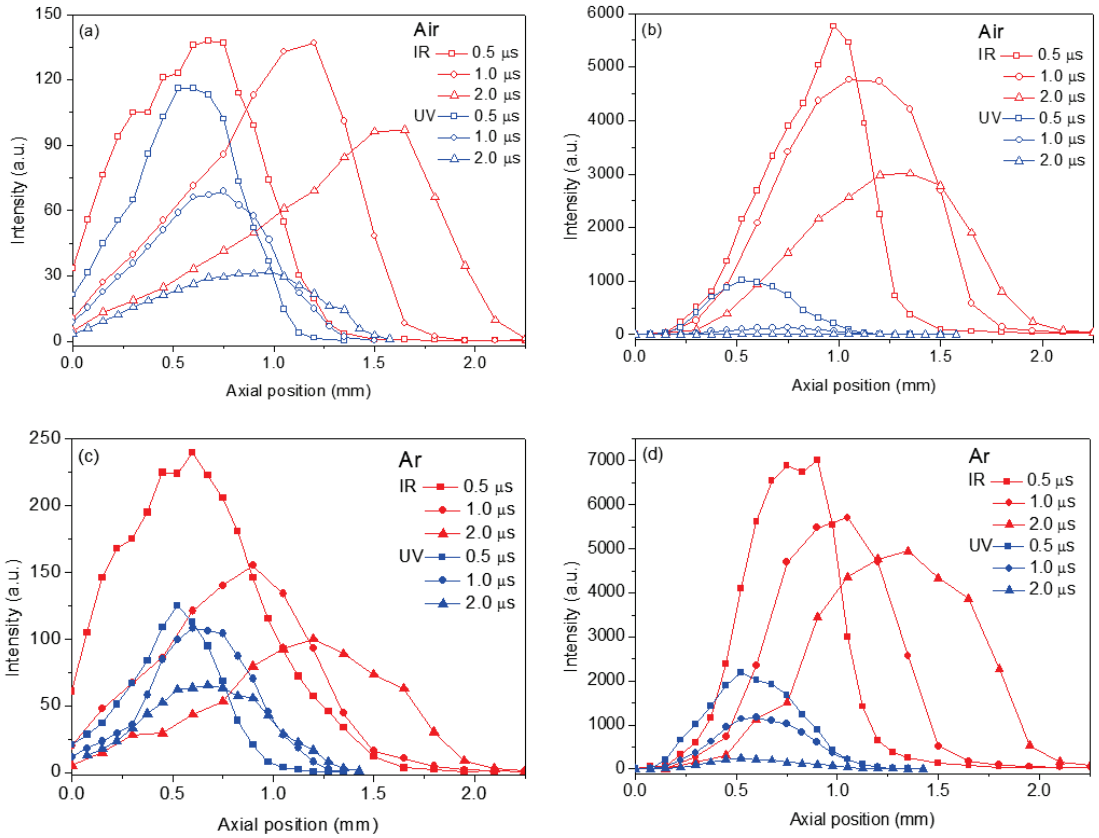

Figure 2.9 Axial emission intensity profiles of Ca line at the delays beyond 0.5 µs in different ablation conditions. (a) Ca I 646.3 nm line in air, (b) Ca II 315.9 nm line in air, (c) Ca I 646.3 nm line in Ar, (d) Ca II 315.9 nm line in Ar. The sample surface is situated at 0.0 mm.

When comparing the results for the two ambient gases, we observe that the emission intensity is always higher and with longer lifetime in argon gas than in air. By observing the propagation behaviors of the Ca lines, we can see that the plasma in air presents a slightly larger extent than that in argon. This can be attributed to the different hydrodynamic or thermodynamic properties of the two gases. For example, air is more compressible and with higher thermal conductivity than argon [127]. This means the plasma could be more confined in argon resulting in stronger emission lines. It is also worthy to mention that when the LSC wave is the dominant mechanism of post-ablation,

as it is the case of the present work, the optical nature of the ambient gas does not influence greatly the propagation behavior of the plasma. This is quite different from the case of LSD regime as reported in Ref. 58, where a significant difference can be observed for the expansion behavior of plasmas in air and in argon, due to the different ignition mechanisms of LSD wave involved in these two ambient gases.

2.4.3 Axial profiles of electron density and temperature

From the recorded spectra, we further extracted the axial profiles of electron density and electron temperature for the different ablation conditions studied in this experiment. In our data treatment, the electron density was extracted by the Stark broadening of the Si I 288.2 nm line. This is a strong non-resonant line and its Stark broadening parameter is known [83]. We used a value of 6.40×10^{-4} nm for a plasma temperature of 10^4 K from the Ref. 83. The relative uncertainty of the electron density determination was estimated to 10%, taking into account both the uncertainty of the Stark broadening parameter and the error in the fitting of the experimental data. An example of Si I 288.2 nm line with a Voigt fit used for estimating the electron density is shown in Fig. 2.10(a). In such fit the instrumentation broadening is taken into account with a Gaussian profile, the resulted FWHM of the corresponding Lorentz profile is used to calculate the electron density with Eq. (1-6).

The temperature was calculated using Saha-Boltzmann plots [See Fig. 2.10(b)] of the emission lines from Ca, including Ca I and Ca II lines (Ca II 315.9, 317.9, 370.6, 373.7 nm lines and Ca I 445.5, 643.9, 646.3, 649.4 nm lines). There was not any resonant line among the above ones, which reduces the error of temperature determination due to self-absorption. The relative uncertainty of the electron temperature determination was estimated to 10%. The needed spectroscopic data of the used Ca lines taken from the NIST database [128] are presented in Table 2-4.

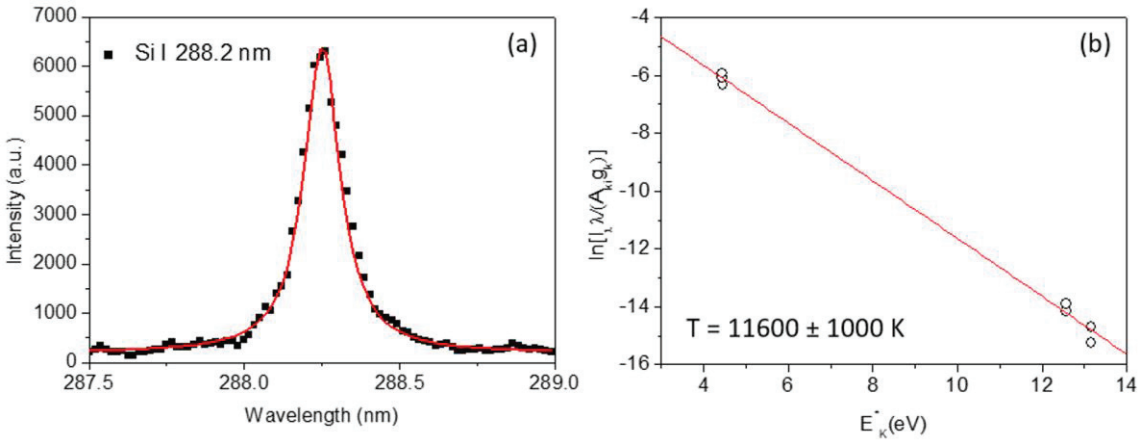

Figure 2.10 (a) An example of Si I 288.2 nm line used for estimating the electron density; (b) a typical Saha-Boltzmann plot of Ca lines used for estimating the plasma temperature.

Table 2-4 Spectroscopic data of Ca lines used for temperature calculation.

Species	λ (nm)	A_{ki} (s-1)	E_i (eV)	E_k (eV)	g_i	g_k
Ca II	315.887	3.1e+8	3.12	7.05	2	4
Ca II	317.933	3.6e+8	3.15	7.05	4	6
Ca II	370.603	8.8e+7	3.12	6.47	2	2
Ca II	373.690	1.7e+8	3.15	6.47	4	2
Ca I	445.589	2.0e+7	1.90	4.68	5	5
Ca I	643.907	5.3e+7	2.53	4.45	7	9
Ca I	646.257	4.7e+7	2.52	4.44	5	7
Ca I	649.378	4.4e+7	2.52	4.43	3	5

Fig. 2.11 shows the axial profiles of electron density for ablations in air [Fig. 2.11(a)] and in argon [Fig. 2.11(b)] for IR and UV lasers. We can see that for UV ablation and especially in air, the plume does not exhibit significant axial motion against the sample surface for delays beyond 0.5 μs. This motion is quite small in air. On the contrary, the IR ablation plume continues to propagate at longer delays. This corresponds well to the observations in Fig. 2.9 that the UV plasma is more static than IR plasma. Besides, we can remark that the electron density decreases with time for all the ablation conditions. Nevertheless, the electron density profiles are always higher for IR plume than for the UV plume, regardless of the choice of the ambient gas. When comparing the two ambient

gases, we can see that IR ablation in argon produces the highest electron density (0.5 μs), while UV ablation seems to be almost insensitive to the ambient gas from the point of view of the electron density. This confirms the fact that in image observation (Fig. 2.8), for UV ablation, similar morphologies are observed in air and in Ar ambient gases.

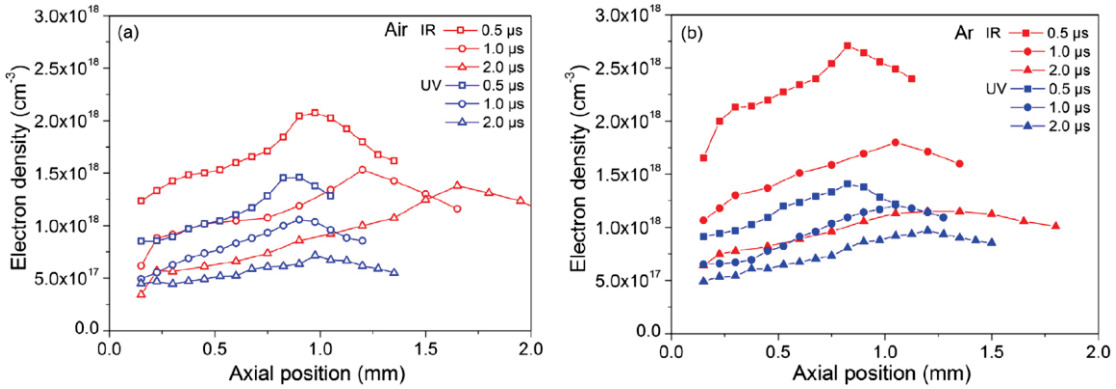

Figure 2.11 Axial profiles of the electron density of the plasmas induced in air (a) and in argon (b) with IR or UV laser at different delays beyond 0.5 μs. The sample surface is situated at 0.0 mm.

Fig. 2.12 shows axial profiles of electron temperature. Similar behaviors as the electron density profiles can be observed as functions of the laser wavelength and the ambient gas. The temperature profiles are quite static for UV ablation, while the IR profiles continue to propagate at long delays. The IR plume is always hotter and its temperature decrease is slower than that of the UV plume. When we compare between the two ambient gases, we can see that for IR ablation, similar temperatures are obtained in air as in argon. Thus, the higher electron density in argon observed in Fig. 2.11(b) does not correspond here to a higher temperature for IR ablation in argon. This behavior will be again discussed below when we observe the self-absorption phenomenon in the different ablation conditions. For UV ablation, however, the plasma temperature is found higher in argon than in air. This may be interpreted by the confinement effects of the argon gas with smaller compressibility and smaller thermal conductivity.

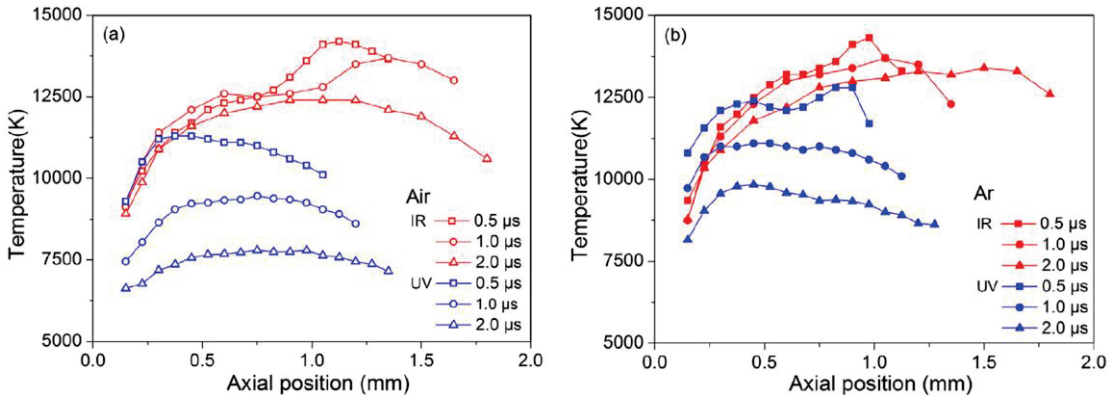

Figure 2.12 Axial profiles of the electron temperature of the plasmas induced in air (a) and in argon (b) with the IR or the UV lasers at different delays beyond 0.5 µs. The sample surface is situated at 0.0 mm.

2.5 Analytical performances in different ablation conditions

After dealing with the plasma characteristics in the different ablation conditions, we will focus in this section on the analytical performance of the plasmas induced in these conditions. Such performance is obviously related to the plasma characteristics discussed above, but it is often directly interesting for LIBS applications [101]. We will present a study on the signal-to-noise ratio and self-absorption behavior in the detection of minor elements in glass with the different ablation conditions.

2.5.1 Signal-to-noise ratio as a function of the detection delay

Fig. 2.13 shows signal-to-noise ratio as a function of the detection delay for an neutral line, Al I 309.3 nm line, and an ionic line, Fe II 259.9 nm line, belonging to 2 minor elements in glass, aluminum and iron. The measurement was taken for IR and UV ablations and with the collection fiber in the central part of the plasma, i.e. according to the morphologies of the plasmas induced with IR or UV ablation, at a height of 1.05 mm for IR ablation and 0.65 mm for UV ablation. The detection gate width used for the measurement varied for different delays with the following couples of gate/delay in ns: 20/50, 25/100, 30/150, 60/200, 80/500, 100/1000, 150/2000 and 350/4000. The recorded spectra were then normalized to a gate width of 100 ns for the evaluation of signal-to-noise ratio presented in Fig. 2.13. For ablation in air, we can see in Fig. 2.13(a) that for a given lines, Al I or Fe II, the UV ablation plasma reaches first the optimal delay

for the best signal-to-noise ratio at 200 ns, whereas the IR ablation plasma the optimal delay is obtained between 500 ns and 1000 ns. Nevertheless, the IR ablation plasma always leads to higher signal-to-noise ratio for both neutral and ion lines. For ablation in argon, as shown in Fig. 2.13(b), we can see the same behaviors as in air, with an optimal delay around 500 ns for UV ablation and a longer delay of 1000 ns for IR ablation. We can remark that the optimum ablation condition was obtained for the IR laser with argon ambient gas at 1000 ns delay time. The observed behaviors in terms of signal-to-noise ratio are consistent with the fact that in both ambient gases, the IR ablation induces plasmas with higher electron densities and temperatures than the UV ablation.

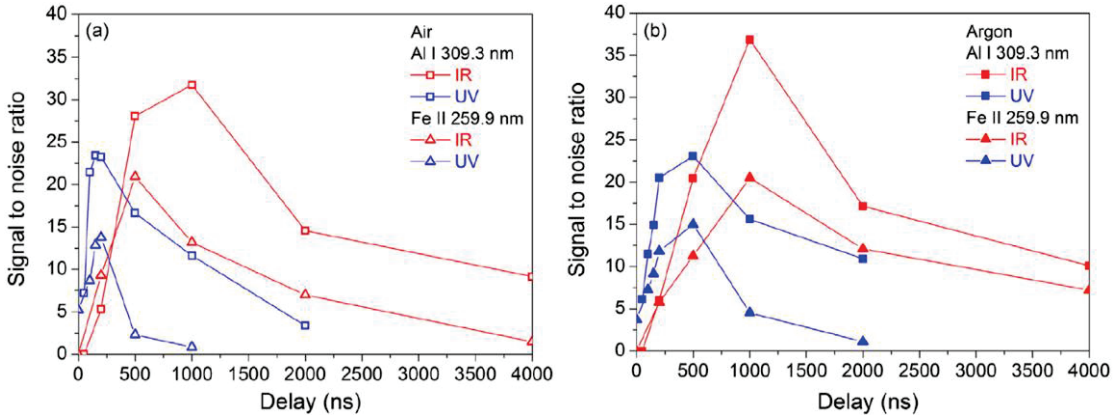

Figure 2.13 Signal-to-noise ratio as a function of the detection delay of two different lines, Al I 309.3 nm line and Fe II 259.9 nm line, measured in air (a) and in argon (b).

2.5.2 Self-absorption effect as a function of the axial detection position

The effects of self-absorption have been evaluated and compared between the different ablation configurations with a qualitative indicator: the intensity ratio of the two resonant Ca II lines at 393.4 nm and 396.8 nm. Since they belong to a doublet corresponding to two transitions sharing the same ground state, the self-absorption due to the population in the ground state would more affect the stronger one (393.4 nm line) and tend to equalize the experimental emission intensities of these two lines. It is why a large value of the intensity ratio, I_{393nm}/I_{396nm}, indicates a weak self-absorption [Fig. 2.14(a)], and a value close to unity indicates a heavy self-absorption [Fig. 2.14(b)]. In the experiment, we measured this ratio as a function of the axial position of the fiber, and for the delays that optimized respectively the signal-to-noise ratio for IR and UV plumes, i.e. 1.0 μs for IR

ablation and 0.5 µs for UV ablation. The obtained results are shown in Fig. 2.15.

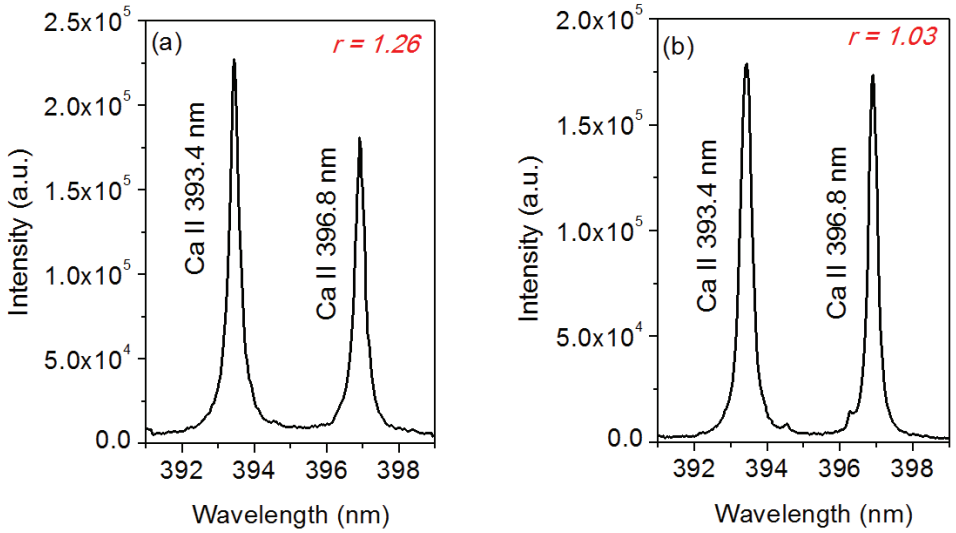

Figure 2.14 Evaluation of the self-absorption effect with the two resonant Ca II lines at 393.4 nm and 396.8 nm. A large value of the intensity ratio of 393.4 nm and 396.8 nm (r = 1.26) indicates a weak self-absorption (a), and a value close to unity (r = 1.03) indicates a heavy self-absorption (b).

We can see in Fig. 2.15(a) that in air, the plasmas with IR or UV ablation are severely affected by self-absorption. We specify that, in addition, the emission line of the UV plasma exhibited a clear self-reversal behavior, indicating a severe self-absorption in an inhomogeneous plasma [76]. The average values of the intensity ratio over the whole plasma are 1.11 for IR plasma and 1.08 for UV plasma. For the IR plasma, only a small volume between the axial distances of 250 µm and 500 µm shows less self-absorption. In argon [Fig. 2.15(b)], self-absorption appears less severe than in air for IR as well as UV plasma, especially around the top edge of the plasmas where the intensity ratio increases because of the decrease of the both density and geometrical thickness of the plasma. In addition, similarly to the case of ablation in air, a zone of weak self-absorption appears in the lower part of the IR plasma between 250 µm and 500 µm, as the consequence of the propagation of the IR plume away from the sample surface. The average values of the intensity ratio are 1.19 for IR plasmas and again 1.08 for UV plasmas. The severer self-absorption in air may affect the temperature evaluation by artificially increasing the temperature values [Fig. 2.12(a)]. It may explain the comparable temperatures that we observed for ablations in air and in argon (Fig. 2.12) despite lower electron densities

measured in air (Fig. 2.11).

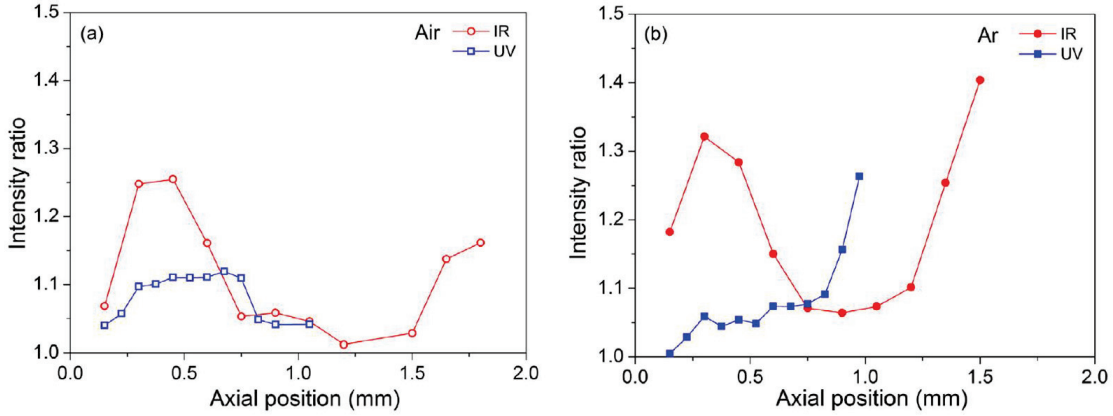

Figure 2.15 Intensity ratio between the two resonant lines of Ca II 393.4 nm and Ca II 396.8 nm as a function of the axial position of the collection fiber with respect to the surface of the sample, for ablation in air (a) and in argon (b) with respectively IR and UV lasers.

2.6 Resume

In this chapter, we have investigated the characteristics of ablation plume induced on float and frosted glasses by IR or UV laser pulse in an ambient gas of air or argon. Both the spectroscopic imaging and time- and space-resolved emission spectroscopy were used for plasma diagnostics in the present study. Our results show that UV laser is versatile for LIBS analysis of float glass as well as frosted glass without inducing excessive surface damages, while IR laser is only suitable for frosted glass analysis. The induced surface damage on a polished dielectric surface such as a float glass is too much for repeated measurements on the same site and for many applications requiring minimal surface damages. In this experiment, the use of frosted glasses allowed for comparative studies of the plasma properties for ablation in air or in argon and with IR or UV laser pulses. Optimal ablation fluence was determined at 43.3 J/cm^2 for IR laser pulse, a similar fluence of 45.3 J/cm^2 was thus used for UV laser pulse, which makes easier the intended comparative study.

The obtained results first show that in all the ablation conditions studied here, the post-ablation interaction can be characterized by the LSC wave, which results in a rather hemispherical form of the plasma with a layered internal structure for different species in

the plume, at short detection delays. Further observations of the profiles of the emission lines, electron density and temperature at longer delays beyond 0.5 μs confirm the characteristics of the morphology of the plasma observed in shorter delays. When comparing between the ablations with IR or UV laser pulses, higher electron densities and higher temperatures are observed for the IR plasma than for the UV plasma whatever in air or in argon ambient. The plasma with IR ablation continues to propagate at longer delays, while the UV plasma is more static. When comparing ambient gases of air and argon, higher electron densities are observed for the IR plasma in argon, and higher temperatures are observed for the UV plasma in argon, which implies a stronger confinement effect of the argon gas. The characteristics of the plasma naturally result in different analytical performances of the plasmas induced in the different conditions. Thus, we observed a shorter delay with UV ablation for an optimal signal-to-noise ratio than with IR ablation. We also observed a higher signal-to-noise ratio with IR laser than with UV laser, in air as well as in argon. Finally, when dealing with resonant emission lines, the plasma induced by UV pulse appears more suffering from self-absorption than that induced by IR pulse, in air as well as in argon. Finally, the use of argon as ambient gas leads to a significantly reduced self-absorption effect for UV plasma and especially for IR plasma.

Chapter 3. Quantitative analysis of powdered materials with surface-assisted laser-induced breakdown spectroscopy

Starting from this chapter, we will turn our focus to the analytical aspect of LIBS. Taking the advantages of laser sampling, LIBS is well-known for its abilities to analyze any kind of substance (gas, liquid and solid state) without sample preparation. Indeed, there are many solid materials that require no sample preparation, for example metals, glasses (as studied in Chapter 2), and polymers. However, for some other types of materials, such as liquids or powders, the LIBS analytical capacity is usually quite limited with direct laser ablation of the samples without any preparation. Some simple sample preparations or treatments may appear greatly useful in this case to achieve high analytical performance with LIBS [42]. In previous works of our group, a so-called surface-assisted LIBS technique has been developed for the elemental analysis in viscous liquids (lubricating oils) [59-61] and soft materials (sunscreen creams) [62]. The purpose of the works presented in this chapter is to generalize the surface-assisted LIBS technique to the quantitative analysis of powdered materials. Such generalization can find much wider applications such as environmental pollution detection, food security, industrial process control, etc. In this chapter, the analytical performances of surface-assisted LIBS on powder samples will be evaluated from a series of calibration graphs built with the cellulose and alumina powders. Special attentions will be focused on the figures-of-merit, normalization procedures, and matrix effects in LIBS analysis. The results obtained with surface-assisted LIBS will be compared to those obtained with classic pellet sample preparation. Preliminary results on soils analysis will also be presented in this chapter.

3.1 Motivation

Elemental analysis in powdered materials represents a very important aspect of analytical needs primarily because of the fact that a very large variety of materials can be mechanically crushed and ground into powders with particle size in the range from tens to hundreds of micrometers. Powders then can be analyzed with LIBS as reported by numerous papers in the literature. Concerned materials include soils [129-131], ashes [132], plants [133,134], foods [135-137], fossil or nuclear combustion materials [138-141], cosmetic powders [142], pharmaceutical products [143] and so on. Elemental analysis in powder is also needed for certain industrial processes such as glass fabrication [144]. Direct laser ablation of powders encounters nevertheless some difficulties since ejection and removal of the powder occur in the laser impact region. One of the most frequently used sample preparation for LIBS analysis of powders consists of pelletizing them. In fact, pellets are very suitable for LIBS measurements with their flat and large surface. Two inconveniences however are often reported in the literature for LIBS measurements of pellets. The first one is due to the fact that powders are not all suitable for preparation by pressing into pellets with good mechanical resistance for laser ablation, or even for sample holding. Binding materials are often needed for pellet preparation [48,145,146]. The second one is even severer because it corresponds to the matrix effect affecting the ability of LIBS to preform quantitative analysis with pellets [19,129-131,133,137,147]. Even though a good pellet preparation, with suitable binders if necessary, can produce pellets with similar mechanical hardness, they can behave differently against laser ablation, because of either inhomogeneity in optical absorption as well as in thermal and mechanical properties on the microscopic scale. Alternative ways are searched to prepare powder samples for LIBS measurements. One of them corresponds to loose powders retained on an adhesive tape [19,148]. It has been demonstrated that with careful sample preparation and correction for sample surface mass density of the powder retained on the tape, the same calibration curve for a given element to be quantified can be obtained for powders of various materials [148].

In this work we demonstrated and evaluated a specific method of powdered material

elemental analysis with LIBS. This method has been inspired from the previous works of our group on wear metal analysis in lubricating oils [59-61] and elemental analysis in sunscreen creams [62]. In those works, the oils or creams were applied on the surface of an aluminum plate in the form of a uniform and thin coating film. A strong IR nanosecond laser pulse transmitted through the coating layer and focused on the substrate, which induced a hot aluminum plasma that in turn interacted with the coating film leading to its evaporation and excitation. The result was a mixture plasma including aluminum vapor but also species from the oil or the cream. A suitable detection system preferentially captured emissions from the elements contained in the thin layer. Standard spectroscopic analysis allowed therefore the determination of their concentrations in the analyzed oils or creams. The primary concern of this method was efficient laser ablation of viscous liquids or soft materials like oils or creams in order to obtain high temperature plasmas which allow sensitive detection of metals in oils or creams. It was shown that temperatures exceeding 15,000 K could be reached for the vaporized oil, which permitted efficient emissions from the constituent elements [59,60]. Further works established the fact that the dominance of the plasma from the substrate, aluminum for instance, in the resulted mixture plasma, efficiently reduces the matrix effect in the LIBS measurement with respect to different types of oil to be analyzed [61]. The demonstrated method, which may be generically called surface-assisted LIBS analysis, is actually a sensitive method practically free of matrix effect for elemental determination in different oils. The application of this method to sunscreens demonstrated its efficiency for powder analysis, since the analyzed sunscreens were in fact prepared by mixing nanoparticles of titanium dioxide (TiO_2) in a matrix of organic cream [62].

The purpose of this chapter is therefore to generalize the surface-assisted LIBS analysis to elemental determination in powders with particle size in the range of several tens of micrometers. As discussed above, such generalization can find much wider applications in important areas such as environmental pollution detection, food security, industrial process control and so on. In the following, we will first present the sample preparation procedure and the measurement protocol used in this work. We will then

focus on the figures-of-merit of the surface-assisted method evaluated from the calibration graphs using a cellulose powder. We will especially show the efficiency of a proper choice of reference line to improve the analytical performances. In the second step, we will study the matrix effect by preparing another series of samples with an alumina powder. The results obtained with surface-assisted method will then be compared to those obtained with classic pellet method. Finally, we will apply this method to the analysis of soils as real powder samples. The matrix effect of this method will be further evaluated and compared to the pellet method for soils analysis.

3.2 Sample preparation and measurement protocol

3.2.1 Sample preparation

Pure powders of cellulose [$(C_6H_{10}O_5)_n$] and alumina (Al_2O_3) were used as two different matrices of powdered material with clearly different compositions, organic for the first and mineral for the second. Both of them were purchased from Sigma-Aldrich with the product number S3504 for the cellulose powder with a typical particle size of 20 µm, and 265,497 for the alumina powder with an average particle size of ≤ 10 µm (purity 99.5%). The powders were spiked with pure titanium dioxide (TiO_2) nanoparticles by weighing them with a microbalance. Several steps of mixing were necessary (2% then 0.2% before lower concentrations) to successively dilute the concentration of TiO_2 particles into the matrix powders until the final targeted Ti concentrations in the matrix powders, in the range from 25 to 5000 ppm by weight, were obtained. Each intermediate mixture powder was put into a shaking machine for vigorous shaking for 5 min to ensure the homogeneity of the mixtures. About twenty samples were thus prepared for each matrix powder with Ti concentrations in the desired concentration range.

For surface-assisted LIBS measurements, a pure aluminum plate (Techlab, Al 99.99%, Cu 0.005%, Si 0.002%, Fe 0.001%) was polished and cleaned (deionized water then alcohol). A volume of spiked powder of 0.3 ml was placed in the middle of the aluminum plate. Oil (75 cSt hydrocarbon base oil from Techlab) was dropped into the powder until a volume ratio of 1:1.2 (oil:powder). The resulted material was stirred to mix completely

the oil and the powder until a uniform paste was obtained. The paste was then spread using a glass slide on the surface of the aluminum plate, forming finally a uniform thin film as shown in Fig. 3.1. The thickness of the coating layer was estimated to be 40 ± 10 μm. In such preparation, all the materials deposited on the plate, powder and oil, were left on the surface, in such way that the volume of powders applied on the surface of the aluminum plate was kept constant for different samples. Note however that the densities of the two matrix powders cellulose and alumina were different, so the surface mass densities were different for the two series of samples. In order to normalize the recorded spectra according to the surface mass density of the powders, we measured the mass densities of the two powders, $\rho_{cellulose}$ and $\rho_{alumina}$. The obtained ratio $\gamma = \rho_{alumina}/\rho_{cellulose} = 3.72$, was then used to correct the spectra from the spiked alumina powders in order to normalize to constant mass of Ti applied on the aluminum plate. Despite the great carefulness taken in the sample preparation, the uniformity and thickness of the samples could fluctuate. We will come back later in the following to the correction of such fluctuation by normalizing the recorded spectra with a reference line. After each measurement, the aluminum plate was cleaned (deionized water then alcohol) and re-polished for a new sample.

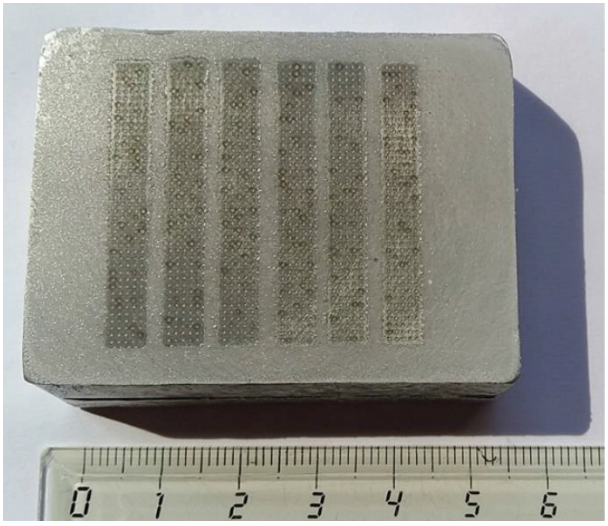

Figure 3.1 Photograph of a thin film sample on the surface of an aluminum plate with a ruler showing the dimension of the plate. The visible marks on the sample surface are caused by laser ablation.

In parallel, pellets were also prepared for the two series of spiked powders of cellulose

and alumina. For the cellulose powders, pellets could be obtained directly by pressing 0.5 g of powder under a pressure of 667 MPa (6.8 t/cm^2) for 5 min. For the spiked alumina powders, pure cellulose powders were used as binder at a mass ratio of 1:4 (cellulose:alumina) to form pellets with good mechanical strength under the same pressure condition and with the same mass as for the spiked cellulose powders. The Ti concentrations of the prepared pellets were therefore recalculated by multiplying by a factor of 0.8 those of the corresponding spiked alumina powders. The resultant pellets had a diameter of 13 mm, and a thickness of 2.5 mm and 1.5 mm for the cellulose and alumina powders, respectively.

3.2.2 Measurement protocol

A detailed description of the experimental setup can be found in Section 2.2 of this manuscript. In this work, we used the fundamental laser wavelength of 1064 nm for ablation. The laser pulse energy was optimized at 120 mJ for thin film samples and 60 mJ for pellet samples. The laser spot on the target surface was estimated to be 300 μm in diameter, which resulted in a fluence of 170 J/cm^2 and 85 J/cm^2 for thin films and pellets, respectively. A microscope glass plate placed under the focusing lens was used to shield the lens from the ejected debris. The spectral emission detection system was the same as that in Fig. 2.1, and the spectroscopic imaging system was available in the experiment for a complementary study of the plasma morphology.

For the thin film measurements, each spectrum was an accumulation of 200 single-shot ablations performed in a matrix of 5 × 40 craters, with a center-to-center distance of 800 μm between the neighboring craters (craters visible in Fig. 3.1). The entrance of the fiber was centered at the symmetrical axis of the plasma and situated at a height 2.0 mm above the sample surface. This distance was the optimum to capture the emission from the powder. The detection window was set with a delay of 2 μs and a width of 5 μs after the impact of the laser pulse on the sample. For the pellet measurements, each spectrum was accumulated over 200 laser shots in 10 craters with each of them ablated by 20 consequent laser pulses, and a distance of 600 μm between the neighboring craters. Due to the different characteristics of the plasma, the distance between the entrance of the

fiber and the sample surface was set to be 1.3 mm. The detection window was set with a delay of 1 μs and a width of 2 μs. For a given sample, 6 replicate measurements were performed in order to extract the average intensity and the standard deviation of a given line.

3.3 Figures-of-merit of the method and optimization with spectrum normalization

3.3.1 Raw spectra

LIBS spectra were first taken with spiked cellulose powders using the measurement protocol described in the previous section (Section 3.2.2). The most intense titanium line in the spectrum, Ti II 334.9 nm line (ionization energy + excitation energy ≈ 11 eV), was used to establish the calibration graph for quantitative determination of Ti in the cellulose powder. The use of the above resonant line of the titanium ion necessitated a check of the line shape to ensure the absence of severe self-absorption and self-reversal for the line. The raw spectra in the neighborhood of this line for spiked powders with Ti concentrations ranging from 50 to 400 ppm by weight are shown in Fig. 3.2. We can see in this figure that for the 50 ppm sample, the Ti II line can be clearly distinguished from the background noise. This is indicative of a LOD under this concentration range. We also remark that the line intensity, defined in this work for simplicity, as the height of the line with respect to the baseline in the vicinity, generally increases with the Ti concentration. But irregularity happens. For example, we can observe in Fig. 3.2 a reversal in intensity change for Ti concentrations from 300 ppm to 400 ppm. This can be typically caused by a relatively important fluctuation of the thickness of the thin film on the aluminum plate. We will show in the next section how spectrum normalization with a reference line can reduce the effect of such fluctuation.

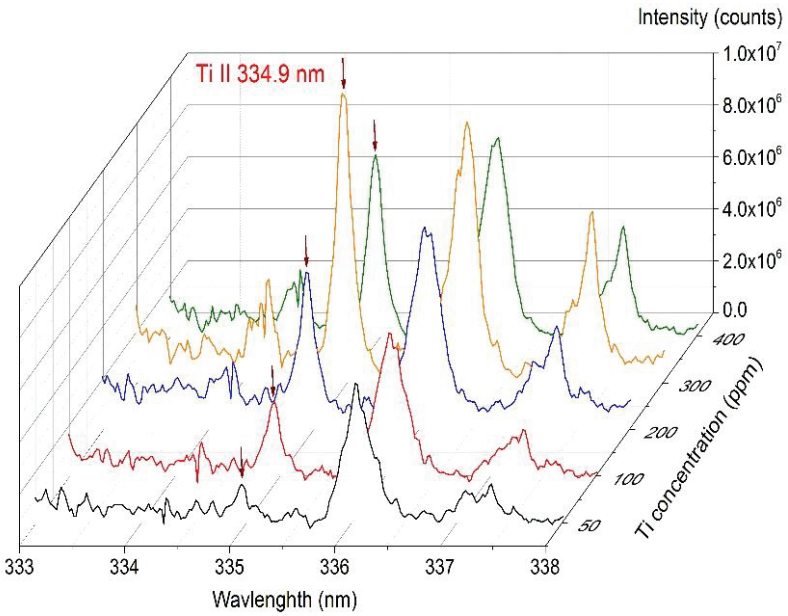

Figure 3.2 Raw LIBS spectra in the spectral range around the Ti II 334.9 nm line from spiked cellulose powders with different Ti concentrations ranging from 50 to 400 ppm with the surface-assisted analysis method.

3.3.2 Calibration graphs, R^2, LOD and LOQ, improvement with spectrum normalization

To obtain calibration graphs, the intensities of the Ti II 334.9 nm line extracted from the LIBS spectra of the spiked cellulose powders are plotted as a function of Ti concentration. Fig. 3.3(a) shows the calibration graph built with the line intensities without any normalization. The data points correspond to the average line intensities and the error bars are the related standard deviations. The data are fitted with a quadratic regression, $y = a + bx + cx^2$. The determination coefficients R^2 that express the degree of correlation of the experimental data to the regression [90] are indicated in Fig. 3.3. The theoretical LODs are also presented in Fig. 3.3. Their values were calculated according to the usual definition, i.e., LOD = 3 σ_a/b, where σ_a is the standard deviation of the spectrum background and b the linear slope of the regression curve. In order to extract the LOQ values, the confidence bands [90] are plotted in the figure (at a confidence level of 95%). LOQ corresponds then to the highest concentration (determined by the lower confidence band) related to the lowest line intensity that can be measured with confidence over the spectrum background (determined by the higher confidence band) [97]. As mentioned in Section 1.3.2, this method of LOQ is based on the confidence bands of the calibration

graphs that take into account the uncertainties due to regression.

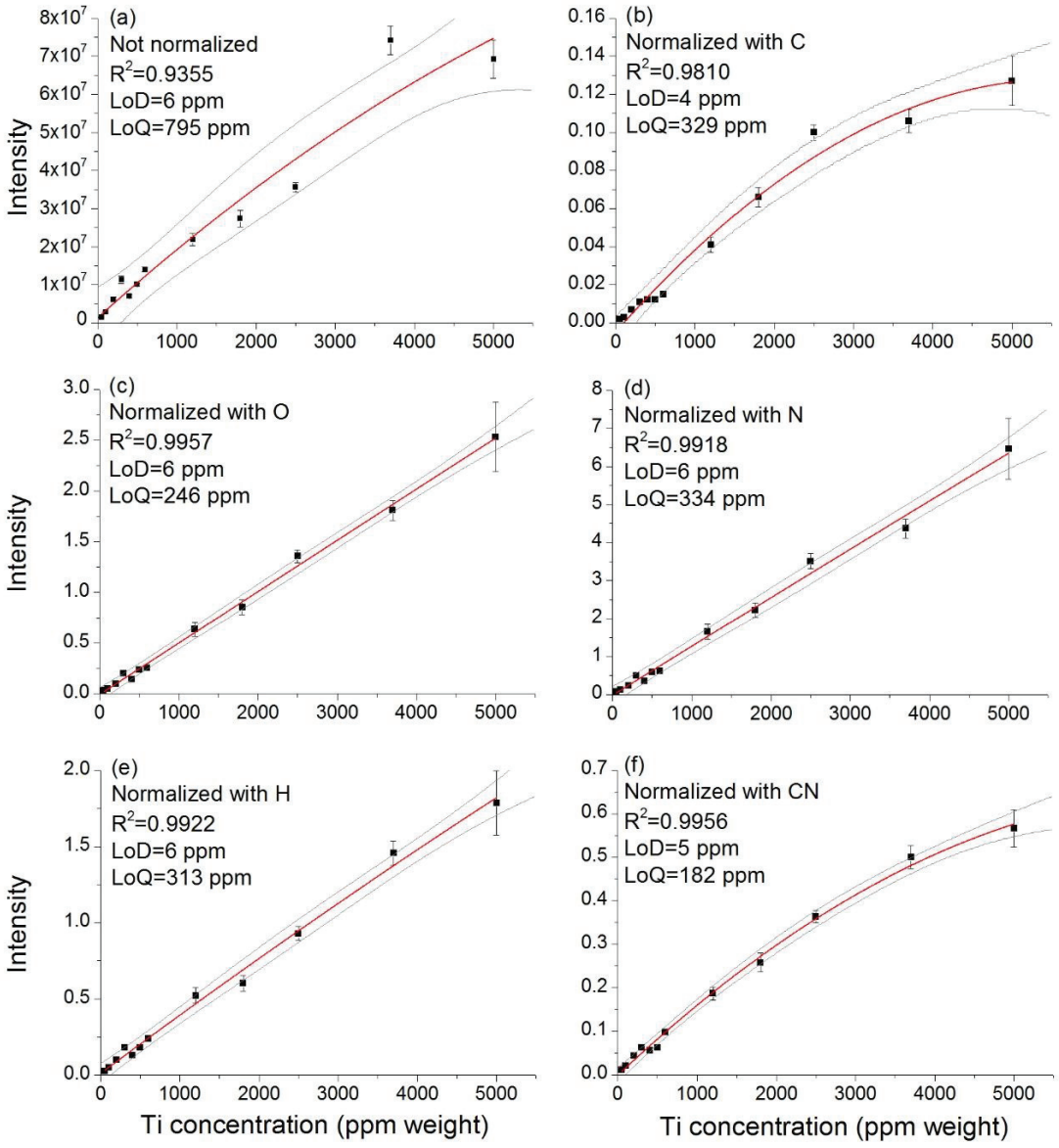

Figure 3.3 Calibration graphs for the Ti II 334.9 nm line obtained with quadratic regression (red solid curves). The experimental data points correspond to the average intensities and the error bars to the line intensity standard deviations of the replicate measurements. The confidence bands are also plotted in the figures in solid gray lines. The parameters related to the figures-of-merit of the calibration graphs are indicated in the figures. The line intensities shown are without normalization (a), normalized with the C I 247.9 nm line (b), normalized with the O I 777 nm line (c), normalized with the N I 746.8 nm line (d), normalized with the H I 656.3 nm line (e) and normalized with the CN 386.1 nm band (f).

In Fig. 3.3(a), we can see that without normalization, the correlation of the data with the fitting function is not good even with a quadratic model. The R^2 value is only 0.9355

which is usually not satisfactory for a quantitative analytical technique [90]. Correspondingly, a mediocre LOQ of 795 ppm by weight is determined. However, a relatively low LOD value of 6 ppm by weight is extracted. This is because it only depends on the slope of the calibration curve at small concentrations and the background noise of the spectrum. These observations on the calibration graph of Fig. 3.3(a) are quite consistent with our aforementioned remarks about the sample-to-sample fluctuations of the raw spectra. To compensate for such fluctuations and improve the correlation between the experimental data and the regression model, normalization of the spectra with a reference line should be used. The usual criteria for choosing a reference line correspond to lines from a matrix element considered as an internal standard, with similar excitation energies as the line to be normalized [107]. The carbon C I 247.9 nm line was thus chosen as the reference line (excitation energy = 7.7 eV) since carbon is a matrix element. The calibration graph with C I 247.9 nm line normalization is shown in Fig. 3.3(b). We can see R^2 increased significantly to 0.9810. This value is however still not good enough to satisfy the usual requirement of $R^2 \geq 0.99$ for a quantitative analytical technique [90]. The corresponding LOQ of 329 ppm by weight is also relatively high.

Other attempts led us to try emission lines from other elements available in the spectra, from O, H, or N for example. The two first, O and H exist in the matrix (cellulose) but they can also be contributed by the ambient gas (O_2 and H_2O). The third, N, can only be contributed by the ambient gas (N_2). However, surprisingly, better figures-of-merit could be obtained by normalization with the lines from these elements, as can be seen in Fig. 3.3(c), (e) and (d). Indeed, using the O I 777 nm line (excitation energy = 10.8 eV), the H I 656.3 nm line (excitation energy = 12.1 eV) and the N I 746.8 nm line (excitation energy = 12.0 eV), calibration graphs with R^2 of 0.9957, 0.9922 and 0.9918, respectively, could be obtained. These R^2 value are above the acceptable value for a quantitative analytical technique. Correspondingly, the LOQ values are improved to 246, 313 and 334 ppm, respectively. The band-head of the CN radical at 386.1 nm was also tested as a reference line for spectrum normalization, as shown in Fig. 3.3(f), and good figures-of-merit were obtained as well. We remark that the difference between CN and C is the implication of

N which is contributed by the ambient gas.

We can thus deduce from the results shown in Fig. 3.3 that with the help of a suitable reference line from an element (or molecule), the normalized line intensities allow building calibration graphs with good figures-of-merit for quantitative analysis of Ti in cellulose powder. This proves the efficiency of the developed surface-assisted LIBS analysis method for elemental determination in powers. The spectral normalization procedure is clearly needed because of the manual preparation of the thin film on the aluminum plate in absence of any precise film homogeneity and thickness control. The most suitable reference line is not necessarily provided by an internal reference defined in the usual way, by an element of the matrix. This unexpected behavior leads us to perform the investigations described in the next section to better elucidate the origins of the elements providing "good reference lines" and the mechanism leading to such a good performance for the fluctuation correction.

3.3.3 Elements from the ambient gas as good references for spectrum normalization

In order to study the mechanism of the observed efficient spectrum normalization and the origin of the involved reference elements, we used the spectroscopic imaging system available in our experiment to observe the morphology of the plasmas induced in LIBS analysis of the thin film of a spiked cellulose powder. The principle and the detailed description of the used imaging system can be found in Section 2.2.2. Table 3-1 specifies the spectral lines used for each studied species and the associated on- and off-filters. As a complementary diagnostics, we also measured the temperature profile of the plasma along the laser incidence axis, by recording the emission spectrum at different heights of the plume and by extracting the electron temperature from the recorded spectra using Saha-Boltzmann plots of Ti I and Ti II lines. The used lines included Ti I 453.3, 498.2, 499.1, 499.9 nm lines and Ti II 323.6, 323.9, 332.3, 336.1, 337.3 nm lines. The needed electron density for the Saha-Boltzmann plot was extracted by the Stark broadening of the H I 656.3 nm line. The measurements were performed with a spiked cellulose powder with a Ti concentration of 5000 ppm weight.

Table 3-1 Emission lines selected for characterizing the species of Ti II, C I, O I and CN, and the characteristics of the corresponding on- and off-filters for the spectroscopic images of the species.

Species	Lines	Central wavelength (nm)		Bandwidth (nm)
		On-filter	Off-filter	
Ti II	334.9 nm	337	340	10
C I	247.9 nm	250	220	10
O I	777 nm	780	760	10
CN	385.1, 385.4, 386.1, 387.1 nm	380	370	10

The spectroscopic images for the studied species and the axial electron temperature profiles are shown in Fig. 3.4. We specify here that the illustrated images correspond to emissivity images that were obtained by dual-wavelength differential spectroscopic imaging technique [123], as described in Section 2.2.2. The raw emission images from the ICCD camera were firstly treated with the Abel inversion to get the emissivity images. The intensity of an emissivity image is proportional to the density of the corresponding species in the plasma in a plane intersecting the plasma into two equal parts by passing through the symmetrical axis of the plasma, i.e. the propagation axis of the ablation laser beam. The separately obtained emissivity images for the four species were then superimposed in the same picture for an easy observation of their respective positions in the plume. For a good visibility, different colors are associated to the different species in the figure: blue to O I, white to Ti II, red to CN and green to C I. Such multi-species emissivity image is shown in Fig. 3.4 for the different detection delays of 500, 1000, 2000 and 4000 ns together with the corresponding axial electron temperature profile.

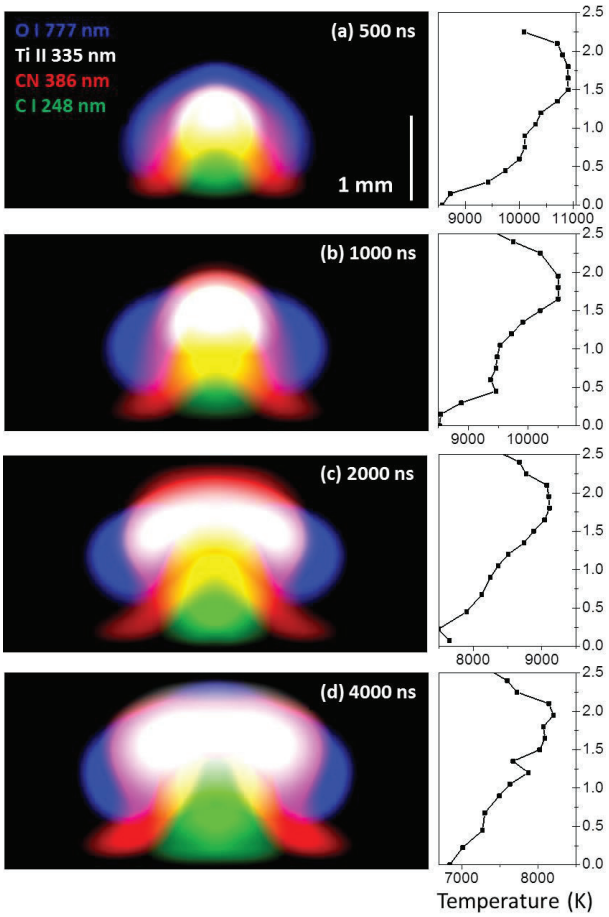

Figure 3.4 Multi-species emissivity images of O I (in blue), Ti II (in white), CN (in red), and C (in green) at the delays of 500 ns (a), 1000 ns (b), 2000 ns (c) and 4000 ns (d). The physical dimension of the images is indicated in (a) and the bottom of the images corresponds to the sample surface. The axial electron temperature profiles at different delays are plotted on the right side of the images with a corresponding vertical scale.

Segregation of the different species in the plasma can be clearly observed in Fig. 3.4. On the one hand, in the interval when the emission spectra were recorded for LIBS measurements after a delay of 2 μs, the Ti II population is located in a zone between 1 mm and 2.5 mm away from the sample surface. While the C I population is found in a zone close to the sample surface from 0 mm to 1 mm. Combining with the observed axial temperature profile, we can understand that these two populations are separated in two zones inside the ablation plume with quite different temperatures. This explains their weak correlation and the mediocre improvement of the data correlation in the calibration graph obtained by normalizing the Ti II line with the C I line. On the other hand, in the same time interval, the O I population is found in the same zone in height as the Ti II

population. In fact, the first surrounds the second as we can see in Fig. 3.4. They experience therefore the same temperature range in the axial temperature profile. As we can expect a smooth temperature variation in the transverse direction of the plasma [52], we deduce thus the two populations of Ti II and O I experience a similar environment in the plume. We understand therefore why the normalization with the O I 777 nm line leads to better figures-of-merit parameters. Not only the excitation energy of the O I line is quite close to the total excitation energy (ionization + excitation) of the Ti II 334.9 nm line, but also the two species overlap each other in a same zone in height inside the plume. A similar observation can be made for the CN population in Fig. 3.4, which explains its good performance in the fluctuation correction of the Ti II line. Moreover, since CN radicals are formed in the plume by recombination between carbon evaporated from the sample and nitrogen from the background gas, and since the C I population is found very close to the sample surface, the overlapping of the CN population with the Ti II one is necessarily due to the nitrogen from the ambient gas.

However, the question remains as to determine the origin of the observed excited species in LIBS spectra, such as O I and H I, which can in principle come either from the matrix or the ambient gas. In order to have a clear answer, we show in Fig. 3.5(a) to (d) the emissivity images of O I 777 nm line at very short delays recorded for plasmas induced with the thin film of a spiked cellulose powder. We can see that the emission from O I comes at very short delays, from the front of the plume, where the initiated shockwave is located right after the material ejection from the surface. Previous works of our group show that in the atmospheric air, excited population of O I appears due to the dissociation of O_2 molecules in the shockwave [58], which occurs within a very short delay with the supersonic propagation of the shockwave, much faster than the propagation of the ablated materials. We deduce therefore that the initially observed O I population is contributed by the ambient gas only. The evolution of this population [Fig. 3.5(a) to (d)] clearly shows that it is supplied by a continuous contribution from the ambient gas with the further propagation of the shockwave, which becomes more spherical at longer delays. A different case corresponds to the ablation of a silicate glass (SiO_2). A series of O I 777

nm line emissivity images [Fig. 3.5(e) to (h)] of the plasma induced on a glass sample shows an initial population of O I developed from the front of the plasma as in the case of powder thin film on aluminum plate. In addition, a second population of O I propagating upward from the sample surface appears at a delay of 90 ns and contributes to the final total O I population in the plasma.

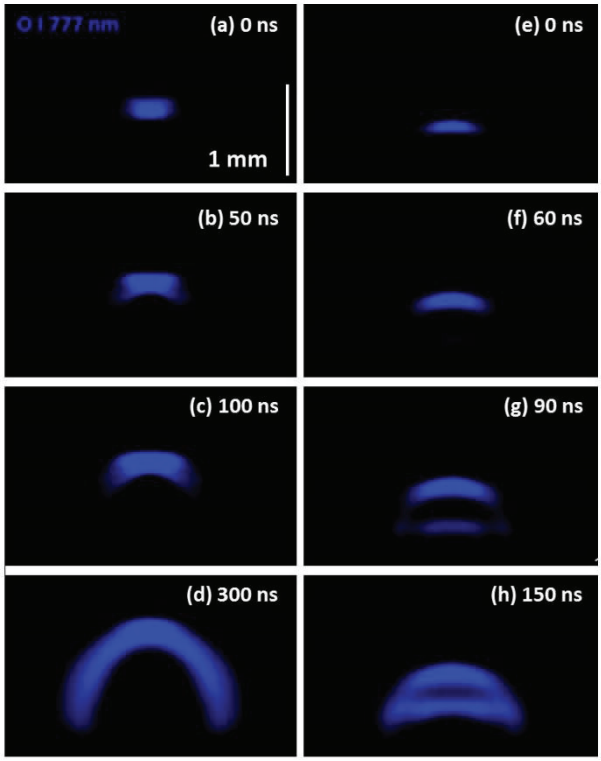

Figure 3.5 Emissivity images of O I (in blue) of the plasmas induced on the aluminum plate with a thin film of powder [(a) to (d)] and on a glass sample [(e) to (h)]. The delays of image recording are indicated in the images. The physical dimension of the images is indicated in (a) and the bottom of the images corresponds to the sample surface.

We conclude therefore that elements contributed by the ambient gas can also provide suitable reference lines for efficient spectrum normalization which significantly improves the figures-of-merit of a calibration graph. In an inhomogeneous spectroscopic emission source like laser-induced plasma for LIBS, an additional condition should be taken into account in the choice of reference lines for spectrum normalization beside the several usual considerations: the reference elements should spatially overlap the elements for which the emission needs to be normalized.

3.4 Study of the matrix effect: comparison with pellets

In this section, we will focus on the matrix effect in elemental determination in powders. Especially, results will be shown for the measurements on the two series of spiked powders of cellulose and alumina. The calibration curves are built for these two powders of different natures: organic powder with cellulose and mineral powder with alumina. Such comparative study will be presented for the two sample preparations: the thin film preparation developed in this work and the classic pellet preparation.

3.4.1 Raw spectra of the cellulose and alumina powders prepared in thin film or in pellet

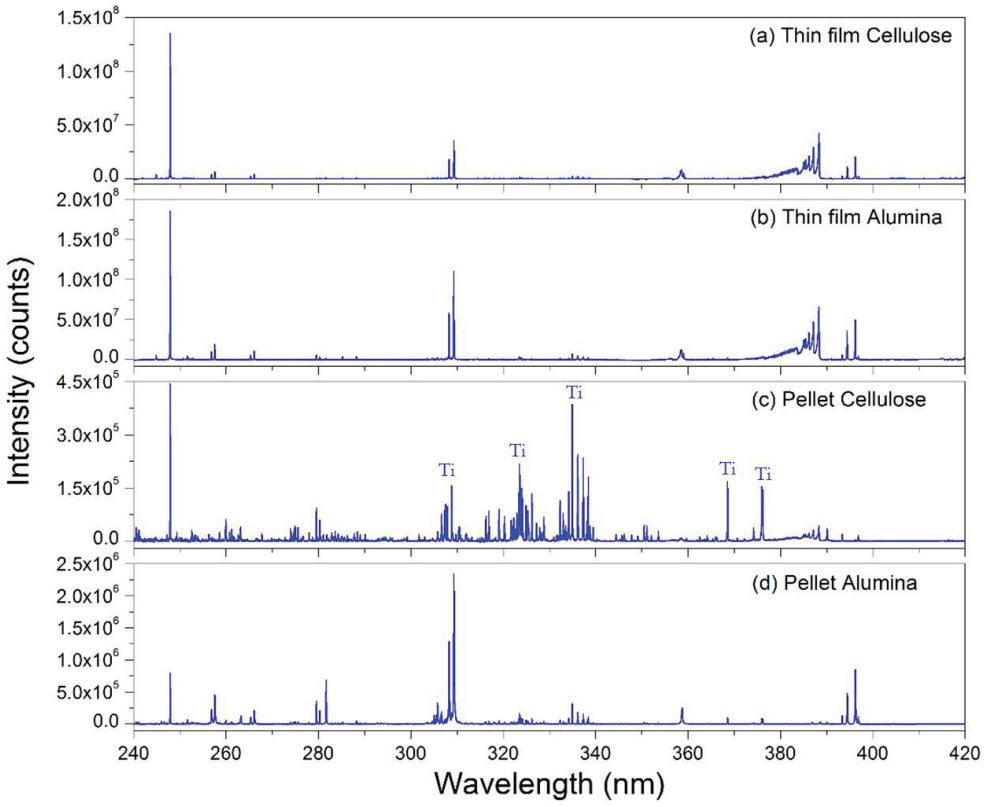

Figure 3.6 LIBS spectra in the spectral range from 240 nm to 420 nm of cellulose [(a), (c)] and alumina [(b), (d)] powders spiked into a Ti concentration of 400 ppm by weight, prepared in thin film [(a), (b)] or in pellet [(c), (d)].

Raw spectra from the spiked cellulose and alumina powders are shown in Fig. 3.6 for the two sample preparation methods of thin film and pellet. The Ti concentration of the measured samples is 400 ppm by weight. At first glance, we can already remark the

similitude between the spectra of the two powders prepared in thin film, whereas those of the samples prepared in pellet appear very different.

3.4.2 Calibration curves for Ti determination in cellulose and alumina powders prepared in pellet

To confirm the impression gotten from the inspection on the raw spectra, calibration curves are first plotted with the two series of spiked powders prepared in pellet. For this purpose, the line intensities of the Ti II 334.9 nm line extracted from the spectra recorded for these two series of pellets are first plotted as a function of Ti concentration [Fig. 3.7(a)]. We can clearly observe the different behaviors between the two powders. At low concentrations, the slope of the calibration curve of the cellulose powder is larger than that of the alumina powder. This indicates a matrix effect between the two powders when they are prepared in pellet for LIBS measurement. The more sensitive response of the cellulose powder may probably be due to a higher mechanical hardness of the pellets formed from the cellulose powder that helps to get a more efficient laser ablation, i.e., a larger ablated mass and a larger atomization degree and thus a denser plasma. This argumentation could be confirmed by the observed curvature of the calibration curve for the cellulose pellets at high Ti concentrations [Fig. 3.7(a)], which can correspond to self-absorption of the resonant Ti II 334.9 nm line [62]. Calibration curves are then built with a weak non-resonant Ti II 457.2 nm line as shown in Fig. 3.7(b). We find that the curvature of the calibration curve of the cellulose powder disappears, which leads to an even larger discrepancy between the two calibration curves due to the matrix difference between the pellets formed from the two powders. In addition, we can extract LODs from the calibration curves built with pellets. A LOD of 3 ppm and 5 ppm by weight are respectively found for the cellulose and the alumina powders, which is comparable to the LOD values extracted for these two powders with thin film sample preparation.

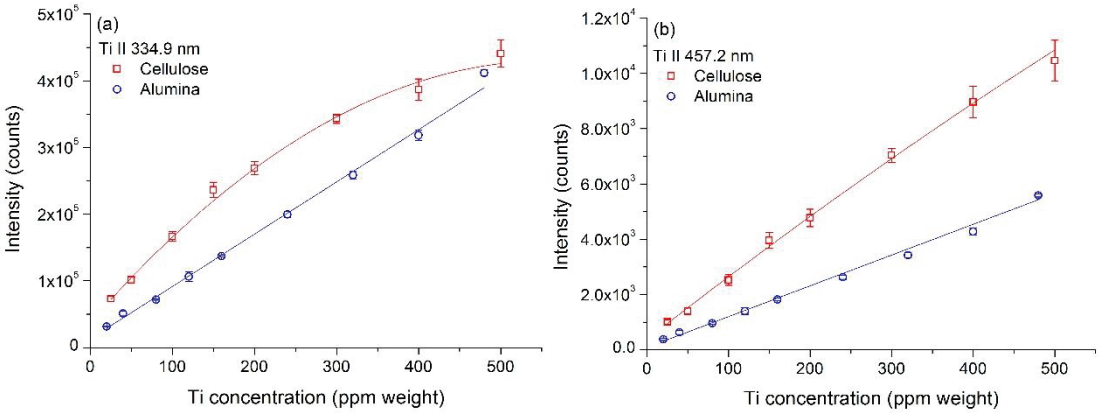

Figure 3.7 Calibration curves of the Ti II 334.9 nm line (a) and the Ti II 457.2 nm line (b) for cellulose and Al_2O_3 powders prepared in pellet.

3.4.3 Calibration curves for Ti determination in cellulose and alumina powders prepared in thin film

Calibration curves are then built with the two series of spiked powders of cellulose and alumina prepared in thin film. For this purpose, the line intensities of the Ti II 334.9 nm line extracted from the LIBS spectra recorded for these two series of spiked powders were first normalized with the O I 777 nm line, because of its efficiency in the correction of sample-to-sample fluctuation of the spectra. Then, the relative intensities of the Ti II 334.9 nm line obtained for the alumina powder were divided by the ratio between the densities of the two powders, $\gamma = \rho_{alumina}/\rho_{cellulose} = 3.72$. In this way, the relative line intensities are normalized with the surface mass density of the analyte (Ti) deposited on the aluminum plate surface. This second normalization was necessary because, in the thin film preparation, the quantity of powder deposited on the aluminum plate for each thin film sample was measured by volume. The doubly normalized intensities of the Ti II 334.9 nm line are then plotted as a function of the Ti concentration, as shown in Fig. 3.8. We use a linear regression, $y = a + bx$, to fit the data of the two powders.

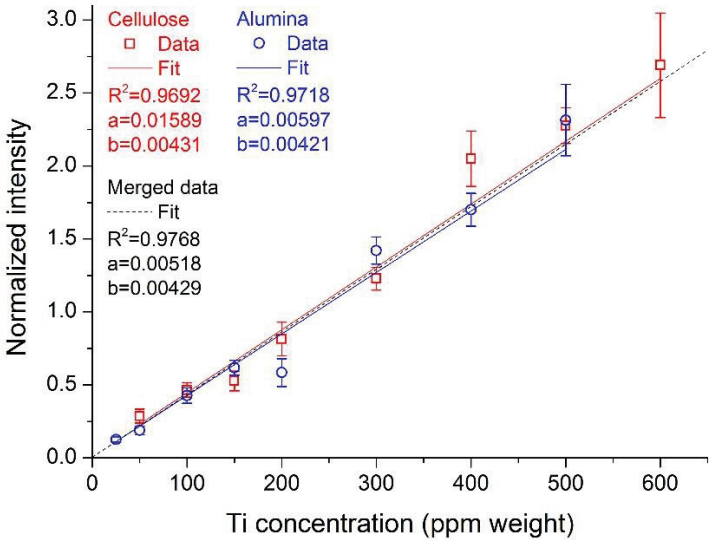

Figure 3.8 Calibration curves with the Ti II 334.9 nm line for cellulose and alumina powders prepared in thin film. The fitting parameters with linear regression are indicated in the figure for the cellulose data, the alumina data and the merged data of the two powders.

From Fig. 3.8 we can see that, different from the case of pellets, the two sets of data obtained with thin film analysis lead to very close calibration curves. Their slopes, b, are slightly different by 2.3% only and their intercepts, a, are also very similar. We can then merge the two sets of data. The merged data are again fitted with a linear regression (black dotted line in Fig. 3.8). We can see that the merged data still have a good correlation similarly to the separated data sets for the two powders. The resulting slope is very close to the slopes for the separated data. These results demonstrate clearly the efficient reduction of the matrix effect between cellulose and alumina powders prepared in thin film. A universal calibration curve could thus be considered for the determination of Ti in different powders, at least for cellulose and alumina powders with particle sizes similar to those concerned in this work.

3.5 Analysis of soils as real powder samples

In this section, we will focus on the analysis of soils as real powder samples. Compared to cellulose and alumina powders that we studied above, spectrum of soils is quite complex with enormous lines from the contained elements such as Ca, Si, Al, Mg, Fe, Ti, Mn and so on. There are many studies [129-131] that have observed matrix effects in the

analysis of soils with LIBS, which is a severe drawback of the technique for the quantitative purpose [101]. In this work, we will make an assessment of the matrix effect by comparison between different types of soil samples, prepared with the surface-assisted LIBS method developed in this work and the classic pellet method. In the following, we will first present the sample preparation procedure for soils, and then show the calibration graphs of soil samples prepared in pellet and in thin film.

3.5.1 Soil samples and their preparation

Four different soil samples were studied in the experiment. Two of them were standard reference materials (SRM) from NIST, NIST 2710 (https://www-s.nist.gov/srmors/view detail.cfm?srm=2710a) and NIST 2587 (https://www-s.nist.gov/srmors/view detail. cfm?srm=2587), and respectively named as N1 and N2 in this work. Other two soils were respectively collected from two different places, one near a river (sand-like soil) and the other near an agriculture area (yellow colored soil) in the region of Lyon, with unknown elemental compositions and therefore named as U1 and U2 in this work.

The 2 NIST samples were prepared in fine and uniform powder of particle diameter of < 75 μm (200 mesh). For the 2 collected soil samples, the raw soils were first dried ground and then sequentially sieved through stainless steel sieves of 100, 200 and 400 mesh apertures (ASTM), corresponding to resulted particle diameters of respectively 150, 75 and 38 μm, assisted by an electromagnetic vibratory shaker. We finally obtained powders with particle diameter of < 38 μm for the 2 collected soils.

In each type of soil powder, silver (Ag) as analyte was added in different concentrations, by mixing the soil powder with Ag solutions at different concentrations obtained by dilution with deionized water, of an Ag standard solution (2 % nitric acid solution at an Ag concentration of 1000 mg/L). Note that the content of Ag in natural soils is negligible (under the LOD of LIBS technique). For the 2 NIST samples, the NIST 2710 (N1) sample is specified with an informative silver concentration of 40 mg/kg. For the NIST 2587 (N2) sample, there is no specification of silver concentration.

In order to have an internal reference element, a standard solution of yttrium (Y)

(10000 mg/L, 5% HNO_3) was mixed to the powders. Note that the content of Y in natural soils is negligible (under the LOD of LIBS technique). For the 2 NIST samples, the NIST 2587 (N2) sample is specified with an informative yttrium concentration of 15 mg/kg. For the NIST 2710 (N1) sample, there is no specification of yttrium concentration.

The detailed sample preparation information is shown in Table 3-2 bellow.

Table 3-2 Products used for preparing the soil powder samples and the obtained analyte and internal reference concentrations.

Soil powder (g)	Ag solution			Y solution	Ag* concentration after drying (ppm)	Y* concentration after drying (ppm)
	1000 ppm Ag standard solution (μL)	Deionized water (μL)	Diluted Ag solution (μL)	10000 ppm Y standard solution (μL)		
0.5	10	390	400	100	20	2000
0.5	25	375	400	100	50	2000
0.5	50	350	400	100	100	2000
0.5	100	300	400	100	200	2000
0.5	200	200	400	100	400	2000
0.5	300	100	400	100	600	2000
0.5	400	0	400	100	800	2000

* without taking into account of the initial concentration of the element.

Therefore, we got three series of soil samples, N2, U1 and U2, with Ag concentrations of 20, 50, 100, 200, 400, 600, and 800 ppm weight, if we admit the fact that in these samples the initial Ag concentration is negligible with respective to the LOD of our detection method. In the same time, for the N1 sample, we got a series powders with Ag concentrations of 60, 90, 140, 240, 440, 640, and 840 ppm weight. And in each of the above 4 series of powder samples, there is a constant Y concentration of 2000 ppm, if we neglect the initial Y content of 15 ppm in N2 sample.

Similarly to the description of the thin film preparation in Section 3.2.1, a mass of soil powder of 0.1 g (an electronic balance was used to precisely weight the powders) was put on the aluminum plate, and mixed with 0.1 mL base oil (75 cSt hydrocarbon base oil,

Techlab, France) to form a uniform paste. The paste was then spread using a glass slide to form finally a uniform thin film on the surface of the aluminum plate as shown in Fig. 3.9. No material was taken away from the surface. Therefore, the surface mass density of the material deposited on the plate was kept constant for different samples. For the pellet preparation, a 0.2 g soil powder was directly pressed under a pressure of 667 MPa (6.8 t/cm^2) for 5 min to form a pellet with a diameter of 13 mm. The measurement protocol for the experiment was the same as that in Section 3.2.2.

Figure 3.9 Photograph of a thin film soil sample on the surface of an aluminum plate. The visible marks on the sample surface are caused by laser ablation.

3.5.2 LIBS spectra of soil powders prepared in pellet and in thin film

Typical spectra of soil powders (N1 soil sample, NIST 2710) prepared in pellet and in thin film are shown in Fig. 3.10, with in the inset a detailed spectrum around the strong Ag I 328.1 nm line used in this work for the quantification of Ag. In the inset we can find the spectral lines from the initially contained elements of Cu (3420 ppm), Zn (4180 ppm), Ti (3110 ppm), Fe (43200 ppm), and the added elements of Ag (440 ppm) and Y (2000 ppm). It is noted that there is no interference of this Ag line with other lines in the spectrum for the tested soil samples.

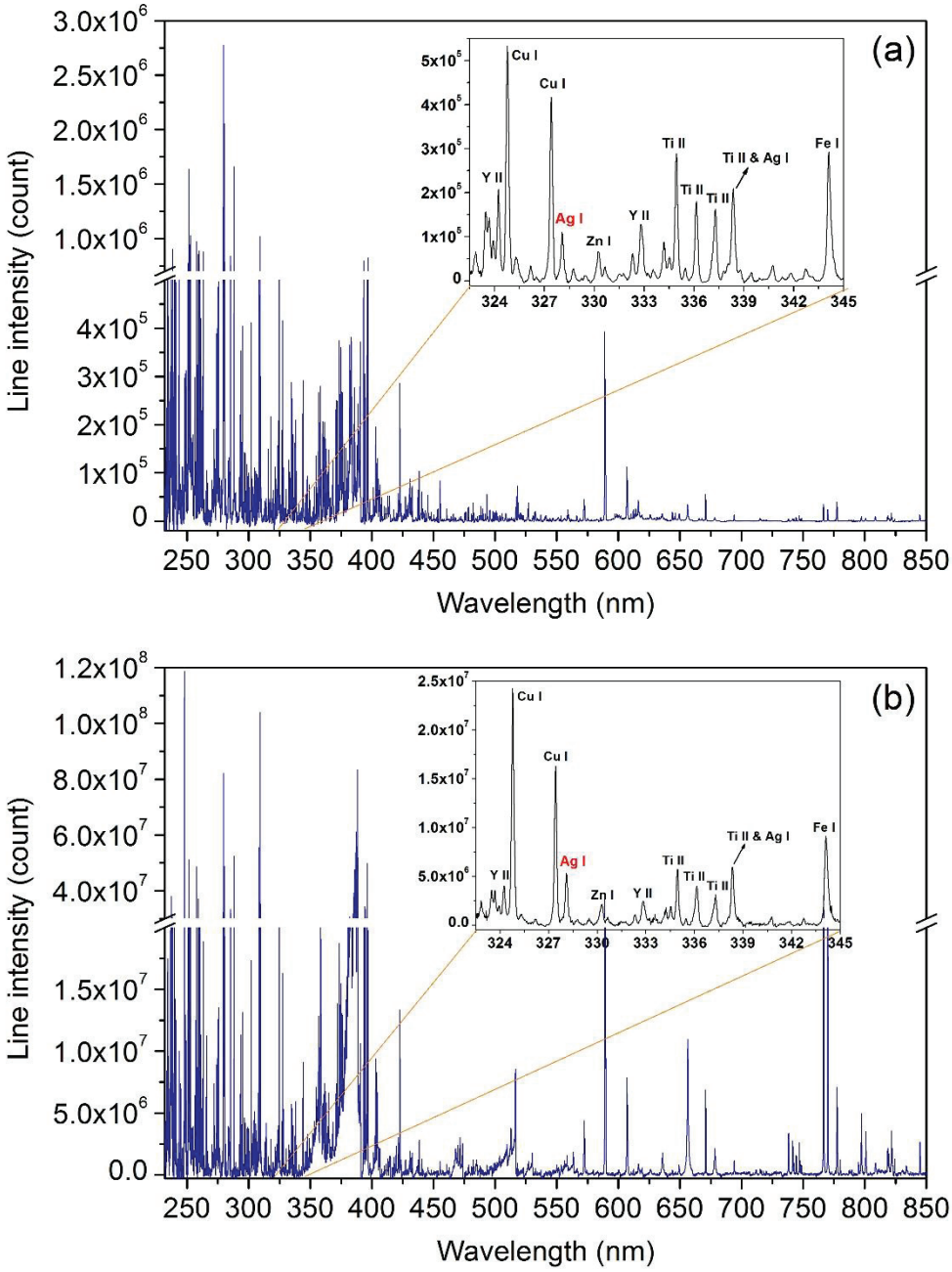

Figure 3.10 Typical spectra of soil powder samples, a) sample prepared in pellet, b) sample prepared in thin film on aluminum target. In the inset of each figure, the detailed spectrum around the Ag I 328.1 nm line is shown. Sample used to obtain the spectra: N1 soil sample (NIST 2710), initially containing the following elements: Cu (3420 ppm), Zn (4180 ppm), Ti (3110 ppm), Fe (43200 ppm), and added Ag (440 ppm) and Y (2000 ppm).

3.5.3 Calibration graphs of soil powders prepared in pellet and in thin film

Calibration curves with the Ag I 328.1 nm line without normalization

In this section, the calibration curves for Ag established with the Ag I 328.1 nm line for

the 4 soil samples are presented first with the intensity of the line. The calibration curves established with samples prepared in pellet are shown in Fig. 3.11. The parameters extracted from the linear regression, $y = a + bx$, of the data are shown in Table 3-3. We can observe a clear matrix effect, since the slopes b of the calibration curves vary a lot over the 4 different soils. A relatively large relative standard deviation (RSD) of b was calculated as 24.3%. In Table 3-3 we can also see quite low R^2 values, which might be contributed both by the experimental fluctuation and the inhomogeneity of the prepared pellets.

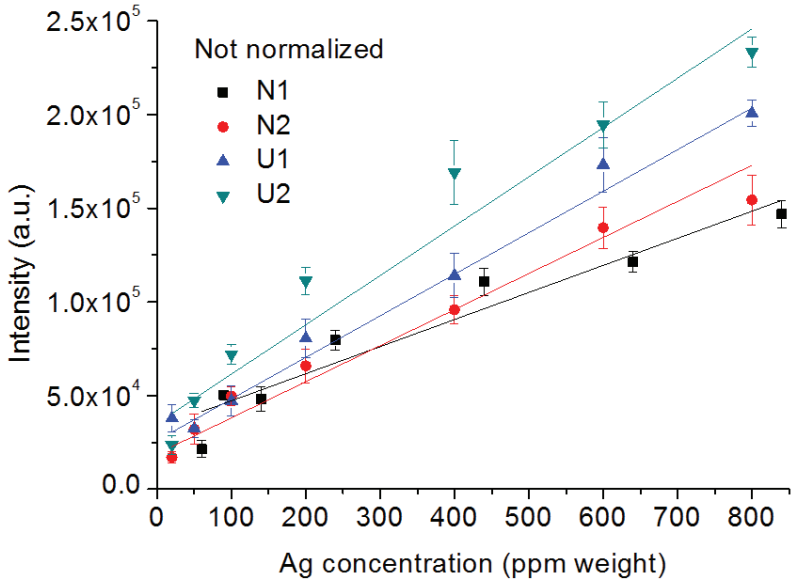

Figure 3.11 Calibration curves of the Ag I 328.1 nm line for the four series of soil samples prepared in pellet without normalization.

Table 3-3 Fitting parameters extracted from the calibration curves presented in Fig. 3.11.

Soils	R^2	LOD (ppm)	LOQ (ppm)	a	b
N1	0.9016	35.6	235.2	32773	144.59
N2	0.9495	21.7	137.6	18885	192.61
U1	0.9898	37.2	95.7	26035	221.82
U2	0.9479	23.2	182.4	35148	263.31
Mean	0.9472	29.4	162.7	28210	205.58
RSD (%)	3.8	27.5	36.8	25.9	24.3

The calibration curves established with samples prepared in thin film are shown in

Fig. 3.12, and the parameters extracted from the linear regression of the data are shown in Table 3-4. A clear reduction of matrix effect is observed, since the slopes of the calibration curves become closer than in the case of pellet samples. A RSD of the slopes b of 9.0% can be calculated which is much smaller than in the case of pellet samples (24.3%). The RSD of the intercepts a is also reduced from 25.9% to 18.0%. However, the correlation of the data remains still quite bad, with similar low R^2 values, which may in addition to the fluctuations already mentioned above for the pellets samples, due to the fluctuations in the preparation of the thin films.

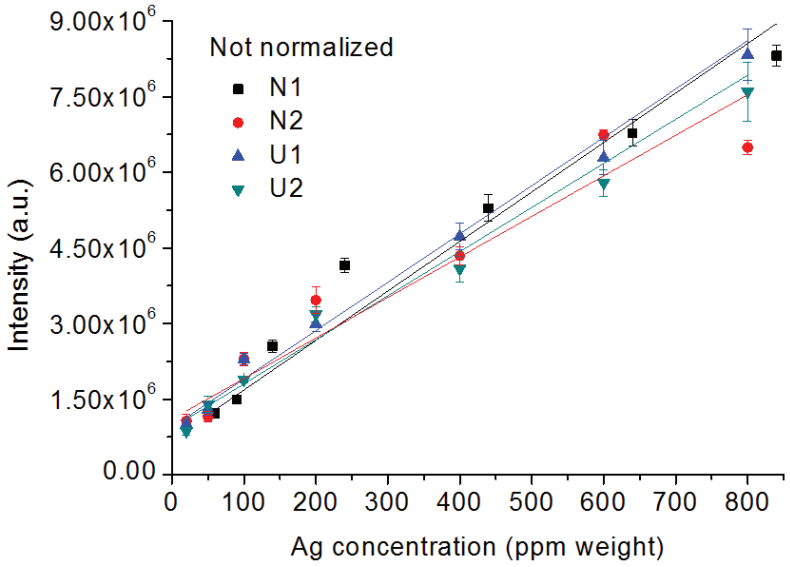

Figure 3.12 Calibration curves of the Ag I 328.1 nm line for the four series of soil samples prepared in thin film without normalization.

Table 3-4 Fitting parameters extracted from the calibration curves presented Fig. 3.12.

Soils	R^2	LOD (ppm)	LOQ (ppm)	a	b
N1	0.9479	4.5	161.1	703353	9811
N2	0.9272	19.5	230.4	1106700	8038
U1	0.9672	9.9	69.6	946937	9576
U2	0.9496	11.4	98.5	930997	8741
Mean	0.9479	11.3	139.9	921996	9041
RSD (%)	1.7	54.8	51.0	18.0	9.0

Calibration curves with the Ag I 328.1 nm line with normalization

We further observe the effect of matrix effect reduction with spectrum intensity normalization with an internal reference, yttrium for instance. In general, an atomic analyte line is better normalized by an atomic line. However, in the case of the spectra of soils, several strong atomic yttrium lines are severely affected by interferences. A check in the spectra shows that several Y I lines around 410 nm are less affected by interference and seem suitable for being used as reference lines for normalization, as shown in Fig. 3.13.

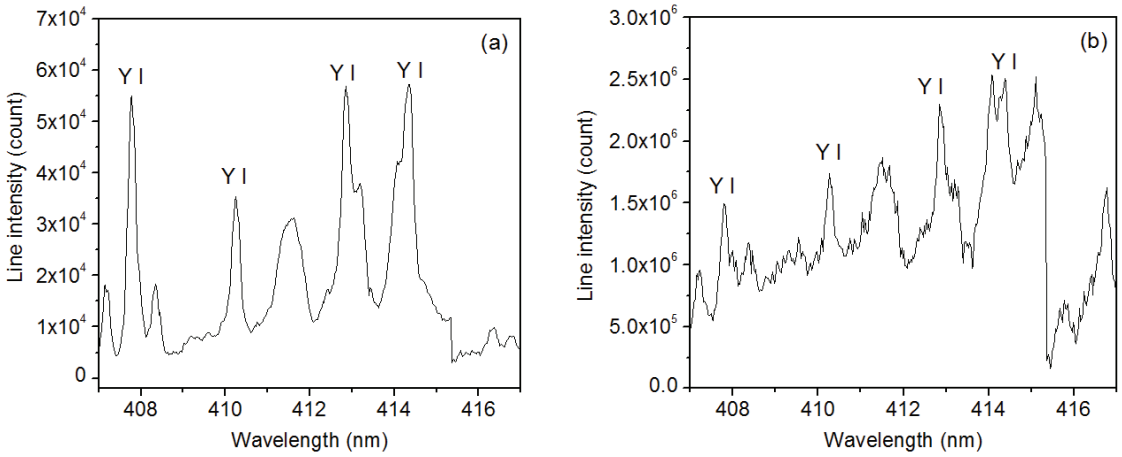

Figure 3.13 Detailed spectrum of the soil sample N1 around 410 nm: a) prepared in pellet, b) prepared in film on aluminum target.

The calibration curves established with the Ag I 328.1 nm line normalized with the Y I 410.2 nm line for samples prepared in pellet are shown in Fig. 3.14. The parameters extracted from the linear regression of the data are shown in Table 3-5. We can see that compared with the data shown in Table 3-3 (pellet samples without normalization), there is a slight reduction of the RSD of the calibration curve slopes, from 24.3% to 19.9%, which indicates a reduction of the matrix effect. However, the improvement remains quite limited, and there is no improvement of R^2 with this spectrum normalization.

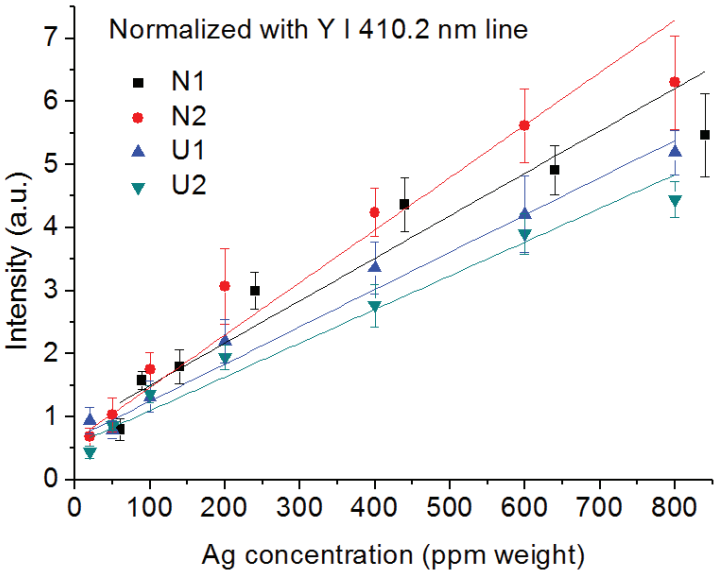

Figure 3.14 Calibration curves of the Ag I 328.1 nm line for the four series of soil samples prepared in pellet with normalization with the Y I 410.2 nm line.

Table 3-5 Fitting parameters extracted from the calibration curves presented in Fig. 3.14.

Soils	R^2	LOD (ppm)	LOQ (ppm)	a	b
N1	0.8995	35.2	241.8	0.8204	0.0067
N2	0.9619	22.6	168.0	0.6310	0.0083
U1	0.9728	42.9	108.0	0.6510	0.0059
U2	0.9467	22.5	133.9	0.5598	0.0053
Mean	0.9452	30.8	162.9	0.6655	0.0065
RSD (%)	3.4	32.6	35.6	16.6	19.9

The calibration curves established with the Ag I 328.1 nm line normalized with the Y I 410.2 nm line for samples prepared in film on aluminum target are shown in Fig. 3.15. The parameters extracted from the linear regression of the data are shown in Table 3-6. Comparing to the results shown in Fig. 3.12 and the data shown in Table 3-4 (film samples without normalization), we can see that the normalization procedure introduces more dispersions in the slopes of the calibration curves. Such results can be explained by the fact that the used internal reference Y I 410.2 nm line is a very week line with respect to the spectrum background and the noise as shown in Fig. 3.13 (b). The use of such line cannot be helpful to improve the analytical performance of the spectroscopic data.

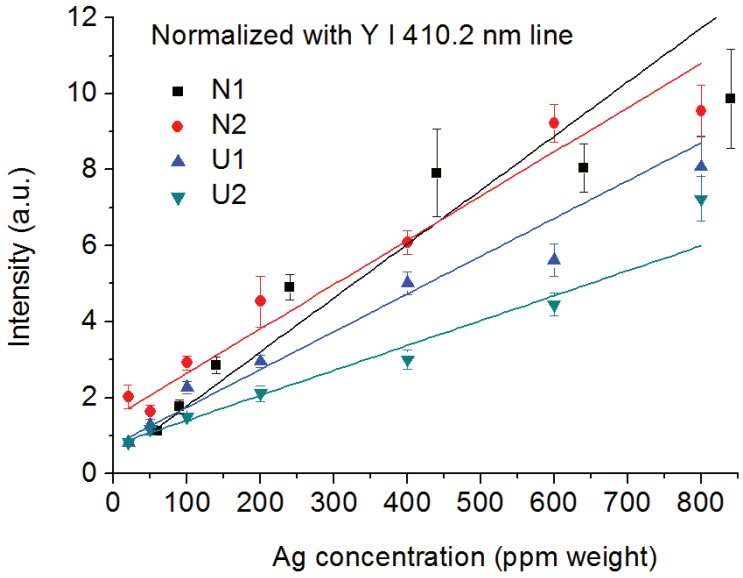

Figure 3.15 Calibration curves of the Ag I 328.1 nm line for the four series of soil samples prepared in film with normalization with the Y I 410.2 nm line.

Table 3-6 Fitting parameters extracted from the calibration curves presented in Fig. 3.15.

Soils	R^2	LOD (ppm)	LOQ (ppm)	a	b
N1	0.9024	6.9	248.6	0.3629	0.0142
N2	0.9549	34.2	168.7	1.4845	0.0116
U1	0.9406	9.4	135.4	0.7557	0.0099
U2	0.9669	12.5	169.3	0.7500	0.0065
Mean	0.9412	15.7	180.5	0.8382	0.0105
RSD (%)	3.0	79.4	26.6	55.9	30.6

An ionic line of yttrium, Y II 360.1 nm line, is then used as the internal reference line, since as shown in Fig. 3.16, this line has a good signal-to-noise ratio and with relatively less interference. Note that the Y I 362.1 nm line is severely affected by the Fe I 361.9 nm line, which can hardly be used for spectrum normalization.

The calibration curves established with the Ag I 328.1 nm line normalized with the Y II 360.1 nm line for samples prepared in pellet are shown in Fig. 3.17. The parameters extracted from the linear regression of the data are shown in Table 3-7. Comparing to the data shown in Table 3-3 (pellet samples without normalization), we can see a great reduction the RSD of the slopes *b*, which indicates a great reduction of the matrix effect.

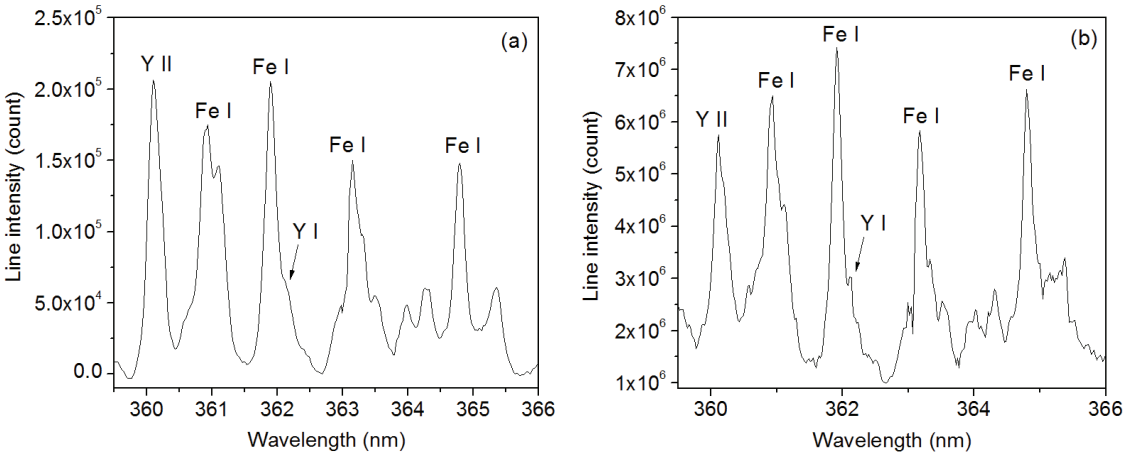

Figure 3.16 Detailed spectrum of the soil sample N1 around 360 nm: a) prepared in pellet, b) prepared in film on aluminum target.

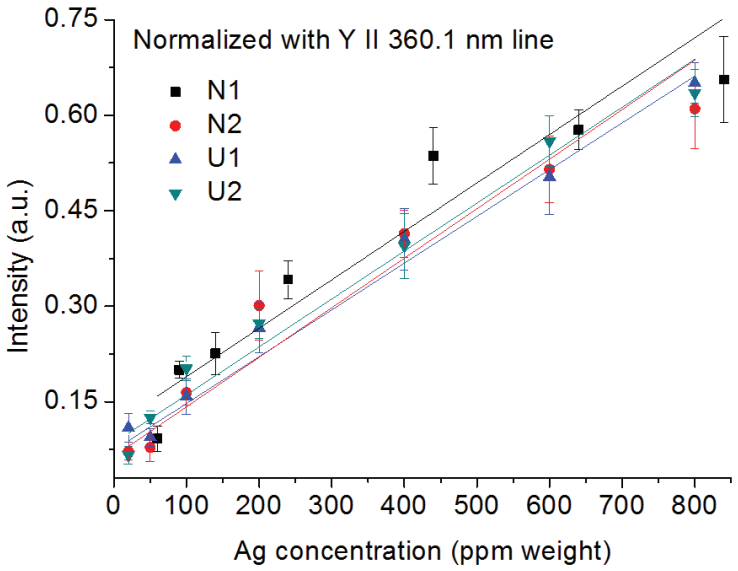

Figure 3.17 Calibration curves of the Ag I 328.1 nm line for the four series of soil samples prepared in pellet and normalized with Y II 360.1 nm line.

Table 3-7 Fitting parameters extracted from the calibration curves presented Fig. 3.17.

Soils	R^2	LOD (ppm)	LOQ (ppm)	a	b (10^{-4})
N1	0.9038	34.0	248.5	0.1131	7.61
N2	0.9537	24.2	176.3	0.0641	7.78
U1	0.9834	37.4	97.5	0.0738	7.35
U2	0.9494	23.5	133.3	0.0854	7.53
Mean	0.9476	29.8	163.9	0.0841	7.57
RSD (%)	3.5	23.5	39.6	25.2	2.4

The calibration curves established with the Ag I 328.1 nm line normalized with the Y II 360.1 nm line for samples prepared in film on aluminum target are shown in Fig. 3.18. The parameters extracted from the linear regression of the data are shown in Table 3-7. Comparing to the data shown in Table 3-4 (film samples without normalization), we can see that globally the RSD of the calibration curve slopes over the 4 soil samples is not decreased with the normalization with the Y II 360.1 nm line, however, if we exclude the N1 soil sample which has a quite singular behavior, we get a RSD of the calibration curve slopes for the rest of 3 samples of 3.6% which is smaller than the RSD of the slopes of the calibration curves obtained in Table 3-4.

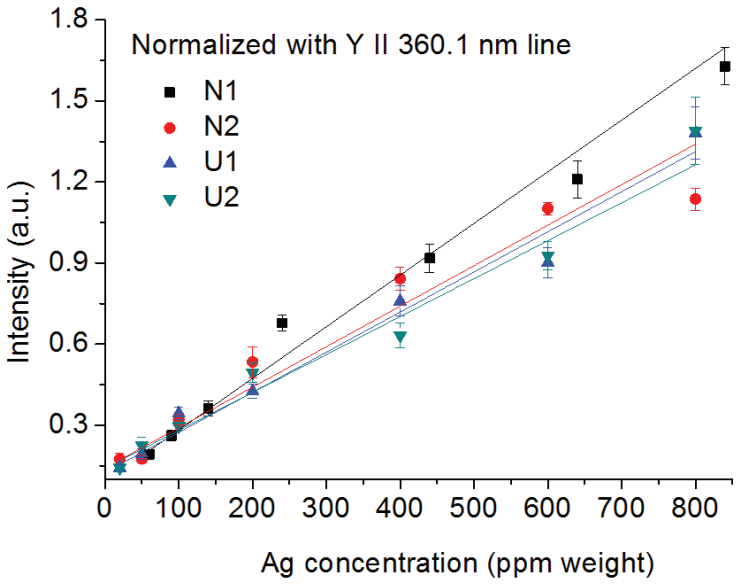

Figure 3.18 Calibration curves of the Ag I 328.1 nm line for the four series of soil samples prepared in thin film and normalized with Y II 360.1 nm line.

Table 3-8 Fitting parameters extracted from the calibration curves presented Fig. 3.18.

Soils	R^2	LOD (ppm)	LOQ (ppm)	a	b (10^{-3})
N1	0.9700	8.0	104.8	0.0914	1.91
N2	0.9648	19.4	194.1	0.1412	1.50
U1	0.9634	8.7	123.0	0.1253	1.48
U2	0.9626	12.0	131.7	0.1407	1.40
Mean	0.9652	12.0	138.4	0.1247	1.57
RSD (%)	0.3	43.4	28.0	18.7	14.6 (3.6*)

* calculated without N1 sample.

From the calibration results discussed above, we conclude that the surface-assisted method could clearly reduce the matrix effect for soil powder analysis compared to the pellet sample preparation method. However, the effect of spectrum normalization with the internal reference element of Y appears quite complex to explain. We mention that there is also no obvious improvement of spectrum normalization with the internal reference element from the ambient gas. The major difficulty to apply spectrum normalization with an internal reference is the choice of a proper reference line. For such complex samples as soils, spectral interferences represent a major challenge for a good normalization. A spectrometer with higher spectral resolution could be helpful in this case. On the other hand, it should be noted that the matrix effect has not been completely eliminated. There is still a RSD of the calibration slopes of 9.0%, which may be representative of the residual matrix effects among the 4 tested soils with the surface-assisted method. For the future works, such residual matrix effects are expected to be overcome with the help of chemometric methods [149] for data calibration and prediction processes, to fully use the complex chemical information from the LIBS spectra of soils.

3.6 Resume

In this chapter, we have developed and evaluated a method of powders analysis with surface-assisted LIBS. We first applied this method on a cellulose powder of 20 µm typical particle size. The powder was spiked with TiO_2 nanoparticles for Ti concentrations ranging from 25 ppm to 5000 ppm. The parameters of figures-of-merit extracted from the calibration graphs show LODs in the range of several ppm weight, which are comparable with the LODs in LIBS analysis of the corresponding pellet samples. Moreover, the correlation of the experimental data to the regression model is greatly improved by spectrum normalization with a properly chosen reference line. Correspondingly, the LOQs also decrease and reach, for optimized spectrum normalizations, the range of 200 ppm weight. We especially demonstrate that the best reference lines for spectrum normalization are not necessary belonging to an internal reference element coming from the sample matrix as recommended by usual

considerations in spectrochemical analysis. Indeed, an element contributed by the ambient gas can also provide suitable reference lines. The additional condition that should be taken into account in particular for an inhomogeneous emission source like laser-induced plasma, is that the population of such element should spatially overlap the elements for which the emission needs to be normalized in the ablation plume.

In the second step, we focused on the matrix effect in the determination of Ti by preparing another series of samples with an alumina powder of average particle size ≤ 10 μm, spiked with TiO_2 nanoparticles. The results obtained with surface-assisted thin film LIBS analysis were then compared to those obtained with LIBS analysis of the corresponding pellets. We show that the important advantage of the surface-assisted LIBS method with respect to the classical pellet method is the efficient reduction of the matrix effect, at least for the two tested kinds of powders, cellulose and alumina powders, which represent very different kinds of organic and mineral powders. A universal calibration curve could be established for elemental analysis in these two matrices, while the comparative measurements with corresponding pellets show a clear matrix effect as we can expect.

Finally, we applied the surface-assisted LIBS method on the analysis of soils as real powder samples. Four different types of soils were tested in the experiment to make an assessment of the method. The preliminary results show clearly the efficiency of the surface-assisted method to reduce the matrix effect for soil powder analysis. The calibration curves of Ag I 328.1 nm line for the four soils prepared in thin films are much closer to each other than for those samples prepared in pellets. The RSD of the slopes of the calibration curves is significantly reduced from 24.3% to 9.0% by using the surface-assisted LIBS method. The effect of spectrum normalization with an internal reference element of Y appears more complex to explain. The major difficulty to apply spectrum normalization with an internal reference is the choice of a proper reference line. For such complex samples as soils, spectral interferences represent a major challenge for a good normalization.

Further studies are still needed before the developed method could be applied in real-

case analyses:

i) about the effects of particle size in powders and the influence of the simultaneous presence of a large number of elements, as it is the case for soils;

ii) about the combination with the chemometric method for data processing, to overcome the residual matrix effect existing for the surface-assisted LIBS analysis.

Chapter 4. Classification of wines according to their production regions with surface-assisted laser-induced breakdown spectroscopy

In this chapter, we will apply the surface-assisted LIBS method for the elemental analysis in wines in order to classify different wines according to their production regions. Although fingerprinting wines based on their elemental profile [150,151] is rather a classical procedure demonstrated for longtime and using various established analytical techniques [152-161], the use of LIBS for such purpose first requires to significantly increase the sensibility of the technique for liquid analysis. In such way that the emission lines of trace elements, which are often discriminative for wines from different production regions, can be detected with good signal-to-noise ratios. One of the key points in this work is thus the use LIBS with the surface-assisted method for sample preparation, where a wine sample is pre-concentrated and transformed into a thin layer of soft material on the surface of a solid target by low temperature evaporation. The high sensitivity of this method can lead to the detection of at least 22 metal and nonmetal elements in a typical wine including majors, minors and traces. Other key point in this work is the LIBS spectrum treatment, with which complex information contained in the LIBS spectra of wines can be efficiently used for successive fingerprinting the tested wines. In this work, an ensemble of 29 bottles of French wines from five production regions have been analyzed together with a wine from California, considered as an outlier. Two classification models based on the principal component analysis (PCA) and random forest (RF) have been used for the classification. We will in this chapter present the measurement method and the obtained results, then for the data treatment procedures, we will especially discuss the choice of input variables for the classification models, the effect of spectrum

normalization with an internal reference, the influence of matrix effects on classification, and the optimization for the developed classification models.

4.1 Motivation

Fingerprinting wines with their elemental composition and the consequent classification according to their production places often correspond to important economic (product authenticity, fraud detection) as well as food security issues (pollutions, accidents in viticultural practice and/or in winemaking procedure). Such classification is based on the fact that the elemental profile of a wine is determined by endogenous factors (soil, grape variety, climate) as well as exogenous influences (cultivation practice, winemaking process, pollutions) [150]. A proper practice in elemental analysis of wines allows observing either the combined effects of the endogenous and the exogenous factors in the elemental profile of a wine, or the specific impacts of the separated influences of different factors [151]. It appears that up to now, the most interests and published works on wine classification are dedicated to those according to the productions regions [152,153]. This is not a surprise considering the endogenous sources as the most influencing factor in the determination of the elemental profile of a wine, and taking into account the most demanding analytical applications in wine production and commercialization.

Efficient classification of wines can be provided by most established analytical techniques, among which we can find atomic emission spectrometry (AES) and atomic absorption spectrometry (AAS) [154,155], especially graphite furnace AAS (GFAAS), hydride generation AAS (HGAAS) [156], or flame AAS (FAAS) [157], inductively coupled plasma optical emission spectrometry (ICP-OES) [152,158] or mass spectrometry (ICP-MS) [151,152,159-161]. The pretreatment procedures associated to these analytical techniques can be quite complex, time-consuming and need substantial quantity of chemical reagents and solvents [162,163]. Heavy sample pretreatment procedures are needed especially for wines because of their complex organic matrix. There is therefore an obvious interest to develop a method of elemental determination for wines, which allows an easier, quicker and environmentally friendly access to the concentrations of

major, minor and trace elements in a wine. For classification purpose, such method becomes crucial when sorting of a large amount of wines is required for important applications, such as food safety control, product traceability or brand authentication.

LIBS technique has been applied to classifications of a variety of materials such as geological minerals [17,164,165], polymeric materials and especially explosives [166-170], biological materials [171,172] and so on. However, the sensitivity of LIBS for elemental detection in liquid samples such as wines is usually limited by the low efficiency of direct laser ablation of liquids, either on the surface or inside of a liquid, which leads to low temperature and short lifetime of the induced plasma [173]. The reported LOD for metallic elements in a liquid matrix is often much higher than the ppm (or mg/L) level [174,175]. Such sensitivity does not allow minor and trace elements in wines to be detected, while some detected major elements would not be enough characteristic to provide efficient fingerprints of wines. In previous works of our group, the surface-assisted LIBS technique has been used for efficient analysis of thin coating layer of viscous liquids, such as lubricating oils [59-61], creams [62], and more recently wines [176]. Such method is quite similar to the dried-liquid layer method introduced with the name of surface-enhanced LIBS [177-181]. For wines more specifically, pre-concentration is possible and easily feasible during the thin coating layer preparation with low temperature evaporation. The conjugated effect of efficient solid target ablation and pre-concentration in the dried thin layer of wine residue led to sensitive detection of metals in wines with especially LODs of respectively 0.1 ppm and 1.5 ppm for Ti and Fe [176]. A recent work has also reported a different wine sample preparation method by using an added collagen gel combining with low temperature heating and ventilation to obtain a dried solid layer of wine residue of about 0.35 mm thickness for laser ablation. Subsequent LIBS measurements together with an artificial neural network (ANN) model allowed then a successful classification of red wines according to their production regions [182]. The sensibility associated to such sample preparation method is however quite low, limiting the detection to only some major elements in a wine.

The purpose of the works presented in this chapter is to use the surface-assisted LIBS

technique, with its ppm and sub-ppm LODs, for the classification of a variety of wines of controlled designation of origin from different wine production regions in France, with their elemental profiles including major, minor and trace elements. Two classification models have been developed for the classification. The first one is based on the principal component analysis (PCA), and the second one on the random forest (RF). After a brief presentation of the sample preparation procedure and the measurement protocol, the results from a PCA classification will be first presented. The optimization of the RF algorithm will then be presented together with the obtained classification results. We will especially discuss the choice of input variables for the classification models, the effect of spectrum normalization with an internal reference, the influence of matrix effects on classification, and the optimization for the developed classification models.

4.2 Sample preparation and measurement protocol

4.2.1 Wine samples and their production sites

An ensemble of 30 bottles of French wines bought from supermarkets was analyzed in this work, including 14 red wines and 16 white wines. Thirteen red wines were from 4 production regions in France: 3 from Beaujolais, 4 from Bordeaux, 3 from Bourgogne and 3 from Languedoc. A red wine produced in California in USA was tested as outlier. The white wines were from 4 regions in France, 7 from Alsace, 3 from Bordeaux, 4 from Bourgogne, 1 from Languedoc. And 1 Rosé wine from Languedoc was considered as white wine for simplicity. The detailed information about the wine samples and their number used in this work are shown in Table 4-1. Note that there were two bottles of a same wine from Alsace (n°25 and n°26) that were used to test the repeatability of the LIBS measurements. All the French wines were of controlled designation of origin to guarantee their production sites. A map of wine production regions in France is shown in Fig. 4.1, where we can see the five production regions involved in this work.

Table 4-1 Wine samples tested in this work and their detailed information.

Production Region	Type of wine	Sample number	Commercial name	Controlled designation of origin
California (USA)	Red	1	De Loach Heritage Reserve Zinfandel California Rouge 2014	California
Beaujolais	Red	2	Domaine de L'Herminette Morgon Rouge 2014	Morgon
	Red	3	Domaine du Grand Foudre Côte de Brouilly Rouge 2014	Côte de Brouilly
	Red	4	Bouchard Père et Fils Beaujolais Villages Nouveau Rouge 2015	Beaujolais-Villages
Bordeaux	Red	5	Les Allées de Cantemerle Haut-Médoc Rouge 2012	Haut-Médoc
	Red	6	Château Reysson Haut-Médoc Rouge 2011	Haut-Médoc
	Red	7	Château Lusseau Saint-Emilion Grand Cru Rouge 2004	Saint-Emilion
	Red	8	Château de Chantegrive Graves Rouge 2013	Graves
	White	9	Château du Cros Cuvée Prélude Gourmand Loupiac Blanc 2011	Loupiac
	White	10	Château de Chantegrive Caroline Graves Blanc 2013	Graves
	White	11	Château La Grave Sainte Croix du Mont Cuvée Les Bessanes 2012	Saint Corix du Mont
Bourgogne	Red	12	Domaine Levert Barault Mercurey 1er Cru Rouge 2013	Mercurey
	Red	13	Domaine Gachot Monot Côte de Nuits Villages Rouge 2013	Côtes de Nuits Villages
	Red	14	Domaine Paire Macon-Azé Rouge 2012	Mâcon
	White	15	Domaine R. Thibert Lardet Pouilly Vinzelles Blanc 2014	Pouilly-Vinzelles
	White	16	Domaine du Mont Saint Gilbert Mâcon Villages Blanc 2013	Mâcon Village
	White	17	Saint-Véran Bouchard Père et Fils Blanc 2013	Saint Véran
	White	18	Mâcon-Villages Domaine du Mont Saint Gilbert Blanc 2014	Mâcon Village
Languedoc	Red	19	Château La Voulte Gasparets Corbières Rouge 2013	Corbières
	Red	20	Château de Saint Louis Corbières Cuvée Prestige Rouge 2013	Corbières
	Red	21	Domaine du Chapitre Délice IGP Hérault Rouge 2012	Pays de l'Hérault
	Rosé	22	Domaine Valgalier Le Cru Qui Tue IGP Hérault Rosé 2013	Pays de l'Hérault
	White	23	Domaine de la Rencontre IGP Herault Blanc 2013	Pays de l'Hérault

Alsace	White	24	Rittimann Riesling Réserve Particulière Blanc 2014	Alsace
	White	25	Domaine Joseph Cattin Alsace Pinot Gris Blanc 2014	Alsace
	White	26	Domaine Joseph Cattin Alsace Pinot Gris Blanc 2014	Alsace
	White	27	Wolfberger Sylvaner Blanc 2014	Alsace
	White	28	Domaine F Engel Riesling Praelatenberg Grand Cru blanc 2011	Alsace
	White	29	Domaine Hurst Alsace Pinot Blanc 2014	Alsace
	White	30	Tradition Dopff Muscat Sec Blanc 2014	Alsace

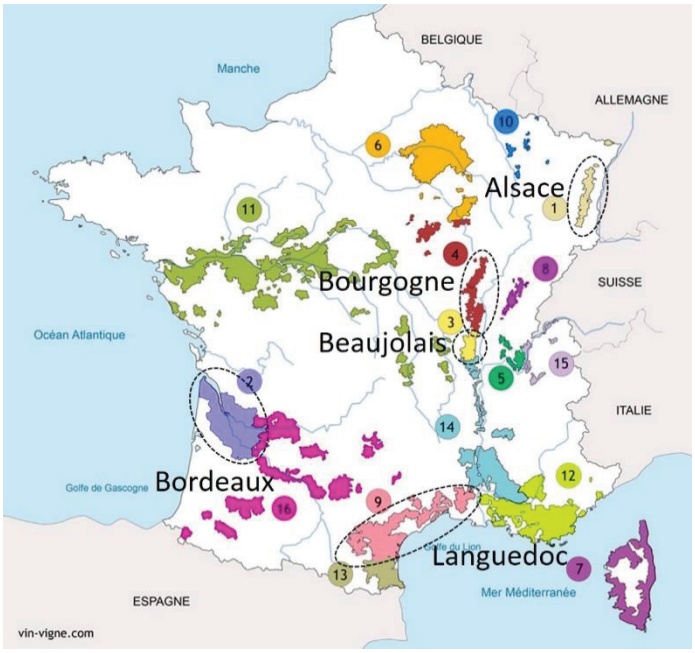

Figure 4.1 Map of wine production regions in France with the five sites considered in this work.

4.2.2 Sample preparation and measurement protocol

The bottles of wine were opened at the room temperature and extracted with a syringe in order to avoid any contamination. Yttrium (Y) was introduced as an internal reference, since we did not detect any emission line from this element in the LIBS spectra of the wine samples and Y solution is a usual standard solution. Each wine sample was spiked with 1 mL standard solution of Y (yttrium standard in 2 % nitric acid solution purchased from Sigma-Aldrich at a concentration of 1000 mg/L) to a total volume of 40 mL to get spiked wine samples with 25 mg/L of Y. Two mL of the prepared liquid was picked with a pipette and dropped on the polished and cleaned plate surface of a pure aluminum target

(Techlab, Al 99.99%). The liquid was retained stable on the target surface by the surface tension, as shown in Fig. 4.2 (picture of the left side). A prior adjustment of the target ensured the horizontality of its surface. The sample was then put into a laboratory-made oven with an electrical hot plate for a drying procedure by gentle evaporation. This procedure consisted of a first phase of relatively strong heating of 10 minutes in order to remove the most of liquid without any boiling, followed by a second phase of weaker 5 minutes heating to get a better fixation of the obtained coating layer on the target surface. The sample was then left for cooling down for about 5 minutes before being moved into the laser ablation stage. By applying this procedure, we got the residue from a liquid wine in the form of a uniform and semi-transparent thin layer on the aluminum target, as shown in Fig. 4.2 (picture of the right side). In the picture, we also can see the traces left by laser ablations on the target surface. We remark also a zone of dark color appears in the periphery of the target. This zone corresponds to an area of thicker wine residue deposition formed during the preparation of the layer, and it was not used in our experiment for LIBS measurements.

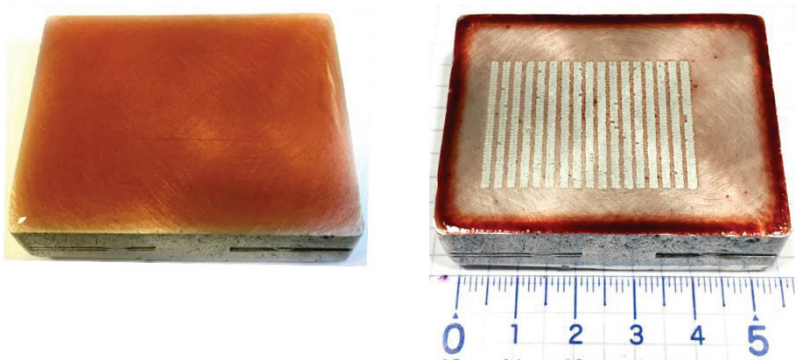

Figure 4.2 Photograph of liquid wine sample dropped on the surface of an aluminum target (left) and the resulted wine residue as a thin layer on the aluminum target after the heating process (right). Only the uniform and semi-transparent middle part of the target was used for laser ablation.

The experimental setup is similar to that in Section 2.2. In this work, we used the infrared (1064 nm) laser pulses for ablation. The laser pulse energy was fixed at 100 mJ. The laser beam spot on the target surface was about 300 μm in diameter, which resulted in a fluence of 140 J/cm^2. A microscope glass plate placed under the focusing lens was used to protect the lens from ejected debris. The spectral emission detection system was

the same as that in Fig. 2.1(b). The entrance of the fiber was centered at the symmetrical axis of the plasma and shifted by 2.0 mm from the target surface, such distance was optimized to capture the emission from the deposited wine residue on the aluminum target, which is located around the propagation front of the plasma. Such a shift was also sufficient to get away from strong emissions from Al and its oxide AlO and other molecular species (C_2 and CN) often observed in the LIBS spectrum of an organic sample, as well as the continuum emission. The detection window was set with a delay of 1.5 μs and a width of 3.0 μs after the impact of the laser pulse on the sample. We mention that with the above described detection arrangement, large bandwidth emissions, including molecular and continuum emissions from the plasma, appeared very weak with respect to the emission lines from the metallic elements contained in the wine, which is benefic for their detection.

During the experiment, each individual spectrum was an accumulation of 80 single-shot ablations performed in a matrix of 2 × 40 craters on the target surface, with a center-to-center distance of 600 μm between the neighboring craters (craters visible in Fig. 4.2). Fifteen replicate spectra were acquired for each sample. Therefore, we produced 450 spectra from the 30 bottles of wine for statistical analysis.

4.3 Step by step classifications with principal component analysis

In this section, the classification results of the tested wines with PCA analysis are presented in several steps. The purpose is not only to show the results as the final achievement, but also to show the procedure and the significance of the method used in its details. Such approach would be more interesting in this work intended to the development of a method because, as we will see, some physical and chemical properties of wines (not only their elemental profile) can have important influence for their characterization and therefore for their classification. The PCA was realized using a commercial software (SIMCA-P software, version 14.1, Umetrics, Sweden).

4.3.1 Selection of fingerprint elements and characteristic lines

Typically, in the tested wines, besides the organic elements (C, H, O, N) and Al, 17 metal

and nonmetal elements, including Na, Mg, K, and Ca as majors, Li, B, Si, P, Ti, Mn, Fe, Cu, Zn, Rb, Sr, Ba and Pb as minors or traces were detected with sufficient signal-to-noise ratios [176]. C is contributed by organic materials in wine, and H, O, N and Al can be detected without wine residue layer due to the aluminum target and the ambient air. Therefore, they are not specific to an analyzed wine. A proper selection of elements among those detected in wines and further determination of their characteristic lines to be taken into account as input variables in the PCA data analysis are very important for an efficient classification. The purpose was to select a list of elements and associated lines that were discriminative for the tested wines with respect to their production sites. The organic elements C, H, O and N were obviously excluded from this list since they were related to the organic matrix of wines and the ambient gas. We further excluded Al because the observed emission intensity was dominated by the contribution from the aluminum plate.

In addition, as we discussed above, among minor and trace elements detected in a wine, a part of them may be more related to the grape cultivation practice and the winemaking procedure. This is actually the case of Pb and Cu. Pb as a trace element in wine is predominately contributed by fungicide treatments, containers or atmosphere pollutions (for example, vineyards located near roads subjected to heavy traffics). Only a small amount of this element can be originated from the vineyard soil [151,183]. Cu can be mainly introduced by the fungicidal treatment (Bordeaux mixture) or by the wine-making process [183]. Copper sulfate in particular, is used to prevent from parasitic infection during grape growth. Fe can also be potentially introduced in a wine during the winemaking process, however it is observed to be a good indicator for distinguishing between red and white wines [150,183,184]. Finally, 15 elements (Li, B, Na, Mg, Si, P, K, Ca, Ti, Mn, Fe, Zn, Rb, Sr and Ba) were selected as fingerprint elements for classification of the tested wines.

Characteristic lines were chosen for these elements based on the criteria of absence of interference and having a sufficiently good signal-to-noise ratio. A typical LIBS spectrum of a tested wine is shown in Fig. 4.3 with a detailed view on the spectral range

from 248 nm to 256 nm, showing 4 Fe I lines, 2 B I lines, 6 Si I lines and 4 P I lines. We can see that a large number of lines can be identified in the spectrum, which facilitates the selection of characteristic lines. All the selected elements and the corresponding characteristic lines used as input variables in the PCA analysis are shown in Table 4-2. Notice that, for Ca and Mg, one atomic line and one ionic line were selected among the large number of available atomic and ionic lines. Therefore, the intensities of 17 characteristic lines belonging to 15 elements were selected as input variables of the PCA analysis. In this work, the intensity of an emission line was defined as the height of the line with respect to the baseline.

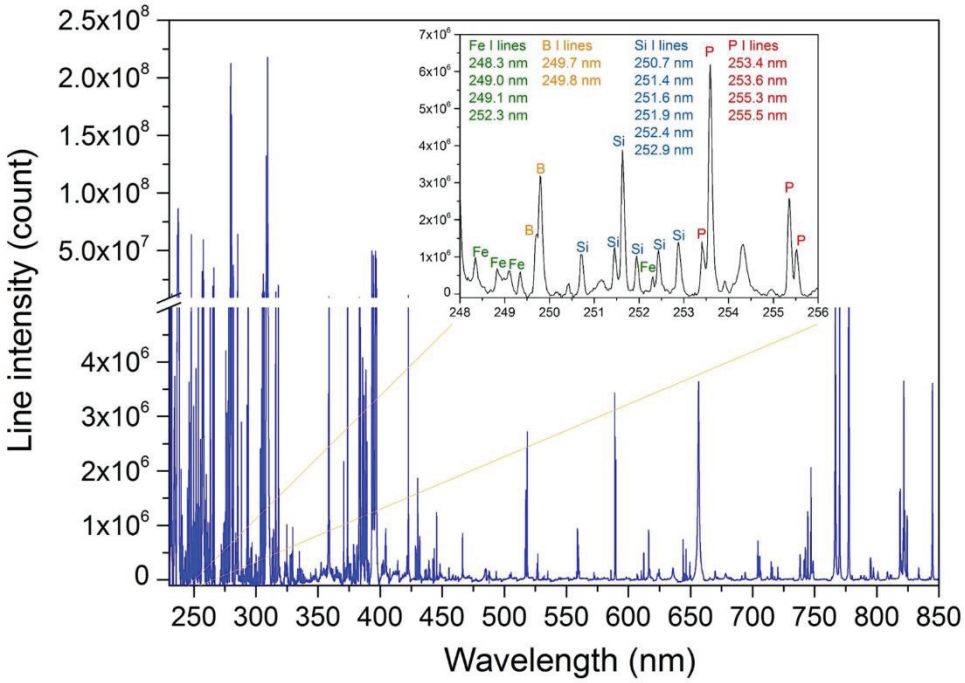

Figure 4.3 A typical spectrum of a wine analyzed in this work with, in the inset, the portion of spectrum corresponding to the spectral range from 248 nm to 256 nm showing 4 Fe I lines, 2 B I lines, 6 Si I lines and 4 P I lines.

Table 4-2 Selected elements and corresponding characteristic lines used as input variables for the PCA analysis.

Element	Li	B	Na	Mg	Si	P	K	Ca	Ti	Mn	Fe	Zn	Rb	Sr	Ba
Atomic line (nm)	670.8	249.8	589.6	518.4	288.2	255.3	766.5	445.5			344.1	334.5	780.0	460.7	
Ionic line (nm)				279.6				317.9	334.9	259.4					455.4

4.3.2 Spectrum normalization with an internal reference

Standard solution of Y is typically used as an internal reference for ICP-OES analysis. It was also chosen in this work for the following reasons:

i) Y is a rare earth element, which is usually not present in wines (taking into account the LOD of the used method);

ii) Y has a quite sensitive response with both Y I and Y II lines within a wide wavelength range from 300 to 600 nm;

iii) A solution of Y can be easily mixed into liquid wines, forming a homogeneous liquid sample.

We first observed the effect of fluctuation reduction of line intensities when the emission intensities were normalized with a Y I or a Y II line. The RSD of atomic lines or ionic lines was calculated for 15 replicate spectra of a given sample. The RSDs are displayed for different elements in Fig. 4.4(a) for atomic lines of Ca, Mg, Sr, Li and in Fig. 4.4(b) for ionic lines of Ca, Mg, Mn, Ti. The atomic Y I 362.1 nm line and the ionic Y II 360.1 nm line were chosen as the internal reference lines, which are both observed with good signal-to-noise ratio (SNR) without significant interference with other emission lines. In order to avoid sample-to-sample variation, the presented RSD values are those averaged over four red wines among the samples (n°3, n°7, n°13 and n°20).

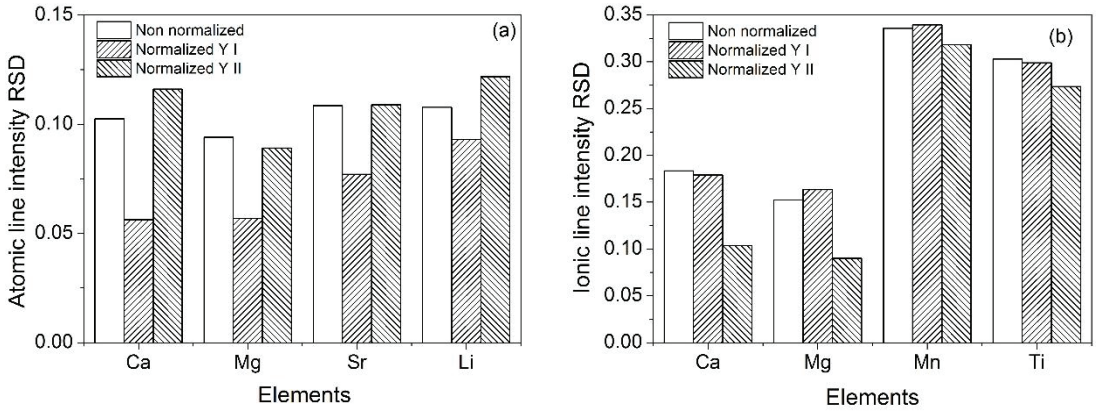

Figure 4.4 RSD of atomic line (a) and ionic line (b) of different elements (Ca, Mg, Sr and Li for atoms and Ca, Mg, Mn and Ti for ions) without normalization, normalized with the Y I 362.1 nm line and the Y II 360.1 nm line.

We can see first in Fig. 4.4 that the atomic lines globally have a smaller fluctuation (~10% without normalization) than the ionic lines (~15% to 30% without normalization). This behavior can be explained by the higher energy of ionic systems which are more sensitive to the fluctuations of plasma parameters such as the temperature. For atomic lines, we can see in Fig. 4.4(a) that the normalization with the Y I line significantly reduces the RSD. Satisfactory values of about 5% and 10% are obtained for majors (Ca and Mg) and traces (Sr and Li), respectively. However, the RSDs increase when normalized with the Y II line. These observations indicate a good correlation between the atomic lines, while the correlation between the atomic lines and the ionic line of the internal reference element is rather bad [185]. The opposite behavior is observed for the ionic lines [Fig. 4.4(b)]. The RSDs of the intensities of the ionic lines are significantly reduced when normalized with the Y II line, while the RSDs remain rather unchanged or become even larger when normalized with the Y I line. We clearly observe here different behaviors between major elements, Ca and Mg with a RSD which can be reduced under 10%, and trace elements Mn and Ti, for which the RSD does not decrease much when normalized with the Y II line and stays at a high level of about 30%. Such a difference may be explained by the low SNRs observed for the emission lines from trace elements.

The results presented in Fig. 4.4 lead to the following evidences: i) the RSDs of atomic lines are always lower than those of ionic lines; ii) to further reduce the RSDs, the atomic lines should be normalized with an atomic line of the internal reference, while the ionic lines should be normalized with an ionic line. This is why we have chosen a list of lines with a majority of atomic lines completed with several ionic lines with significantly higher intensities than the atomic lines of the same elements in the spectral range of our spectrometer.

The raw and normalized intensities of the lines listed in Table 4-2 were thus used as input variables of a PCA analysis of 4 wine samples (n°3, n°7, n°13 and n°20) from 4 different regions. The obtained PCA score plots are shown in Fig. 4.5. We can see a clear improvement in terms of classification by clusters of the tested wines. The dispersion of the PCA scores of a given wine [Fig. 4.5(a)] becomes much more reduced compared to

the dispersion between the clusters corresponding to different wines when the line intensities are normalized respectively with an atomic or an ionic line [Fig. 4.5(b)]. In the following PCA analyses, only the lines intensities respectively normalized with the atomic or the ionic line of Y are used as input variables.

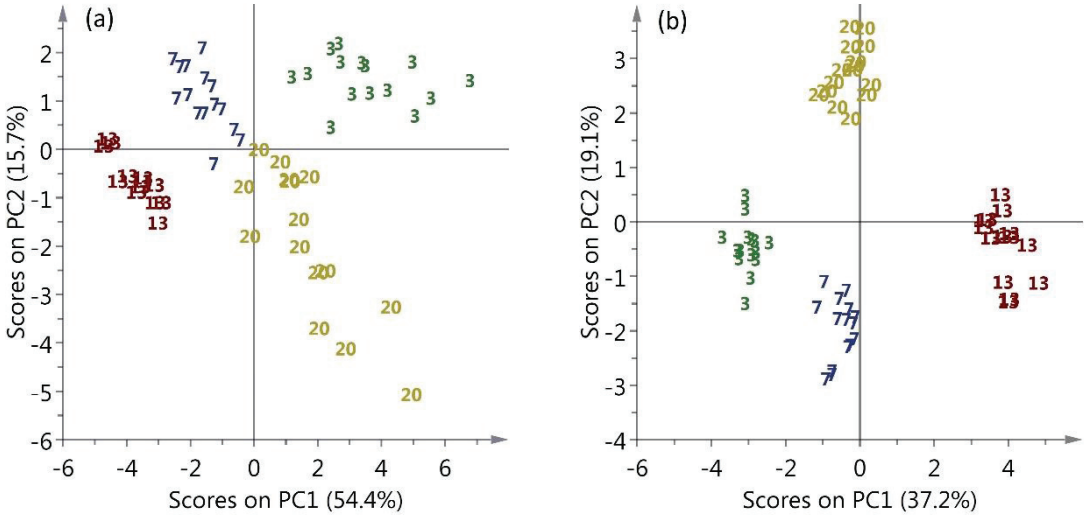

Figure 4.5 PCA score plots of four red wines: (a) performed with raw lines intensities; (b) performed with line intensities normalized with the Y I and Y II lines respectively.

4.3.3 Classification of all the wine samples: influence of the matrix effect

Figure 4.6 shows the PCA scores of all the tested wines obtained using, as input variables, the normalized line intensities of the fingerprint elements as discussed above. We can see that even though a detailed interpretation of the plot remains quite difficult, three separated clusters appear. A cluster for the California wine clearly distinguished from the French wines, appears as the outlier with respect to the tested French wines. With a closer examination on the spectra, we can see that the California wine exhibits much higher intensities for the two lines of Sr I at 460.7 nm and Li I at 670.8 nm than the French wines. Among the French wines, two clusters can be observed. One is situated in the up side of the PCA plot and involves eight white wines [n°9, n°11 (Bordeaux), n°17 (Bourgogne), n°23 (Languedoc), n°25, n°26, n°28 and n°30 (Alsace)]. The other one is situated in the lower part of the PCA plot and containing the rest of white (rosé) wines and all the red wines. There is no straightforward interpretation for these two clusters in terms of the characteristics of the wines (production region, color of the wine). One can

remark that the PCA scores of the samples n°25 and n°26, in fact two bottles of the same wine, are distributed in the same region of the PCA score plot, which indicates the good repeatability of the measurements.

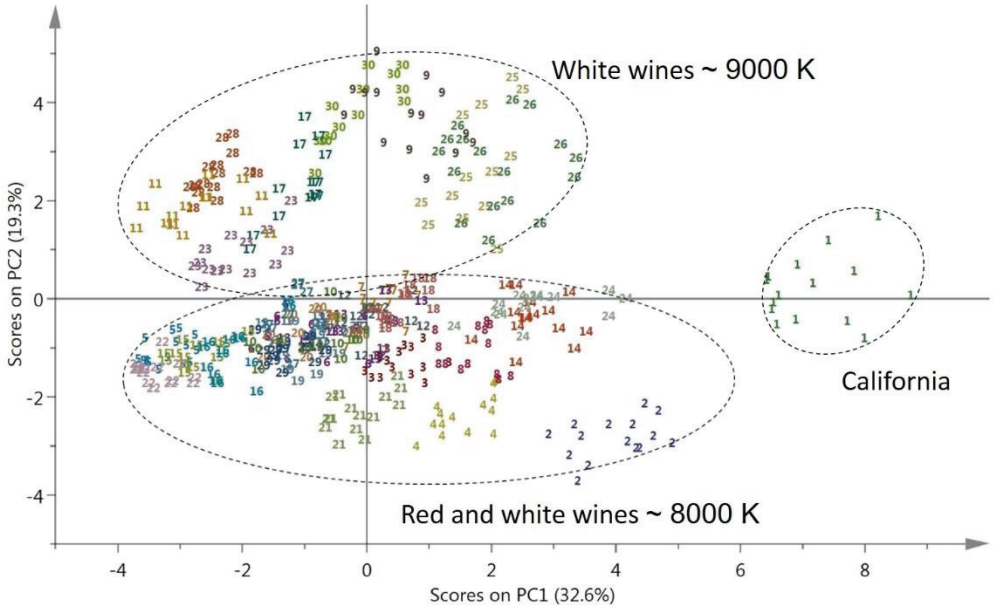

Figure 4.6 PCA score plot of all the wine samples represented by their number in this work (Table 4-1). The indications in temperature are discussed in the next section.

In order to understand hidden parameters leading to the formation of the observed two distinguished clusters for the French wines, we extracted the electron density and the temperature of the plasmas from the recorded spectra. The electron density was extracted by the Stark broadening of the H_α line at 656.3 nm. The temperature was calculated by Saha–Boltzmann plot of the emission lines from a major element in wine, Ca for instance, including Ca I and Ca II lines (Ca I 445.5, 643.9, 646.3, 649.4 nm lines and Ca II 315.9, 317.9 nm lines). There was not any resonant line among the above ones, which reduces the error of temperature determination due to self-absorption. The extracted electron density and temperature are shown in Fig. 4.7.

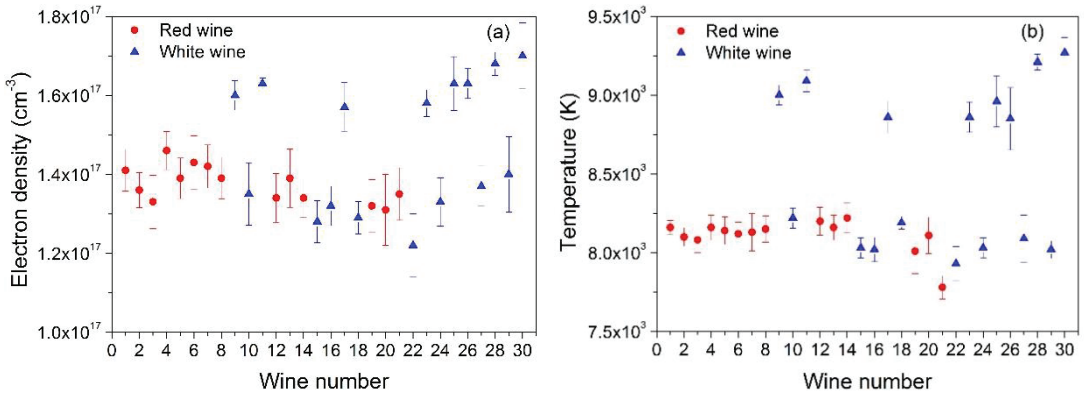

Figure 4.7 Electron density (a) and plasma temperature (b) of all the wine samples as a function of their number in this work (Table 4-1).

In Fig. 4.7, we can see that the measured electron densities and temperatures are distributed around two average values. For the electron density (resp. the temperature), most samples exhibit a value around 1.3×10^{17} cm^{-3} (resp. 8000 K). However eight samples, all white wines, present significantly higher values of around 1.6×10^{17} cm^{-3} for the electron density and 9000 K for the temperature. The differences between the low and the high values for the electron density and the temperature clearly exceed the experimental error bars. Even though the absolute values of the electron density and the electron temperature could be influenced by eventual self-absorption of the used lines, the relative values of these quantities, and thus their difference, remain reliable. A quick check shows that the white wines showing higher values of electron density and temperature are those with sample number of 9, 11, 17, 23, 25, 26, 28 and 30. It is quite remarkable that these white wines exactly correspond to those gathered within the cluster, which is located in the up part of the PCA plot in Fig. 4.6.

An inspection of the obtained wine residues prepared on the aluminum target can also show different visual aspects as shown in Fig. 4.8. Especially we can remark that the for all the white wines corresponding to higher electron densities and temperatures, the films of wine residue appear rather clear and transparent, while for the rest of white wines and all the red wines, the prepared residue films appear less transparent and more dark in color. This observation provides a visual evidence supporting the observed differences in the physical parameters of the plasma. Indeed, the differences in the apparent color or darkness of the prepared wine residues indicate the differences in the physical and

chemical properties of the wines, which can lead to matrix effect in laser ablation as we observed in the experiments.

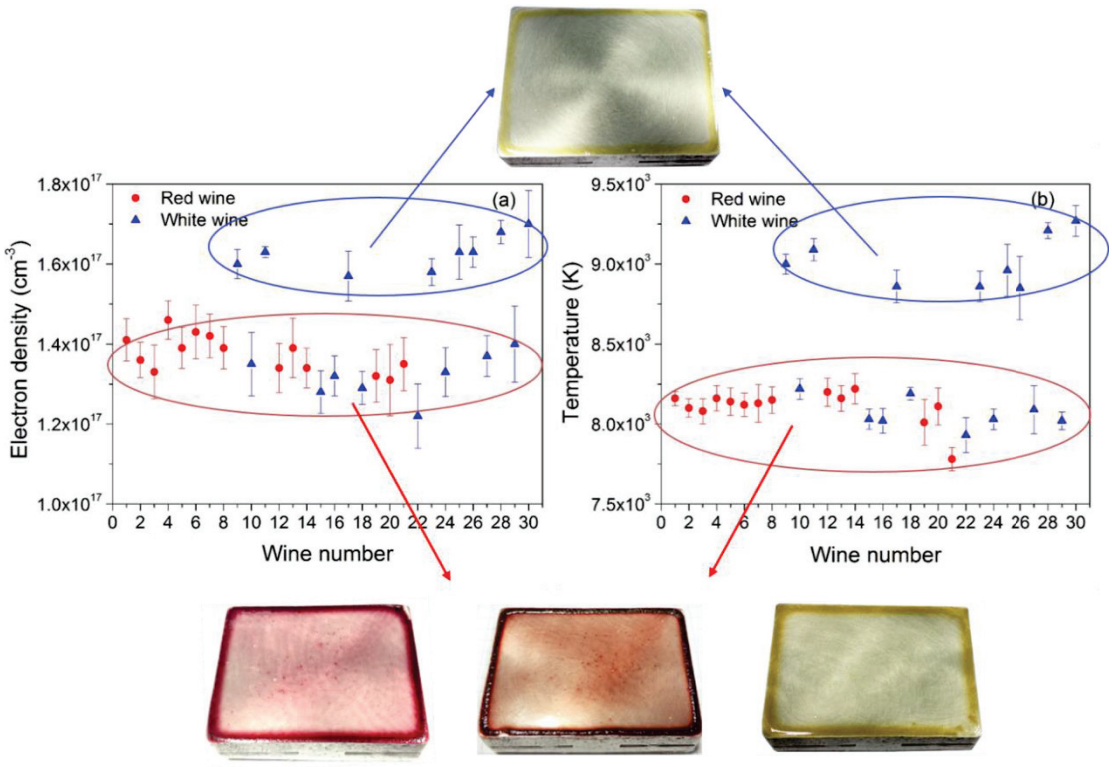

Figure 4.8 Pictures of prepared films of wine residue on the surface of aluminum target and their correspondence to different electron densities and temperatures.

Therefore, the observed correlation between the clusters in the PC diagram and the distinct values of the electron density and temperature shows the physical origin of the classification appearing among the French wines observed in the PCA plot in Fig. 4.6. Apart from the cluster of the California wine, which behaviors as an outlier as expected, the arrangement of the tested French wines in the PCA plot seems being determined by the so-called matrix effect. In other words, under the same experimental condition as it was the case in our work, the generated plasmas exhibit different properties for different wines, such as different electron densities and different temperatures. Such differences could be due to the fact that for different wines, the properties of the obtained wine residue layers on the aluminum target, such as the thickness or the transparency, could be different, which leads to different plasma properties as observed in Fig. 4.7. Before we find a suitable method to overcome completely the matrix effect, it is therefore reasonable to remove those eight "special" white wines in order to go further in the classification.

4.3.4 Separation between the red and the white wines

The PCA score plot of the ensemble of red and white wines showing electron densities of around 1.3×10^{17} cm^{-3} and temperatures of around 8000 K is presented in Fig. 4.9. We can see that apart from the already observed separation of the California wine, the French wines appear being separated into two clusters, the first one corresponding to all the white wines and the second one to all the red wines. Such result indicates that the color of the wines can correspond to significant different characteristics of the related LIBS spectra, which results in the separation of the white wines and the red wines in the PCA score plot. With a close look of the spectra of the tested wines, we can see that the intensity of the Fe I 344.1 nm line is always higher for red wines than for white wines. In fact, white wines and red wines are produced with different wine making procedure. In particular, the contact between the grape juice and the skins after crushing for red wines is longer than for white wines. Therefore, the absorption of trace elements from the skins for red wines is more efficient than for white wines [159] due to the differential uptake of trace elements in the skins and fleshes of the grapes. This difference in the concentration of trace elements in wines leads to the observed separation of white wines and red wines before their respective classifications according to the production sites. This also means that for analysis of white wines, a higher detection sensitivity is required. For example in our previous work [176], we have shown that the LOD for Fe detection is 1.5 ppm with the used surface-assisted sample preparation method. In this work, the Fe I 344.1 nm could be detected with good SNR in the spectra of all the red wines, while it could only be detected in a part of white wines. Our observation corresponds well to the typical Fe concentrations reported in the literature of 1.7 - 8.4 ppm for red wines and 0.8 - 2.4 ppm for white wines [184].

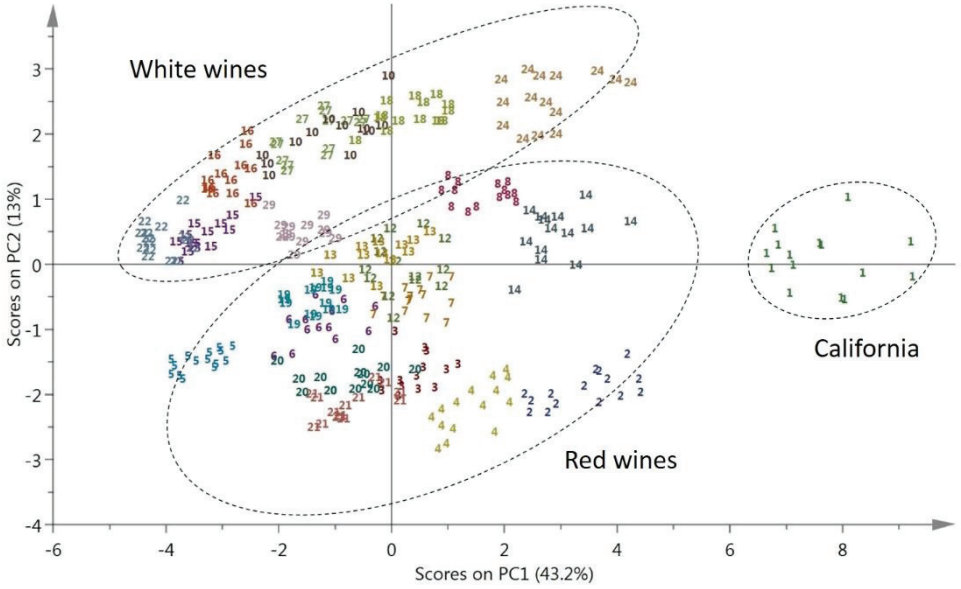

Figure 4.9 PCA score plot of the red and white wines with a plasma temperature of about 8000 K.

4.3.5 Classification of the red wines according to their production regions

Figure 4.10 shows the PCA score plot for the 14 red wines from 5 regions (California, Beaujolais, Bordeaux, Bourgogne and Languedoc). As mentioned before, the wine from California (n°1) is always well separated from the other wines produced in France. While for the French wines, three clusters appear as shown in Fig. 4.10, which correspond to the three production regions of Beaujolais, Bourgogne and Languedoc. With a detailed check of the spectra of the wines from the 3 above regions, we can find that the most abundant elements are Mn and Ba for Beaujolais, K and Ca for Bourgogne, and Na for Languedoc (with a quite straightforward explanation of the influence of the salty Mediterranean Sea). We remark also that there is no specific cluster corresponding to the 4 Bordeaux red wines (n°5, n°6, n°7 and n°8). In fact as we can see in Fig. 4.10, that the PCA scores of these wines are distributed into the cluster of the Languedoc wines for the wines n°5 and n°6 from Haut-Médoc, and into the cluster of the Bourgogne wines for the wines n°7 from Saint-Emilion and n°8 from Graves. Such behaviors of the Bordeaux wines can be explained by the variety of the vineyard terroirs in the Bordeaux wine production site.

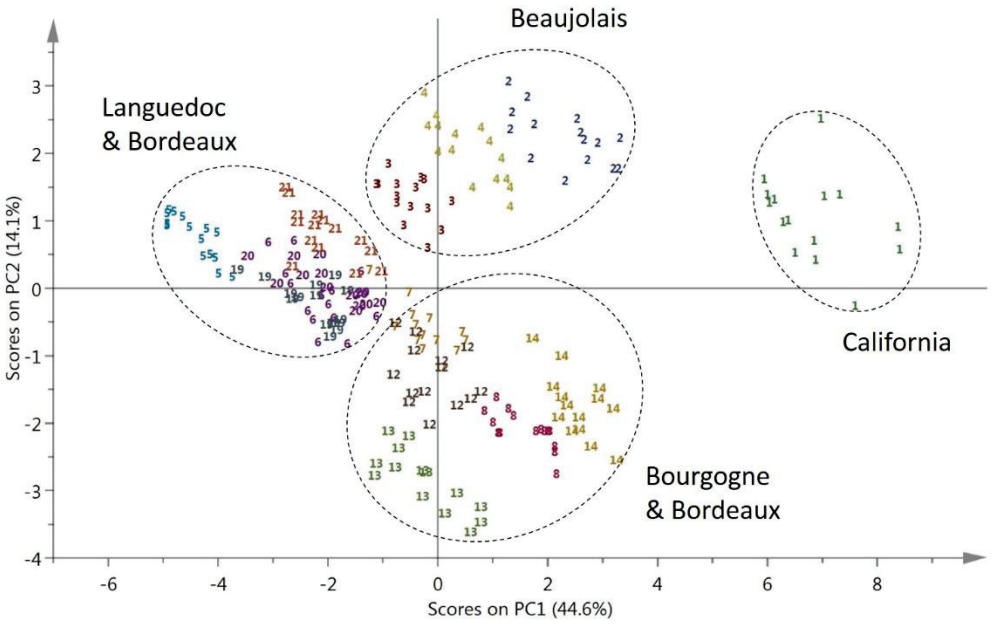

Figure 4.10 PCA score plot of red wines from the five regions.

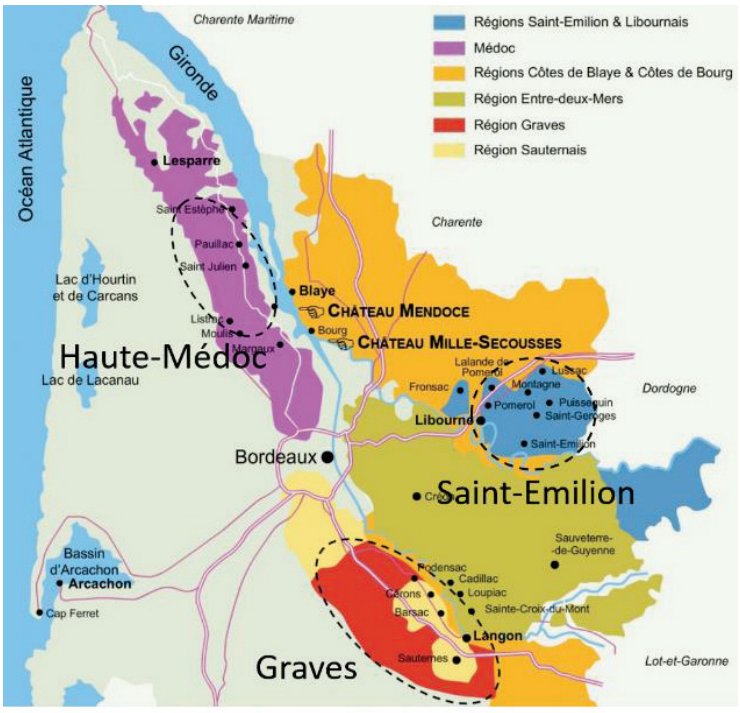

Figure 4.11 Map of the wine production sites in the Bordeaux region.

As we can see in Fig. 4.11, the vineyard of Haut-Médoc situates in the delta of the Gironde River close to the Atlantic Ocean. Such geographic situation of the vineyard makes the produced wines influenced by the climate and the terroir of seaside. It would explain the observed merge of these two wines into the cluster of the Languedoc wines.

On the other hand, the PCA scores of the two red wines (n°7 and n°8) from Saint-Emilion and Graves are observed to merge into the cluster of the Bourgogne wines. This is logical taking into account the similar characteristics of these two production sites in the Bordeaux production region, which are located in hills as the Bourgogne production region. There are probably some similitude between the soils in the two regions and the wine making process. Nevertheless, further investigations with more wine samples are needed to confirm these results.

4.4 Classification with random forest based on a variable importance model

In this section, the classification procedure and results for the tested wines with random forest (RF) are presented. In this work, 300 spectra (10 spectra for each wine sample) were randomly selected as the training set to build the RF model, and the rest 150 spectra (5 spectra for each wine sample) were used as the test set. The RF analysis was performed using a laboratory-developed software developed in the environment of MATLAB (version 2010b, Mathworks).

4.4.1 Random forest (RF) method

RF, as an advanced classification and regression method based on statistical learning theory, was proposed by Breiman in 2001 [186]. Briefly, it is an ensemble of classifiers consisting of many decision trees, where the final predicted class for a test sample is obtained by majority voting of all the single classification trees [187]. It is proved that RF classifier has a good tolerance for the noise, as well as avoid over-fitting phenomenon [188]. Recently, LIBS combined with RF method has been used for the identification and classification of rocks [189], iron ores [190] and slag samples [191]. It has also been used for the quantitative analysis of multiple elements in steel samples [192].

RF model construction

A resampling technique based on bootstrap method is used to continuously generate the bootstrap samples and out-of-bag (OOB) samples from the original training set.

Bootstrap samples are randomly drawn with the replacement from the training set. For each bootstrap, different spectra of the dataset are used to construct the RF model. Hence, some of the samples will be repeated, while others will be 'left out' from the training set and form OOB samples (~37% of the samples in original dataset) [186]. The OOB samples are used to constitute the OOB error and to receive a running unbiased estimate of the classification error and variable importance for constructing the tree.

For a given training set, $A = \{(x_1, y_1), (x_2, y_2), \cdots, (x_n, y_n)\}$, where x_i is the spectrum of the sample, y_i is its corresponding category, and n is the number of spectra in the training set. The RF model training can be described as follows:

i) From the training data of n spectra, a set of bootstrap samples is randomly drawn to construct a classification tree.

ii) At each node of the classification tree, choose the best split among a randomly selected subset of m_{try} (instead of all the input variables). Here for each tree, m_{try} is essentially the only tuning parameter in the algorithm. The tree is grown to the maximum size (until no further splits are possible) and not pruned back.

iii) Repeat the above steps until the defined number of trees (n_{tree}) are grown.

After training, for a test spectrum x', the predicted category y' can be determined by taking the majority vote of the predictions from all the individual classification trees on x'.

RF Model estimation

The classification performance of the RF model can be measured through the generalization error by OOB estimation [186]. The smaller the classification error, the better the classification performance, and vice versa. The parameters in RF model can also be optimized based on the OOB estimation.

The OOB error is calculated by an estimate of the error rate (ER) for classification using the equation as follows [193]:

$$ER^{OOB} = \frac{1}{n}\sum_{i=1}^{n} I\left[Y^{\hat{OOB}}(X_i) \neq Y_i\right]. \quad (4\text{-}1)$$

Since each training feature X_i is in an OOB sample, we can calculate an ensemble prediction $Y^{\hat{OOB}}(X_i)$ by aggregating only its OOB predictions, where $I[\cdot]$ is an indicator function testing whether the $Y^{\hat{OOB}}(X_i)$ belongs or not to Y_i. Y_i is the observed output and n represents the total number of OOB samples.

The classification accuracy of the OOB samples in the training dataset can also be used to assess the performance of the RF model, and is defined by:

$$Classfication\ accuracy = \frac{Number\ of\ correctly\ identified\ samples}{Number\ of\ total\ samples} \times 100\% \quad (4\text{-}2)$$

Variable importance

A significant characteristic of RF is the ability to calculate and rank the importance of each input variable [186]. For each tree grown in RF, OOB is put down and the number of vote cast for the correct class is counted. The value of the variable m in OOB is randomly permuted and these samples are put down the tree. The numbers of votes are counted for the correct class in the variable-m-ranked OOB data; and then, the number of votes for the correct class in the untouched OOB data is again counted. Subtracting the two counts, and averaging this number over all the trees in the forest give the raw score importance for the variable. Finally, the importance of the scores are computed depending on the correlation between the trees, in other words, it is obtained depending on the contribution of the input variable to the classification result.

The extracted variable importance can be further used for the feature selection procedure of the RF model. The process of RF model based on variable importance (VIRF) can be summarized as following [191]:

i) Assuming that there is an original spectra set A, which can be used to construct a RF classification model;

ii) Calculating the variable importance of each input variable for the classification analysis based on OOB error;

iii) Removing the variable if the variable importance is lower than a threshold value, and generate a new input variable set B;

iv) The input variable set B is then used to construct a new VIRF classification model.

4.4.2 Parameter optimization of the RF model for wines classification

There are two important parameters in a RF model: the number of trees in the forest (n_{tree}), and the number of peaks randomly selected as the candidates for splitting at each node (m_{try}). An ideal RF model not only has high classification accuracy and stability, but also has high efficiency. Theoretically, the generalization error of a classifier tends to a finite upper bound when n_{tree} reaches a certain value [194]. In other words, if n_{tree} is increased above the optimal value, there is in general an increase in the computational time without significant improvement of the classification result. In the present work, selecting the number of trees was the first step of the construction of the RF model from the ensemble of 500 trees initially set. The OOB classification error as a function of the number of grown trees, n_{tree}, is shown in Fig. 4.12. We can see that the OOB error stops to decrease with the number of trees beyond a certain value of about 88, which means that the model does not over-fit when n_{tree} reaches this value, no matter how many trees are grown. The optimal number of trees was determined to be the one that reached a relatively stable trend at the lowest OOB error. 88 was therefore chosen as the optimal parameter in our models, when the OOB error was at the lowest level as marked by a red arrow in Fig. 4.12.

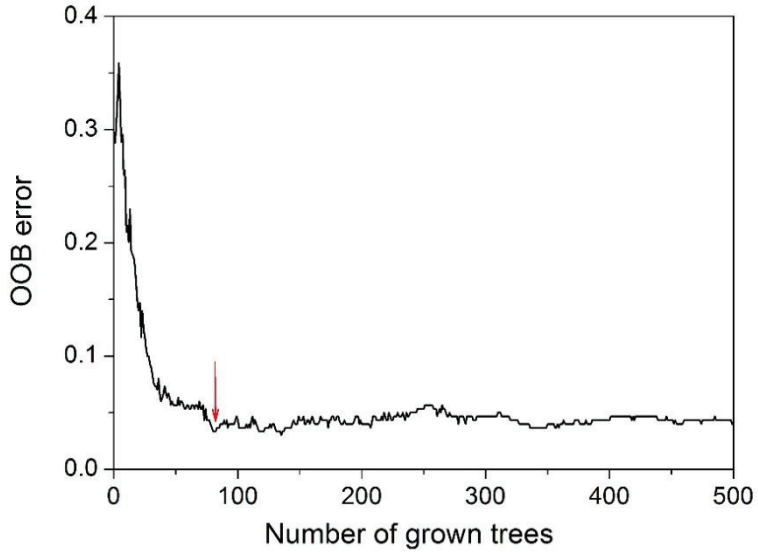

Figure 4.12 Determination of the tree number (n_{tree}) in the RF model: OOB mean square error as a function of the number of the grown trees.

m_{try} is another major feature through each division that introduces random nodes for randomly selected attributes. It was assumed that there were M attributes ($M = 21915$ pixels in a spectrum, when all the spectrum was used as input variables) in the training sample, then m_{try} attributes were extracted randomly as candidate attributes between each of the internal nodes in the decision tree ($m_{try} \ll M$). Actually, $m_{try} = \sqrt{M} = 148$ variables, was found to be the best choice based on the OOB error rate [195]. The 148 selected variables included some useful chemical information to facilitate the classification, and these chemical information mainly consisted of LIBS spectrum with maximum diversity.

4.4.3 Predictive performances of the RF model for wines classification

As mentioned above, the classification performance of the RF model can be estimated by the classification accuracy of the OOB samples in the training set. In general, the performance of the model is estimated by a cross validation, such validation generally needs an extensive calculation and thus reduces the efficiency of the evaluation. However, when the OOB data is used to estimate the classifier performance, the calculation time is much reduced [186]. The OOB estimation is convenient for the RF models owing to the utilization of the bootstrap method of data selection.

Table 4-3 shows the classification accuracies of the RF model for the wine samples based on OOB estimation. We can see that the RF model shows good predictive performances for wines classification according to their production regions, the classification accuracies are all better than 96.00%. The classification accuracies of the wines from the 4 production regions of California, Beaujolais, Bordeaux and Bourgogne are over than 99.00%. However, the classification accuracies of the wines from Languedoc and Alsace are lower than this value (97.67% and 96.62%) probably due to a strong discrepancy in electron density and temperature of the plasmas, as discussed in Section 4.3.3.

Table 4-3 Classification accuracies of the RF model for all the wine samples, based on OOB estimation with the intensities of all the pixels of a spectrum as the input variables.

Production regions	Classification accuracy (%)
California	99.96
Beaujolais	99.33
Bordeaux	99.37
Bourgogne	99.32
Languedoc	97.67
Alsace	96.62

4.4.4 Classification of wines according to their production regions with a VIRF model

We then extracted the variable importance of each input variable in the RF model to make a feature selection. By removing the variable whose variable importance is lower than a certain value, we can finally construct a new VIRF classification model. The obtained results are presented in Table 4-4, where we can find the classification accuracies calculated for all the 150 test spectra from the 30 wine samples. We can see that the classification accuracies are 97.3% and 96.7% with all the pixel intensities of the whole spectrum as the input variables, respectively with and without normalization with the Y I line. In this case, some of the input variables have a variable importance equal to 0,

therefore do not contribute to the classification of the wines. Hence, we can remove the corresponding pixel intensities in a LIBS spectrum from the list of the input variables of the RF classification model. The remaining pixel intensities in a spectrum corresponding to the spectral features with a variable importance larger than 0 are kept as the input variables of a new generation of RF classification model. We repeated such procedure several times, with at each step an increasing threshold value for the variable importance, and by consequence, a decreasing number of pixel intensities as the input variables of a new generation of RF classification model.

Table 4-4 Classification accuracies and the corresponding number of input variables for RF models using raw or normalized intensities. The results obtained with the characteristic line listed in Table 4-2 are also presented in the bottom line of the table.

Input variables		RF model without normalization		RF model normalized by Y	
		Number of variables	Classification accuracy (%)	Number of variables	Classification accuracy (%)
Whole spectrum		21915	97.3	21915	96.7
Variable importance	>0	9598	100	8347	97.3
	≧0.1	372	100	421	99.3
	≧0.2	119	100	144	97.3
	≧0.3	48	98.7	61	98
	≧0.4	31	98.7	23	98
	≧0.5	12	92.7	5	87.3
	≧0.6	4	77.3	2	77.3
	≧0.7	3	76.7	0	--
	≧0.8	3	76.7	0	--
	≧0.9	2	73.3	0	--
	≧1.0	2	73.3	0	--
Characteristic lines		17	100	17	100

In Table 4-4, we present the detailed results of the VIRF classification. We can see in particular, the numbers of input variables, the corresponding classification accuracies when the model used the intensities of all the pixels in a spectrum and when the variable

importance was considered with difference threshold values. In the bottom line of the table, we can see the results when the intensities of the characteristic lines considered in Section 4.3.1 (Table 4-2) were used as input variables in the RF models. All of the results are shown in Table 4-4 with raw intensities and with normalized intensities with the Y I line.

We can first observe the influence of the variable importance on the classification accuracy. When the intensities of all the pixels of a spectrum are used as input variables, the obtained classification accuracies are respectively 97.3% and 96.7% for the raw intensities and the normalized ones. As soon as the variable importance is set to be larger than 0, the obtained results show classification accuracies of 100% and 97.3% with raw intensities and normalized intensities respectively. Correspondingly, the number of input variables respectively decrease from the initial value of 21915 to 9598 and 8347. When the threshold value of variable importance continues to increase up to be equal or larger than 0.1, the classification performance continues to be improved with respective classification accuracies of 100% and 99.3% for raw intensities and normalized intensities, with obviously a decreased number of input variables for the model. With further increase of the threshold value of the variable importance, we can observe a constant classification accuracy of 100% with raw intensities, while a decreased classification accuracy with normalized intensities. Beyond a threshold value of 0.3 of the variable importance, the classification accuracies globally decrease. This can be understood by the drastic decrease of input variables of the RF model, the too few remaining intensities (or variables) do not provide anymore a representative set of variables of the analyzed spectrum. The results show also that with raw intensities, a classification accuracy of 100% can be reached, while with normalized intensities, the best classification accuracy rate is 99.3%. This might mean that the normalization with an internal reference introduces somehow an artificial perturbation in the spectra, which may decrease the inherent correlation among the spectra of the wine samples from the same production region. It is finally quite remarkable to observe that when the characteristic lines selected in Section 4.3.1 (Table 4-2) are used as the input variables of a RF model, the classification accuracies are identically 100% for

raw intensities and normalized ones. This clearly shows the pertinence of the selection of the fingerprint elements and the associated characteristic lines, and the agreement between an artificial selection based on physical and chemical considerations and a selection based on an automatic procedure.

In the point of view of the computation time, since the used spectra had a quite high resolution over a quite wide spectral range, it took a long time to construct a RF training model. When the intensities of all the 21915 pixels in a spectrum was used as the input variables, the modeling time was about 2 minutes with the used computer (a PC with a CORE i7 processor). When the variable importance was set to be larger than 0, the modeling time was significantly reduced to be in the order of several seconds. Such a reduction of the computation time could be crucial for a practical application.

4.5 Resume

In this chapter, we have used the surface-assisted LIBS technique for the classification of French wines according to their production regions. The sensitivity of the technique allowed 17 elements (Na, Mg, K, and Ca as majors, Li, B, Si, P, Ti, Mn, Fe, Cu, Zn, Rb, Sr, Ba and Pb as minors and traces), in addition to C, H, O, N and Al, being detected in a typical wine. A non-supervised classification model based on PCA was first developed for the classification. The effect of spectrum normalization was studied with Y as an internal reference. A general rule of using an atomic or an ionic line of the internal reference to normalize an atomic or an ionic line, respectively, has been deduced with practical interest. Thus, the respectively normalized emission intensities of 17 atomic and ionic lines were used as input variables for PCA analysis. It was shown that the classification of all the wines was dominated by the matrix effects: the PCA score plot showed clusters of wines with similar electron density and temperature of the corresponding plasmas. By applying PCA to the subset of white and red wines with the similar electron densities and temperatures, the white wines appeared separated from the red wines. By further considering the red wines, the PCA model was able to partially classify them according to their production sites. It however failed to classify the wine

samples from Bordeaux region. These results showed a limited separation power of the PCA model, which however allowed, in a step by step approach, to understand the physical reasons behind each step of sample separation and especially to observe the influence of the matrix effect in the sample classification.

A supervised classification model based on RF was then developed for wines classification. The parameters n_{tree} and m_{try} in the RF model were determined based on the OOB error, with the respective optimized values of 88 and 148. The classification performance of the RF model was then assessed based on OOB estimation. It was shown that the classification accuracies are all better than 96.00% for the wines from different production regions. Finally, we implemented the VIRF model and showed the influence of the variable importance on the classification accuracy. By properly setting the threshold value of the variable importance, satisfactory classification results were obtained with, in the best cases, a classification accuracy of 100% for all the tested wines. This indicated that the RF method is more powerful for wines classification in this work than the PCA method. In addition, the computation time was significantly reduced with the VIRF model, which could be crucial for practical applications. Nevertheless, future works are needed to increase the number and the variety of the wine samples for a robustness test, before the developed method could be applied in practical analyses.

We conclude that, comparing to other elemental analytical techniques which have been demonstrated as suitable ones for providing satisfactory classification of wines according to their production regions, LIBS can certainly provide easier and quicker classifications without use of any chemical reagent nor sophisticated equipment for complicated sample preparation, which should represent a decisive advantage for applications dedicated to fast screenings and/or field inspections of a large amount of wines or other beverages.

Conclusions and future directions

This thesis work has been motivated by two basic needs in the improvement of LIBS technique for qualitative and quantitative analyses purposes: a better understanding of the fundamental aspects of laser-induced plasma as the spectroscopic emission source for LIBS, and new sample preparation methods for LIBS measurement to improve the analytical performance while keeping the technique still enough simple. Accordingly, the main part of the thesis manuscript is divided into two parts. The first part is dedicated to characterize the plasma induced on glass samples under different ablation conditions (Chapter 2); the second part corresponds to the development of the surface-assisted LIBS method for elemental analyses in powders (Chapter 3) as well as in wines (Chapter 4). The obtained results and conclusions can be summarized into the following three aspects.

1. **Characteristics of the plasma induced on glass samples as a function of the ablation laser wavelength and ambient gas.**

In this study, we have investigated the characteristics of ablation plume induced on float and frosted glasses by IR or UV laser pulse in an ambient gas of air or argon [196]. Both the spectroscopic imaging and time- and space-resolved emission spectroscopy were used for plasma diagnostics in the present study. The obtained results first show that in all the ablation conditions studied here, the post-ablation interaction can be described by the LSC wave, which results in a rather hemispherical form of the plasma with a layered internal structure for different species in the plume, at short detection delays. Further observations of the profiles of the emission lines, electron density and temperature at longer delays beyond 0.5 µs confirm the characteristics of the morphology of the plasma observed in shorter delays. When comparing between the ablations with IR and UV laser pulses, higher electron densities and higher temperatures are observed for the IR plasma than for the UV plasma whatever in air or in argon ambient. The plasma with IR ablation continues to propagate at longer delays, while the UV plasma is more static. When comparing ambient gases of air and argon, higher electron densities are observed for the

IR plasma in argon, and higher temperatures are observed for the UV plasma in argon, which implies a stronger confinement effect of the argon gas.

The characteristics of the plasma naturally result in different analytical performances of the plasmas induced in the different conditions. We thus observed a shorter delay with UV ablation for an optimal signal-to-noise ratio than with IR ablation. We also observed a higher signal-to-noise ratio with IR laser than with UV laser, in air as well as in argon. When dealing with resonant emission lines, the plasma induced by UV pulse appears more suffering from self-absorption than that induced by IR pulse, in air as well as in argon. Finally, the use of argon as ambient gas leads to a significantly reduced self-absorption effect for UV plasma and especially for IR plasma. The results presented in this chapter provide therefore useful information for the choice of experimental parameters for LIBS analysis of glass-like samples, such as gemstones.

2. Quantitative analysis of powder samples with surface-assisted LIBS.

In this study, we have developed and evaluated a method of powders analysis with surface-assisted LIBS [197], the main purpose is to reduce the matrix effect in elemental analysis of powders using LIBS. We first applied this method on a cellulose powder spiked with TiO_2 nanoparticles. The parameters of figures-of-merit extracted from the calibration graphs show LODs in the range of several ppm, which are comparable with the LODs in LIBS analysis of the corresponding pellet samples. We especially demonstrate that the best reference lines for spectrum normalization are not necessary belonging to an internal standard element coming from the sample matrix as recommended by usual considerations. An element contributed by the ambient gas can also provide suitable reference lines. The additional condition that should be taken into account in particular for an inhomogeneous emission source like laser-induced plasma, is that the spatial distributions of the reference element and the elements to be normalized should have a good overlap.

In the second step, we focused on the matrix effect by preparing another series of samples with an alumina powder. The results obtained with the surface-assisted method

were then compared to those obtained with classical pellet method. We show that the important advantage of the surface-assisted method is an efficient reduction of matrix effect. At least for the two tested kinds of powders (cellulose and alumina powders), a universal calibration curve could be established for elemental analysis of the two matrices, while the comparative measurements with corresponding pellets show a clear matrix effect.

Finally, we applied the surface-assisted LIBS method to the analysis of soils as real powder samples. Four different types of soils were tested in the experiment to make an assessment of the method. The preliminary results show clearly the efficiency of the surface-assisted method to reduce the matrix effect for soil powder analysis. The calibration curves of Ag I 328.1 nm line for the four soils prepared in thin films are much closer to each other than for those samples prepared in pellets. The RSD of the slopes of the calibration curves is significantly reduced from 24.3% to 9.0% by using the surface-assisted LIBS method. The effect of spectrum normalization with an internal reference element of Y appears more complex to explain. The major difficulty to apply spectrum normalization with an internal reference is the choice of a proper reference line. For such complex samples as soils, spectral interferences represent a major challenge for a good normalization.

3. Classification of wines according to their production regions with surface-assisted LIBS.

In this study, we have used the surface-assisted LIBS technique for the classification of French wines according to their production regions [198]. The sensitivity of the technique allowed 17 elements (Na, Mg, K, and Ca as majors, Li, B, Si, P, Ti, Mn, Fe, Cu, Zn, Rb, Sr, Ba and Pb as minors and traces), in addition to C, H, O, N and Al, being detected in a typical wine. A non-supervised classification model based on PCA was first developed for the classification. It was shown that the classification of all the wines was dominated by the matrix effects: the PCA score plot showed clusters of wines with similar electron density and temperature of the corresponding plasmas. By considering the subset of red wines which correspond to similar plasma parameters, the PCA model was able to

classify partially the wine samples according to their production sites. It however failed to classify the wine samples from Bordeaux region. These results showed a limited separation power of the PCA model, which however allowed, in a step by step approach, to understand the physical reasons behind each step of sample separation and especially to observe the influence of the matrix effect in the sample classification.

A supervised classification model based on RF was then used for wines classification. The parameters n_{tree} and m_{try} in the RF model were determined based on the OOB error, with the respective optimized values of 88 and 148. The classification performance of the RF model was then assessed based on OOB estimation. It was shown that the classification accuracies are all better than 96.00% for the wines from different production regions. Finally, we implemented the VIRF model and showed the influence of the variable importance on the classification accuracy. By properly setting the threshold value of the variable importance, satisfactory classification results were obtained with, in the best cases, a classification accuracy of 100% for all the tested wines. This indicated that the RF method is more powerful for wines classification in this work than the PCA method. In addition, the computation time was significantly reduced with the VIRF model, which could be crucial for practical applications. We conclude that surface-assisted LIBS is an easier, quicker and environmentally friendly technique which could be potentially used for field inspections of a large amount of wines or other beverages.

My future research directions, in relation with the research interests of my new research team in Ocean University of China, will continue to include the both fundamental and application aspects of LIBS technique. For the fundamental aspect, I would work in the direction of developing the characterization of laser-induced plasma in extreme conditions. Especially, I will interest in the mechanism of laser-induced plasma in the underwater condition. This research direction is driven by important applications of LIBS technique in deep-sea explorations (e.g. 4000 m depth corresponding to 40 MPa pressure under seawater) [199,200]. Same types of investigations can also be extended to the investigation of LIBS measurement conditions in space explorations of Mars (7 Torr CO_2 or 933 Pa) [29-33] and Venus (9.1 MPa CO_2) [201,202] for example. For these studies,

in extremely low or high pressures, laser-induced plasma will behave completely differently from its generation to its propagation into the ambient gas or water. Specific chambers coupled with plasma diagnostic techniques are needed to simulate these conditions in the laboratory.

Concerning the application aspect of my future research activities, I am interested in combining the LIBS technique with chemometric methods in order to fully use the analytical information contained in a LIBS spectrum. This approach is particularly important to treat some complex samples, such as soils, which have very high application relevance. In particular, it is expected that the chemometric method could significantly improve the performance of LIBS analysis. For example, in Chapter 4, the wine samples can be successfully classified by using the RF method, although there are evident matrix effects in the surface-assisted LIBS measurements. Moreover, this gives us the hope to overcome the matrix effects in quantitative analysis of soils based on our works presented in Chapter 3. We can expect first to reduce the matrix effects by surface-assisted method during LIBS experiment, and then to eliminate completely the residual matrix effects by chemometric method in the data processing. Actually, this work is being undertaken in our laboratories now.

References

1. F. Brech, L. Cross, Optical microemission stimulated by a ruby maser, Appl. Spectrosc. 16 (1962) 59.
2. J. Debras-Guédon, N. Liodec, De l'utilisation du faisceau issu d'un amplificateur à ondes lumineuses par emission induite de rayonnement (laser à rubis), comme source énergétique pour l'excitation des spectres d'emission des éléments, C.R. Acad. Sci. 257 (1963) 3336–3339.
3. D.A. Cremers, L.J. Radziemski, Handbook of Laser-Induced Breakdown Spectroscopy, John Wiley & Sons, Chichester, 2006.
4. A.W. Miziolek, V. Palleschi, I. Schechter, (Eds), Laser-induced breakdown spectroscopy: Fundamentals and applications, Cambridge University Press, 2006.
5. L.J. Radziemski, T.R. Loree, Laser-induced breakdown spectroscopy: time-resolved applications, J. Plasma Chem. Plasma Proc. 1 (1981) 281–293.
6. D.A. Cremers, L.J. Radziemski, Detection of chlorine and fluorine in air by laser-induced breakdown spectrometry, Anal. Chem. 55 (1983) 1252–1256.
7. L.J. Radziemski, D.A. Cremers, T.R. Loree, Detection of beryllium by laser-induced breakdown spectroscopy, Spectrochim. Acta Part B 38 (1983) 349–355.
8. D.A. Cremers, L.J. Radziemski, Direct detection of beryllium on filters using the laser spark, Appl. Spectrosc. 39 (1985) 57–63.
9. L.J. Radziemski, T.R. Loree, D.A. Cremers, N.M. Hoffman, Time-resolved laser-induced breakdown spectrometry of aerosols, Anal. Chem. 55 (1983) 1246–1252.
10. J.D.Winefordner, I.B. Gornushkin, T. Correll, E. Gibb, B.W. Smith, N. Omenetto, Comparing several atomic spectrometric methods to the super stars: special issue on laser induced breakdown spectrometry, LIBS, a future super star, J. Anal. Atom. Spectrom. 19 (2004) 106–108.
11. S. Pandhija, N. Rai, A. Rai, S. Thakur, Contaminant concentration in environmental samples using LIBS and CF-LIBS, Applied Physics B 98 (2010) 231–241.
12. R. Wisbrun, I. Schechter, R. Niessner, H. Schroeder, K.L. Kompa, Detector for trace elemental analysis of solid environmental samples by laser plasma spectroscopy, Anal. Chem. 66 (1994) 2964–2975.
13. M.Z. Martin, N. Labbé, N. André, R. Harris, M. Ebinger, S.D. Wullschleger, A.A. Vass, High resolution applications of laser-induced breakdown spectroscopy for environmental and forensic applications, Spectrochim. Acta Part B 62 (2007) 1426–1432.
14. R. Noll, V. Sturm, Ü. Aydin, D. Eilers, C. Gehlen, M. Höhne, A. Lamott, J. Makowe, J. Vrenegor, Laser-induced breakdown spectroscopy—from research to industry, new frontiers for process control, Spectrochim. Acta Part B 63 (2008) 1159–1166.
15. N.K. Rai, A.K. Rai, LIBS—an efficient approach for the determination of Cr in industrial wastewater, Journal of hazardous materials, 150 (2008) 835–838.

16. P. Werheit, C. Fricke-Begemann, M. Gesing, R. Noll, Fast single piece identification with a 3D scanning LIBS for aluminium cast and wrought alloys recycling. J. Anal. Atom. Spectrom. 26 (2011), 2166–2174.

17. J.L. Gottfried, R.S. Harmon, F.C. De Lucia Jr., A.W. Miziolek, Multivariate analysis of laser-induced breakdown spectroscopy chemical signatures for geomaterial classification, Spectrochim. Acta Part B 64 (2009) 1009–1019.

18. N.J. McMillan, S. Rees, K. Kochelek, C. McManus, Geological Applications of Laser-Induced Breakdown Spectroscopy, Geostand. Geoanal. Res. 38 (2014) 329–343.

19. J.M. Anzano, M.A. Villoria, A. Ruíz-Medina, R.J. Lasheras, Laser-induced breakdown spectroscopy for quantitative spectrochemical analysis of geological materials: Effects of the matrix and simultaneous determination, Anal. Chim. Acta 575 (2006) 230–235.

20. M. Baudelet, L. Guyon, J. Yu, J.P. Wolf, T. Amodeo, E. Frejafon, P. Laloi, Spectral signature of native CN bonds for bacterium detection and identification using femtosecond laser-induced breakdown spectroscopy, Appl. Phys. Lett. 88 (2006) 063901.

21. L.C. Trevizan, D. Santos, R.E. Samad, N.D. Vieira, L.C. Nunes, I.A. Rufini, F.J. Krug, Evaluation of laser induced breakdown spectroscopy for the determination of micronutrients in plant materials, Spectrochim Acta B 64 (2009) 369–377.

22. V. Motto-Ros, L. Sancey, X. Wang, Q. Ma, F. Lux, X. Bai, G. Panczer, O. Tillement, J. Yu, Mapping nanoparticles injected into a biological tissue using laser-induced breakdown spectroscopy, Spectrochim Acta Part B 87 (2013) 168–174.

23. K. Müller, H. Sterge, Evaluation of the analytical potential of laser-induced breakdown spectrometry (LIBS) for the analysis of historical glasses, Archaeometry 45 (2003) 421–433.

24. N. Carmona, M. Oujja, E. Rebollar, H. Römich, M. Castillejo, Analysis of corroded glasses by laser induced breakdown spectroscopy, Spectrochim. Acta Part B 60 (2005) 1155–1162.

25. A. Giakoumaki, K. Melessanaki, D. Anglos, Laser-induced breakdown spectroscopy (LIBS) in archaeological science—applications and prospects, Anal. Bioanal. Chem. 387 (2007) 749–760.

26. C.M. Bridge, J. Powell, K.L. Steele, M.E. Sigman, Forensic comparative glass analysis by laser-induced breakdown spectroscopy, Spectrochim. Acta Part B 62 (2007) 1419–1425.

27. E.M. Rodriguez-Celis, I.B. Gornushkin, U.M. Heitmann, J.R. Almirall, B.W. Smith, J.D. Winefordner, N. Omenetto, Laser induced breakdown spectroscopy as a tool for discrimination of glass for forensic applications, Anal. Bioanal. Chem. 391 (2008) 1961–1968.

28. B.E. Naes, S. Umpierrez, S. Ryland, C. Barnett, J.R. Almirall, A comparison of laser ablation inductively coupled plasma mass spectrometry, micro X-ray fluorescence spectroscopy, and laser induced breakdown spectroscopy for the discrimination of automotive glass, Spectrochim. Acta Part B 63 (2008) 1045–1050.

29. A.K. Knight, N.L. Scherbarth, D.A. Cremers, M.J. Ferris, Characterization of laser-induced breakdown spectroscopy (LIBS) for application to space exploration, Appl. Spectrosc. 54 (2000) 331–340.

30. F. Colao, R. Fantoni, V. Lazic, A. Paolini, F. Fabbri, G.G. Ori, L. Marinangeli, A. Baliva, Investigation of LIBS feasibility for in situ planetary exploration: An analysis on Martian rock analogues, Planet. Space Sci. 52 (2004) 117–123.

31. B. Sallé, D.A. Cremers, S. Maurice, R.C. Wiens, P. Fichet, Evaluation of a compact spectrograph for in-situ and stand-off laser-induced breakdown spectroscopy analyses of geological samples on Mars missions, Spectrochim. Acta Part B 60 (2005) 805–815.

32. S. Maurice, R.C. Wiens, M. Saccoccio, et al., The ChemCam instrument suite on the Mars Science Laboratory (MSL) rover: Science objectives and mast unit description, Space Sci. Rev. 170 (2012) 95–166.

33. R.C. Wiens, S. Maurice, B. Barraclough, et al., The ChemCam instrument suite on the Mars Science Laboratory (MSL) rover: Body unit and combined system tests, Space Sci. Rev. 170 (2012) 167–227.

34. M. Noda, Y. Deguchi, S. Iwasaki, N. Yoshikawa, Detection of carbon content in a high-temperature and high-pressure environment using laser-induced breakdown spectroscopy, Spectrochim. Acta Part B 57 (2002) 701–709.

35. B. Bousquet, G. Travaille, A. Ismael, L. Canioni, K.M.L. Pierres, E. Brasseur, S. Roy, I. le Hecho, M. Larregieu, S. Tellier, M. Potin-Gauder, T. Boriachon, P. Wazen, A. Diard, S. Belbeze, Development of a mobile system based on laser-induced breakdown spectroscopy and dedicated to in situ analysis of polluted soils, Spectrochim Acta B 63 (2008) 1085–1090.

36. B. Salle, P. Mauchien, S. Maurice, Laser-induced breakdown spectroscopy in open-path configuration for the analysis of distant objects, Spectrochim Acta B 62 (2007) 739–768.

37. Y. Groisman, M. Gaft, Online analysis of potassium fertilizers by laser-induced breakdown spectroscopy, Spectrochim Acta B 65 (2010) 744–749.

38. E. Tognoni, V. Palleschi, M. Corsi, G. Cristoforetti, Quantitative micro-analysis by laser-induced breakdown spectroscopy: a review of the experimental approaches, Spectrochim Acta B 57 (2002) 1115–1130.

39. V. Motto-Ros, L. Sancey, Q.L. Ma, F. Lux, X.S. Bai, X.C. Wang, J. Yu, G. Panczer, O. Tillement, Mapping of native inorganic elements and injected nanoparticles in a biological organ with laser-induced plasma, Appl. Phys. Lett. 101 (2012) 223702.

40. M. Hoehse, A. Paul, I. Gornushkin, U. Panne, Multivariate classification of pigments and inks using combined Raman spectroscopy and LIBS, Anal. Bioanal. Chem. 402 (2012) 1443–1450.

41. X.K. Shen, Y.F. Lu, Detection of uranium in solids by using laser-induced breakdown spectroscopy combined with laser-induced fluorescence, Appl. Opt. 47 (2008) 1810–1815.

42. S.C. Jantzi, V. Motto-Ros, F. Trichard, Y. Markushin, N. Melikechi, A. De Giacomo, Sample treatment and preparation for laser-induced breakdown spectroscopy, Spectrochim Acta B 115 (2016) 52–63.

43. D.W. Hahn, N. Omenetto, Laser-induced breakdown spectroscopy (LIBS), part I: review of basic diagnostics and plasma–particle interactions: still-challenging issues within the analytical plasma community, Appl. Spectrosc. 64 (2010) 335A–366A.

44. D.A. Cremers, R.C. Chinni, Laser-induced breakdown spectroscopy-capabilities and limitations, Appl. Spectrosc. Rev. 44 (2009) 457–506.

45. S. Musazzi, U. Perini, Laser-induced breakdown spectroscopy: theory and applications, Springer, 2014.

46. A. De Giacomo, M. Dell'Aglio, R. Gaudiuso, S. Amoruso, O. De Pascale, Effects of the background environment on formation, evolution and emission spectra of laser-induced plasmas, Spectrochim Acta B 78 (2012) 1–19.

47. F.F. Al-Adel, M.A. Dastageer, K. Gasmi, M.A. Gondal, Optimization of a laser induced breakdown spectroscopy method for the analysis of liquid samples, J. Appl. Spectrosc. 80 (2013) 767–770.

48. L.L. Shi, Q.Y. Lin, Y.X. Duan, A novel specimen-preparing method using epoxy resin as binding material for LIBS analysis of powder samples, Talanta 144 (2015) 1370–1376.

49. L. Sancey, V. Motto-Ros, B. Busser, S. Kotb, J.M. Benoit, A. Piednoir, F. Lux, O. Tillement, G. Panczer, J. Yu, Laser spectrometry for multi-elemental imaging of biological tissues, Sci. Rep. 4 (2014) 6065.

50. Q. Ma, Structure et dynamique du plasma induit par laser en propagation dans un gaz ambiant d'argon, Thèse Université Lyon 1 (2012).

51. X. Bai, Laser-induced plasma as a function of the laser parameters and the ambient gas, Thèse Université Lyon 1 (2014).

52. Q. Ma, V. Motto-Ros, W. Lei, M. Boueri, X. Bai, L. Zheng, H. Zeng, J. Yu, Temporal and spatial dynamics of laser-induced aluminum plasma in argon background at atmospheric pressure: Interplay with the ambient gas, Spectrochim. Acta Part B 65 (2010) 896–907.

53. Q. Ma, V. Motto-Ros, F. Laye, J. Yu, W. Lei, X. Bai, L. Zheng, H. Zeng, Ultraviolet versus infrared: effects of ablation laser wavelength on the expansion of laser-induced plasma into one-atmosphere argon gas, J. Appl. Phys. 111 (2012) 053301.

54. Q. Ma, V. Motto-Ros, X. Bai, J. Yu, Experimental investigation of the structure and the dynamics of nanosecond laser-induced plasma in 1-atm argon ambient gas, Appl. Phys. Lett. 103 (2013) 204101.

55. X. Bai, Q. Ma, V. Motto-Ros, J. Yu, D. Sabourdy, L. Nguyen, A. Jalocha, Convoluted effect of laser fluence and pulse duration on the property of a nanosecond laser-induced plasma into an argon ambient gas at the atmospheric pressure, J. Appl. Phys. 113 (2013) 013304.

56. X. Bai, Q. Ma, M. Perrier, V. Motto-Ros, D. Sabourdy, N. Luc, A. Jalocha, J. Yu, Experimental study of laser-induced plasma: Influence of laser fluence and pulse duration, Spectrochim. Acta B 87 (2013) 27–35.

57. X. Bai, V. Motto-Ros, W. Lei, L. Zheng, J. Yu, Experimental determination of the temperature range of AlO molecular emission in laser-induced aluminum plasma in air, Spectrochim. Acta B 99 (2014) 193–200.

58. X. Bai, F. Cao, V. Motto-Ros, Q. Ma, Y. Chen, J. Yu, Morphology and characteristics of laser-induced aluminum plasma in argon and in air: A comparative study, Spectrochim. Acta B 113 (2015) 158–166.

59. J. Xiu, X. Bai, E. Negre, V. Motto-Ros, J. Yu, Indirect laser-induced breakdown of transparent thin gel layer for sensitive trace element detection, Appl. Phys. Lett. 102 (2013) 244101.

60. J. Xiu, V. Motto-Ros, G. Panczer, R. Zheng, J. Yu, Feasibility of wear metal analysis in oils with ppm and sub-ppm sensitivity using laser-induced breakdown spectroscopy of thin oil layer on metallic target, Spectrochim. Acta Part B 91 (2014) 24–30.

61. L. Zheng, F. Cao, J. Xiu, X. Bai, V. Motto-Ros, N. Gilon, H. Zeng, J. Yu, On the performance of laser-induced breakdown spectroscopy for direct determination of trace metals in lubricating oils, Spectrochim. Acta Part B 99 (2014) 1–8.

62. J. Menneveux, F. Wang, S. Lu, X. Bai, V. Motto-Ros, N. Gilon, Y. Chen, J. Yu, Direct determination of Ti content in sunscreens with laser-induced breakdown spectroscopy: Line selection method for high TiO_2 nanoparticle concentration, Spectrochim. Acta Part B 109 (2015) 9–15.

63. J. Yu, Q. Ma, W. Lei, X. Wang, X. Bai, Generation and expansion of laser-induced plasma as a spectroscopic emission source, Front. Phys. 7 (2012) 649–669.

64. J.L. Delcroix, A. Bers, Physique des plasmas, Paris: InterEditions/CNRS Editions, 1994.

65. M. Capitellia, A. Casavola, G. Colonna, A. De Giacomo, Laser-induced plasma expansion: theoretical and experimental aspects, Spectrochim. Acta Part B 59 (2004) 271–289.

66. G. Callies, P. Berger, H. Hugel, Time-resolved observation of gas-dynamic discontinuities arising during excimer laser ablation and their interpretation, J. Phys. D: Appl. Phys. 28 (1995) 794.

67. A.V. Gusarov, A.G. Gnedovets, I. Smurov, Two-dimensional gas-dynamic model of laser ablation in an ambient gas, Appl. Surf. Sci. 154 (2000) 66–72.

68. R.G. Root, Modeling of post-breakdown phenomena, in: L.J. Radziemski, D.A. Cremers (Eds.), Laser-induced Plasmas and Applications, Dekker, New York 1989, pp. 69–103.

69. R.E. Russo, X.L. Mao, C. Liu, J. Gonzalez, Laser assisted plasma spectrochemistry: laser ablation, J. Anal. Atom. Spectrom. 19 (2004) 1084–1089.

70. G. Cristoforetti, G. Lorenzetti, P.A. Benedetti, E. Tognoni, S. Legnaioli, V. Palleschi, Effect of laser parameters on plasma shielding in single and double pulse configurations during the ablation of an aluminium target, J. Phys. D: Appl. Phys. 42 (2009) 225207.

71. D.W. Bäuerle, Laser processing and chemistry, Springer Science & Business Media, 2013.

72. M. Stafe, C. Negutu, I.M. Popescu, Theoretical determination of the ablation rate of metals in multiple-nanosecond laser pulses irradiation regime, Appl. Surf. Sci. 253 (2007) 6353–6358.

73. S.S. Mao, X. Mao, R. Greif, R.E. Russo, Initiation of an early-stage plasma during picosecond laser ablation of solids, Appl. Phys. Lett. 77 (2000) 2464.

74. J. Richter, Ch. 1: Radiation of hot gases, in Plasma Diagnostics, Ed. W. Lochte-Holtgreven, Amsterdam: North-Holland Publishing Company, 1968.

75. X. Mao, S.B. Wen, R.E. Russo, Time resolved laser-induced plasma dynamics, Appl. Surf. Sci. 253 (2007) 6316–6321.

76. C. Aragon, J.A. Aguilera, Characterization of laser induced plasmas by optical emission spectroscopy: A review of experiments and methods, Spectrochim Acta B 63 (2008) 893–916.

77. H.R. Griem, Plasma Spectroscopy, McGraw-Hill, 1964.

78. W. Lochte-Holtgreven (Ed.), Plasma Diagnostics, North Holland Publishing Company, 1968.

79. R.W.P. McWhirter, Spectral intensities, in: R.H. Huddlestone, S.L. Leonard (Eds.), Plasma Diagnostic Techniques, Academic Press, 1965, Chapter 5.

80. J.B. Simeonsson, A.W. Miziolek, Time-resolved emission studies of ArF-laser produced microplasmas, Appl. Opt. 32 (1993) 939–947.

81. X.L. Mao, M.A. Shannon, A.J. Fernández, R.E. Russo, Temperature and emission spatial profiles of laser-induced plasmas during ablation using time-integrated emission spectroscopy, Appl. Spectrosc. 49 (1995) 1054–1062.

82. C. Aragón, J. Bengoechea, J.A. Aguilera, Influence of the optical depth on spectral line emission from laser-induced plasmas, Spectrochim. Acta Part B 56 (2001) 619–628.

83. H.R. Griem, Spectral Line Broadening by Plasmas, Academic Press, 1974.

84. A. Ciucci, M. Corsi, V. Palleschi, S. Rastelli, A. Salvetti, E. Tognoni, New procedure for quantitative elemental analysis by laser-induced plasma spectroscopy, Appl. Spectrosc. 53 (1999) 960–964.

85. J.A. Aguilera, C. Aragón, Multi-element Saha-Boltzmann and Boltzmann plots in laser-induced plasmas, Spectrochim. Acta Part B 62 (2007) 378–385.

86. Ş. Yalçin, D.R. Crosley, G.P. Smith, G.W. Faris, Influence of ambient conditions on the laser air spark, Appl. Phys. B 68 (1999) 121–130.

87. G.J. Bastiaans, R.A. Mangold, The calculation of electron density and temperature in Ar spectroscopic plasmas from continuum and line spectra, Spectrochim. Acta Part B 40 (1985) 885–892.

88. D.A. Rusak, B.C. Castle, B.W. Smith, J.D. Winefordner, Excitational, vibrational, and rotational temperatures in Nd:YAG and XeCl laser-induced plasmas, Spectrochim. Acta Part B 52 (1997) 1929–1935.

89. J.M. Mermet, P. Mauchien, J.L. Lacour, Processing of shot-to-shot data to improve precision in LIBS, Spectrochim. Acta Part B 63 (2008) 999–1005.

90. J.M. Mermet, Calibration in atomic spectrometry: a tutorial review dealing with quality criteria, weighting procedures and possible curvatures, Spectrochim. Acta B 65 (2010) 509–523.

91. K. Danzer, L.A. Currie, IUPAC. Guideline for calibration in analytical chemistry, Pure Appl. Chem. 70 (1998) 993–1014.

92. ISO 11095: Linear calibration using reference materials, 1996.

93. J.C. Miller, J.N. Miller, Statistics and Chemometrics for Analytical Chemistry, 5th editionPearson Education Limited, Harlow, 2005.

94. J. El Haddad, L. Canioni, B. Bousquet, Good practices in LIBS analysis: Review and advices, Spectrochim. Acta B 101 (2014) 171–182.

95. A. Tropsha, P. Gramatica, V.K. Gombar, The importance of being earnest: validation is the absolute essential for successful application and interpretation of QSPR models, QSAR Comb. Sci. 22 (2003) 69–77.

96. A. Golbraikh, A. Tropsha, Beware of q^2! J. Mol. Graph. Model. 20 (2002) 269–276.

97. J.M. Mermet, Limit of quantitation in atomic spectrometry: an unambiguous concept? Spectrochim. Acta B 63 (2008) 166–182.

98. A. Menditto, M. Patriarca, B. Magnusson, Understanding the meaning of accuracy, trueness and precision, Accred. Qual. Assur. 12 (2007) 45–47.

99. G.L. Long, J.D. Winefordner, Limit of detection: a closer look at the IUPAC definition, Anal. Chem. 55 (1983) 713A–724A.

100. CITAC / EURACHEM GUIDE, Guide to quality in analytical chemistry, An Aid to Accreditation, 2002.

101. D.W. Hahn, N. Omenetto, Laser-induced breakdown spectroscopy (LIBS), part II: review of instrumental and methodological approaches to material analysis and applications to different fields, Appl. Spectrosc. 66 (2012) 347–419.

102. S. Zhang, M. He, Z. Yin, E. Zhu, W. Hang, B. Huang, Elemental fractionation and matrix effects in laser sampling based spectrometry, J. Anal. Atom. Spectrom. 31 (2016), 358–382.

103. P.W.J.M. Boumans, Theory of Spectrochemical Excitation, Plenum Press, New York, 1966.

104. L. Zheng, S. Niu, A.Q. Khan, S. Yuan, J. Yu, H. Zeng, Comparative study of the matrix effect in Cl analysis with laser-induced breakdown spectroscopy in a pellet or in a dried solution layer on a metallic target, Spectrochim. Acta B 118 (2016) 66–71.

105. M. Thompson, S.L.R. Ellison, A review of interference effects and their correction in chemical analysis with special reference to uncertainty, Accred. Qual. Assur. 10 (2005) 82–97.

106. W.B. Barnett, V.A. Fassel, R.N. Kniseley, Theoretical principles of internal standardization in analytical emission spectroscopy, Spectrochim. Acta B 23 (1968) 643–664.

107. N.B. Zorov, A.A. Gorbatenko, T.A. Labutin, A.M. Popov, A review of normalization techniques in analytical atomic spectrometry with laser sampling: From single to multivariate correction, Spectrochim. Acta B 65 (2010) 642–657.

108. E.C. Jung, D.H. Lee, J.I. Yun, J.G. Kim, J.W. Yeon, K. Song, Quantitative determination of uranium and europium in glass matrix by laser-induced breakdown spectroscopy, Spectrochim. Acta Part B 66 (2011) 761–764.

109. I. Choi, G.C.Y. Chan, X. Mao, D.L. Perry, R.E. Russo, Line selection and parameter optimization for trace analysis of uranium in glass matrices by laser-induced breakdown spectroscopy (LIBS), Appl. Spectrosc. 67 (2013) 1275–1284.

110. X. Wang, V. Motto-Ros, G. Panczer, D. De Ligny, J. Yu, J.M. Benoit, J.L. Dussossoy, S. Peuget, Mapping of rare earth elements in nuclear waste glass-ceramic using micro-laser induced breakdown spectroscopy (LIBS), Spectrochim. Acta B 87 (2013) 139–146.

111. M.S. Krzemnicki, H.A. Hänni, R.A.Walters, A new method for detecting Be diffusion-treated sapphires: laser-induced breakdown spectroscopy (LIBS), Gems Gemology 40 (2004) 314–322.

112. N.J. McMillan, C.E. McManus, R.S. Harmon, F.C. DeLucia, A.W. Miziolek, Laser induced breakdown spectroscopy analysis of complex silicate minerals—beryl, Anal. Bioanal. Chem. 385 (2006) 263–271.

113. G. Agrosì, G. Tempesta, E. Scandale, S. Legnaioli, G. Lorenzetti, S. Pagnotta, V. Palleschi, A. Mangone, M. Lezzerini, Application of laser induced breakdown spectroscopy to the identification of emeralds from different synthetic processes, Spectrochim. Acta B 102 (2014) 48–51.

114. M. Corsi, G. Cristoforetti, M. Giuffrida, M. Hidalgo, S. Legnaioli, V. Palleschi, A. Salvetti, E. Tognoni, C. Vallebona, Three-dimensional analysis of laser induced plasmas in single and double pulse configuration, Spectrochim. Acta Part B 59 (2004) 723–735.

115. J.A. Aguilera, C. Aragon, Characterization of a laser-induced plasma by spatially resolved spectroscopy of neutral atom and ion emissions. Comparison of local and spatially integrated measurements, Spectrochim. Acta Part B 59 (2004) 1861–1876.

116. A. De Giacomo,M. Dell'Aglio, R. Gaudiuso, G. Cristoforetti, S. Legnaioli, V. Palleschi, E. Tognoni, Spatial distribution of hydrogen and other emitters in aluminum laser induced plasma in air and consequences on spatially integrated laser-induced breakdown spectroscopy measurements, Spectrochim. Acta Part B 63 (2008) 980–987

117. G. Cristoforetti, G. Lorenzetti, S. Legnaioli, V. Palleschi, Investigation on the role of air in the dynamical evolution and thermodynamic state of a laser-induced aluminium plasma by spatial- and time-resolved spectroscopy, Spectrochim. Acta Part B 65 (2010) 787–796.

118. C. Barnett, E. Cahoon, J.R. Almirall, Wavelength dependence on the elemental analysis of glass by laser induced breakdown spectroscopy, Spectrochim. Acta B 63 (2008) 1016–1023.

119. E.M. Cahoon, J.R. Almirall, Wavelength dependence on the forensic analysis of glass by nanosecond 266 nm and 1064 nm laser induced breakdown spectroscopy, Appl. Opt. 49 (2010) C49–C57.

120. V. Burakov, N. Tarasenko, M. Nedelko, S. Isakov, Time-resolved spectroscopy and imaging diagnostics of single pulse and collinear double pulse laser induced plasma from a glass sample, Spectrochim. Acta B 63 (2008) 19–26.

121. M. Milan, J.J. Laserna, Diagnostics of silicon plasmas produced by visible nanosecond laser ablation, Spectrochim. Acta Part B 56 (2001) 275–288.

122. C. Gerhard, J. Hermann, L. Mercadier, L. Loewenthal, E. Axente, C.R. Luculescu, T. Sarnet, M. Sentis, W. Viöl, Quantitative analyses of glass via laser-induced breakdown spectroscopy in argon, Spectrochim. Acta Part B 101 (2014) 32–45.

123. V. Motto-Ros, Q. Ma, S. Grégoire, W. Lei, X. Wang, F. Pelascini, F. Surma, V. Detalle, J. Yu, Dual-wavelength differential spectroscopic imaging for diagnostics of laser-induced plasma, Spectrochim. Acta Part B 74–75 (2012) 11–17.

124. A. Sainz, A. Diaz, D. Casas, M. Pineda, F. Cubillo, M.D. Calzada, Abel inversion applied to a small set of emission data from a microwave plasma, Appl. Spectrosc. 60 (2006) 229–236.

125. J.A. Aguilera, C. Aragon, J. Bengoechea, Spatial characterization of laser-induced plasmas by deconvolution of spatially resolved spectra, Appl. Opt. 42 (2003) 5938–5946.

126. O.H. Nestor, H.N. Olsen, Numerical methods for reducing line and surface probe data, SIAM Rev. 2 (1960) 200–207.

127. S.S. Harilal, C.V. Bindhu, V.P.N. Nampoori, C.P.G. Vallabhan, Influence of ambient gas on the temperature and density of laser produced carbon plasma, Appl. Phys. Lett. 72 (1998) 167–169.

128. NIST Atomic Spectra Database: http://www.nist.gov/pml/data/asd.cfm.

129. A.S. Eppler, D.A. Cremers, D.D. Hickmott, M.J. Ferris, A.C. Koskelo, Matrix effects in the detection of Pb and Ba in soils using laser-induced breakdown spectroscopy, Appl. Spectrosc. 50 (1996) 1175–1181.

130. B. Bousquet, J.B. Sirven, L. Canioni, Towards quantitative laser-induced breakdown spectroscopy analysis of soil samples, Spectrochim. Acta Part B 62 (2007) 1582–1589.

131. A. Segnini, A.A.P. Xavier, P.L. Otaviani-Junior, E.C. Ferreira, A.M. Watanabe, M.A. Sperança, G. Nicolodelli, P.R. Villas-Boas, P.P.A. Oliveira, D.M.B.P. Milori, Physical and chemical matrix effects in soil carbon quantification using laser-induced break-down spectroscopy, Am. J. Anal. Chem. 5 (2014) 722–729.

132. A. Stankova, N. Gilon, L. Dutruch, V. Kanicky, A simple LIBS method for fast quantitative analysis of fly ashes, Fuel 11 (2010) 3468–3474.

133. D. Santos Jr., L.C. Nunes, G.G.A. de Carvalho, M.D.S. Gomes, P.F. de Souza, F.D.O. Leme, L.G.C.D. Santos, F.J. Krug, Laser-induced breakdown spectroscopy for analysis of plant materials: A review, Spectrochim. Acta B 71-72 (2012) 3–13.

134. G.G.A. de Carvalho, D. Santos Jr., M.S. Gomes, L.C. Nunes, M.B.B. Guerra, F.J. Krug, Influence of particle size distribution on the analysis of pellets of plant materials by laser-induced breakdown spectroscopy, Spectrochim. Acta B 105 (2015) 130–135.

135. A. Khumaeni, M. Ramli, Y. Deguchi, Y.I. Lee, N. Idris, K.H. Kurniawan, T.J. Lie, K. Kagawa, New technique for the direct analysis of food powders confined in a small hole using transversely excited atmospheric CO_2 laser-induced gas plasma, Appl. Spectrosc. 62 (2008) 1344–1348.

136. A. Khumaeni, Z.S. Lie, H. Niki, K.H. Kurniawan, E. Tjoeng, Y.I. Lee, K. Kurihara, Y. Deguchi, K. Kagawa, Direct analysis of powder samples using transversely excited atmospheric CO_2 laser-induced gas plasma at 1 atm, Anal. Bioanal. Chem. 400 (2011) 3279–3287.

137. W. Lei, J. El Haddad, V. Motto-Ros, N. Gilon-Delepine, A. Stankova, Q. Ma, X. Bai, L. Zheng, H. Zeng, J. Yu, Comparative measurements of mineral elements in milk powders with laser-induced breakdown spectroscopy and inductively coupled plasma atomic emission spectroscopy, Anal. Bioanal. Chem. 400 (2011) 3303–3313.

138. J.B. Sirven, A. Pailloux, Y. M'Baye, N. Coulon, T. Alpettaz, S. Gossé, Towards the determination of the geographical origin of yellow cake samples by laser-induced breakdown spectroscopy and chemometrics, J. Anal. At. Spectrom. 24 (2009) 451-459.

139. E.J. Judge, J.E. Barefield II, J.M. Berg, S.M. Clegg, G.J. Havrila, V.M. Montoya, L.A. Le, L.N. Lopez, Laser-induced breakdown spectroscopy measurements of uranium and thorium powders and uranium ore, Spectrochim. Acta Part B 83 (2013) 28–36.

140. X. Li, Z. Wang, Y. Fu, Z. Li, J. Liu, W. Ni, Application of a spectrum standardization method for carbon analysis in coal using laser-induced breakdown spectroscopy (LIBS), Appl. Spectrosc. 68 (2014) 955–962.

141. S. Yao, J. Xu, X. Dong, B. Zhang, J. Zheng, J. Lu, Optimization of laser-induced breakdown spectroscopy for coal powder analysis with different particle flow diameters, Spectrochim. Acta B 110 (2015) 146–150.

142. M.A. Gondal, M.A. Dastageer, A.A. Naqvi, A.A. Isab, Y.W. Maganda, Detection of toxic metals (lead and chromium) in talcum powder using laser induced breakdown spectroscopy, Appl. Opt. 51 (2012) 7395–7401.

143. L. St-Onge, E. Kwong, M. Sabsabia, E.B. Vadasb, Quantitative analysis of pharmaceutical products by laser-induced breakdown spectroscopy, Spectrochim. Acta Part B 57 (2002) 1131–1140.

144. H. Zheng, F.Y. Yueh, T. Miller, J.P. Singh, K.E. Zeigler, J.C. Marra, Analysis of plutonium oxide surrogate residue using laser-induced breakdown spectroscopy, Spectrochim. Acta Part B 63 (2008) 968–974.

145. B. Lal, H. Zheng, F.Y. Yueh, J.P. Singh, Parametric study of pellets for elemental analysis with laser-induced breakdown spectroscopy, Appl. Opt. 43 (2004) 2792–2797.

146. M.A. Gondal, T. Hussain, Z.H. Yamini, M.A. Baig, The role of various binding materials for trace elemental analysis of powdered samples using laser-induced breakdown spectroscopy, Talanta 72 (2007) 642–649.

147. N. Gilon, J. El-Haddad, A. Stankova, W. Lei, Q. Ma, V. Motto-Ros, J. Yu, A matrix effect and accuracy evaluation for the determination of elements in milk powder LIBS and laser ablation/ICP-OES spectrometry, Anal. Bioanal. Chem. 401 (2011) 2681–2689.

148. S.I. Gornushkin, I.B. Gornushkin, J.M. Anzano, B.W. Smith, J.D. Winefordner, Effective normalization technique for correction of matrix effects in laser-induced breakdown spectroscopy detection of magnesium in powdered samples, Appl. Spectrosc. 56 (2002) 433–436.

149. J.N. Miller, J.C. Miller, Statistics and chemometrics for analytical chemistry, Pearson Education, 2005.

150. P. Pohl, What do metals tell us about wine? Trends Anal. Chem. 26 (2007) 941–949.

151. H. Hopfer, J. Nelson, T.S. Collins, H. Heymann, S.E. Ebeler, The combined impact of vineyard origin and processing winery on the elemental profile of red wines, Food Chem. 172 (2015) 486–496.

152. V.S. Šelih, M. Šala, V. Drgan, Multi-element analysis of wines by ICP-MS and ICP-OES and their classification according to geographical origin in Slovenia, Food Chem. 153 (2014) 414–423.

153. P.P. Coetzee, F.P. van Jaarsveld, F. Vanhaecke, Intraregional classification of wine via ICP-MS elemental fingerprinting, Food Chem. 164 (2014) 485–492.

154. S. Frías, J.E. Conde, J.J. Rodríguez-Bencomo, F. García Montelongo, J.P. Pérez-Trujillo, Classification of commercial wines from the Canary Islands (Spain) by chemometric techniques using metallic contents, Talanta 59 (2003) 335–344.

155. P. Kment, M. Mihaljevič, V. Ettler, O. Šebek, L. Strnad, L. Rohlová, Differentiation of Czech wines using multielement composition–A comparison with vineyard soil, Food Chem. 91 (2005) 157–165.

156. A. Jos, I. Moreno, A.G. González, G. Repetto, A.M. Cameán, Differentiation of sparkling wines (cava and champagne) according to their mineral content, Talanta 63 (2004) 377–382.

157. M.P. Fabani, R.C. Arrúa, F. Vázquez, M.P. Diaz, M.V. Baroni, D.A. Wunderlin, Evaluation of elemental profile coupled to chemometrics to assess the geographical origin of Argentinean wines, Food Chem. 119 (2010) 372–379.

158. A. Gonzálvez, A. Llorens, M.L. Cervera, S. Armenta, M. de la Guardia, Elemental fingerprint of wines from the protected designation of origin Valencia, Food Chem. 112 (2009) 26–34.

159. P.P. Coetzee, F.E. Steffens, R.J. Eiselen, O.P. Augustyn, L. Balcaen, F. Vanhaecke, Multi-element analysis of South-African wines by ICP-MS and their classification according to geographical origin, J. Agric. Food Chem. 53 (2005) 5060–5066.

160. P. Serapinas, P.R. Venskutonis, V. Aninkevičius, Ž. Ežerinskis, A. Galdikas, V. Juzikien, Step by step approach to multi-element data analysis in testing the provenance of wines, Food Chem. 107 (2008) 1652–1660.

161. I. Geana, A. Iordache, R. Ionete, A. Marinescu, A. Ranca, M. Culea, Geographical origin identification of Romanian wines by ICP-MS elemental analysis, Food Chem. 138 (2013) 1125–1134.

162. I.M. Moreno, D. González-Weller, V. Gutierrez, M. Marino, A.M. Cameán, A.G. González, A. Hardisson, Determination of Al, Ba, Ca, Cu, Fe, K, Mg, Mn, Na, Sr and Zn in red wine samples by inductively coupled plasma optical emission spectroscopy: Evaluation of preliminary sample treatments, Microchem. J. 88 (2008) 56–61.

163. W.N.L. dos Santos, G.C. Brandao, L.A. Portugal, J.M. David, S.L.C. Ferreira, A photo-oxidation procedure using UV radiation/H_2O_2 for decomposition of wine samples-Determination of iron and manganese content by flame atomic absorption spectrometry, Spectrochim. Acta Part B 64 (2009) 601–604.

164. J.B. Sirven, B. Salle, P. Mauchien, J.L. Lacour, S. Maurice, G. Manhes, Feasibility study of rock identification at the surface of Mars by remote laser-induced breakdown spectroscopy and three chemometric methods, J. Anal. At. Spectrom. 22 (2007) 1471–1480.

165. Y. Tian, Z. Wang, X. Han, H. Hou, R. Zheng, Comparative investigation of partial least squares discriminant analysis and support vector machines for geological cuttings identification using laser-induced breakdown spectroscopy, Spectrochim. Acta Part B 102 (2014) 52–57.

166. R. Sattmann, I. Mönch, H. Krause, R. Noll, S. Couris, A. Hatziapostolou, A. Mavromanolakis, C. Fotakis, E. Larrauri, R. Miguel, Laser-induced breakdown spectroscopy for polymer identification, Appl. Spectrosc. 52 (1998) 456–461.

167. M. Boueri, V. Motto-Ros, W. Lei, Q. Ma, L. Zheng, H. Zeng, J. Yu, Identification of polymer materials using laser-induced breakdown spectroscopy combined with artificial neural networks, Appl. Spectrosc. 65 (2011) 307–314.

168. F.C. De Lucia Jr., J.L. Gottfried, Influence of variable selection on partial least squares discriminant analysis models for explosive residue classification, Spectrochim. Acta Part B 66 (2011) 122–128.

169. J.L. Gottfried, F.C. De Lucia Jr., A.W. Miziolek, Discrimination of explosive residues on organic and inorganic substrates using laser-induced breakdown spectroscopy, J. Anal. At. Spectrom. 24 (2009) 288–296.

170. P. Lucena, A. Doña1, L.M. Tobaria, J.J. Laserna, New challenges and insights in the detection and spectral identification of organic explosives by laser induced breakdown spectroscopy, Spectrochim. Acta Part B 66 (2011) 12–20.

171. M. Baudelet, J. Yu, M. Bossu, J. Jovelet, J.P. Wolf, T. Amodeo, E. Frejafon, P. Laloi, Discrimination of microbiological samples using femtosecond laser-induced breakdown spectroscopy, Appl. Phys. Lett. 89 (2006) 163903.

172. F.Y. Yueh, H. Zheng, J.P. Singh, S. Burgess, Preliminary evaluation of laser-induced breakdown spectroscopy for tissue classification, Spectrochim. Acta Part B 64 (2009) 1059–1067.

173. A. De Giacomo, M. Dell'Aglio, O. De Pascale, M. Capitelli, From single pulse to double pulse ns-Laser Induced Breakdown Spectroscopy under water: Elemental analysis of aqueous solutions and submerged solid samples, Spectrochim. Acta Part B 62 (2007) 721–738.

174. P. Fichet, P. Mauchien, J.F. Wagner, C. Moulin, Quantitative elemental determination in water and oil by laser induced breakdown spectroscopy, Anal. Chim. Acta 429 (2001) 269–278.

175. P. Yaroshchyk, R.J.S. Morrison, D. Body, B.L. Chadwick, Quantitative determination of wear metals in engine oils using LIBS: The use of paper substrates and a comparison between single- and double-pulse LIBS, Spectrochim. Acta Part B 60 (2005) 1482–1485.

176. J. Bocková, Y. Tian, H. Yin, N. Gilon, Q. Ma, Y. Chen, P. Veis, J. Yu, Determination of metal elements in wine using laser-induced breakdown spectroscopy, Appl. Spectrosc. 71 (2017) 1750–1759.

177. M.A. Aguirre, S. Legnaioli, F. Almodóvar, M. Hidalgo, V. Palleschi, A. Canals, Elemental analysis by surface-enhanced laser-induced breakdown spectroscopy combined with liquid–liquid microextraction, Spectrochim. Acta, Part B 79–80 (2013) 88–93.

178. V. Lazic, A. Palucci, S. Jovicevic, M. Carpanese, Detection of explosives in traces by laser induced breakdown spectroscopy: Differences from organic interferents and conditions for a correct classification, Spectrochim. Acta Part B 66 (2011) 644–655.

179. Z. Abdel-Salam, J. Al Sharnoubi, M.A. Harith, Qualitative evaluation of maternal milk and commercial infant formulas via LIBS, Talanta 115 (2013) 422–426.

180. A. Metzinger, Ė. Kovács-Széles, I. Almási, G. Galbács, Laser-induced breakdown spectroscopy (LIBS) for the analysis of cesium in liquid samples of biological origin, Appl. Spectrosc. 68 (2014) 789–793.

181. M.A. Aguirre, E.J. Selva, M. Hidalgo, A. Canals, Dispersive liquid–liquid microextraction for metals enrichment: A useful strategy for improving sensitivity of laser-induced breakdown spectroscopy in liquid samples analysis, Talanta 131 (2015) 348–353.

182. S. Moncayo, J.D. Rosales, R. Izquierdo-Hornillos, J. Anzano, J.O. Caceres, Classification of red wine based on its protected designation of origin (PDO) using Laser-induced Breakdown Spectroscopy (LIBS), Talanta 158 (2016) 185–191.

183. M.G. Volpe, F. La Cara, F. Volpe, A. De Mattia, V. Serino, F. Petitto, C. Zavalloni, F. Limone, R. Pellecchia, P.P. De Prisco, M. Di Stasio, Heavy metal uptake in the enological food chain, Food Chem. 117 (2009) 553–560.

184. M.J. Anjos, R.T. Lopes, E.F.O. de Jesus, S. Moreira, R.C. Barroso, C.R.F. Castro, Trace elements determination in red and white wines using total-reflection X-ray fluorescence, Spectrochim. Acta Part B 58 (2003) 2227–2232.

185. A.I. Kuznetsova, T.E. Morgulis, Investigation of internal standardisation for atomic emission spectrometric analysis with direct current arc excitation, J. Anal. At. Spectrom. 3 (1988) 973–977.

186. L. Breiman, Random forests, Mach. Learn. 45 (2001) 5–32.

187. L. Breiman, J. Friedman, R. Olshen, C. Stone, Classification and regression tree, CRC Press, 1984.

188. L. Zheng, D.G. Watson, B.F. Johnston, R.L. Clark, R. Edrada-Ebel, W. Elseheri, A chemometric study of chromatograms of tea extracts by correlation optimization warping in conjunction with PCA, support vector machines and random forest data modeling, Anal. Chim. Acta 642 (2009) 257–265.

189. J. Remus, K.S. Dunsin, Robust validation of pattern classification methods for laser-induced breakdown spectroscopy, Appl. Opt. 51 (2012) B49–B56.

190. L. Sheng, T. Zhang, G. Niu, K. Wang, H. Tang, Y. Duan, H. Li, Classification of iron ores by laser-induced breakdown spectroscopy (LIBS) combined with random forest (RF), J. Anal. At. Spectrom. 30 (2015) 453–458.

191. H. Tang, T. Zhang, X. Yang, H. Li, Classification of different types of slag samples by laser-induced breakdown spectroscopy (LIBS) coupled with random forest based on variable importance (VIRF), Anal. Methods, 7 (2015) 9171–9176.

192. T. Zhang, L. Liang, K. Wang, H. Tang, X. Yang, Y. Duan, H. Li, A novel approach for the quantitative analysis of multiple elements in steel based on laser-induced breakdown spectroscopy (LIBS) and random forest regression (RFR), J. Anal. At. Spectrom. 29 (2014) 2323–2329.

193. S. Adusumilli, D. Bhatt, H. Wang, P. Bhattacharya, V. Devabhaktuni, A low-cost INS/GPS integration methodology based on random forest regression, Expert Syst. Appl. 40 (2013) 4653–4659.

194. A. Liaw, M. Wiener, Classification and regression by randomForest, R News 2 (2002) 18–22.

195. Y. Freund, R.E. Schapire, A desicion-theoretic generalization of on-line learning and an application to boosting, Lect. Notes Comput. Sci 904 (1995) 23–37.

196. Y. Tian, E.B. Sokolova, R. Zheng, Q. Ma, Y. Chen, J. Yu, Characteristics of the ablation plume induced on glasses for analysis purposes with laser-induced breakdown spectroscopy, Spectrochim. Acta Part B 114 (2015) 7–14.

197. Y. Tian, H. Cheung, R. Zheng, Q. Ma, Y. Chen, N. Delepine-Gilon, J. Yu, Elemental analysis in powders with surface-assisted thin film laser-induced breakdown spectroscopy, Spectrochim. Acta B 214 (2016) 16–24.

198. Y. Tian, C. Yan, T. Zhang, H. Tang, H. Li, J.L. Yu, J. Bernard, L. Chen, S. Martin, N. Delepine-Gilon, J. Bocková, P. Veis, Y. Chen, J. Yu, Classification of wines according to their production regions with the contained trace elements using laser-induced breakdown spectroscopy, Spectrochim. Acta B 135 (2017) 91–101.

199. H. Hou, Y. Tian, Y. Li, R. Zheng, Study of pressure effects on laser induced plasma in bulk seawater, J. Anal. At. Spectrom. 29 (2014) 169–175.

200. B. Thornton, T. Takahashi, T. Sato, T. Sakka, A. Tamura, A. Matsumoto, T. Nozaki, T. Ohki, K. Ohki, Development of a deep-sea laser-induced breakdown spectrometer for in situ multi-element chemical analysis, Deep Sea Res. Part I 95 (2015) 20–36.

201. Z.A. Arp, D.A. Cremers, R.D. Harris, D.M. Oschwald, G.R. Parker, D.M. Wayne, Feasibility of generating a useful laser-induced breakdown spectroscopy plasma on rocks at high pressure: preliminary study for a Venus mission, Spectrochim. Acta Part B 59 (2004) 987–999.

202. D.A. Cremers, Space applications of LIBS, In Laser-Induced Breakdown Spectroscopy (pp. 257–291), Springer Berlin Heidelberg, 2014.

Annex

List of publications

1. Characteristics of the ablation plume induced on glasses for analysis purposes with laser-induced breakdown spectroscopy.

   Y. Tian, E.B. Sokolova, R. Zheng, Q. Ma, Y. Chen, J. Yu, *Spectrochimica Acta Part B-atomic Spectroscopy*, 114, 7–14 (2015).

2. Elemental analysis in powders with surface-assisted thin film laser-induced breakdown spectroscopy.

   Y. Tian, H. Cheung, R. Zheng, Q. Ma, Y. Chen, N. Delepine-Gilon, J. Yu, *Spectrochimica Acta Part B-atomic Spectroscopy*, 214, 16–24 (2016).

3. Classification of wines according to their production regions with the contained trace elements using laser-induced breakdown spectroscopy.

   Y. Tian, C. Yan, T. Zhang, H. Tang, H. Li, J.L. Yu, J. Bernard, L. Chen, S. Martin, N. Delepine-Gilon, J. Bocková, P. Veis, Y. Chen, J. Yu, *Spectrochimica Acta Part B-atomic Spectroscopy*, 135, 91–101 (2017).

4. Determination of metal elements in wine using laser-induced breakdown spectroscopy.

   J. Bocková, **Y. Tian,** H. Yin, N. Delepine-Gilon, Q. Ma, Y. Chen, P. Veis, J. Yu, *Applied Spectroscopy*, 71, 1750–1759 (2017).

Oral presentations

1. Influence of ablation laser wavelength and ambient gas on LIBS analysis of glass with polished or frosted surface.

   The *8th Euro-Mediterranean Symposium on Laser Induced Breakdown Spectroscopy*, September 14–18, 2015, Linz, Austria.

2. Classification of wines according to the contained trace elements with LIBS.

   The *9th International Conference on Laser Induced Breakdown Spectroscopy*, September 12–16, 2016, Chamonix-Mont-Blanc, France.